Title
Olfactory representations in an entorhinal-dentate pathway

Author
Woods, Nicholas I

Publication Date
2020

Peer reviewed|Thesis/dissertation

Olfactory representations in an entorhinal-dentate pathway

by
Nicholas Woods

DISSERTATION
Submitted in partial satisfaction of the requirements for degree of
DOCTOR OF PHILOSOPHY

in

Neuroscience

in the

GRADUATE DIVISION
of the
UNIVERSITY OF CALIFORNIA, SAN FRANCISCO

Approved:

DocuSigned by:
Anatol Kreitzer
03F45B9A4CF445E...

Anatol Kreitzer
Chair

DocuSigned by:
Zachary Knight
DocuSigned by:
Vikaas Sohal
DocuSigned by:
Mazen Kheirbek
D52190F39543433...

Zachary Knight
Vikaas Sohal
Mazen Kheirbek

Committee Members

Acknowledgements

I started my graduate studies in 2016 with uncertainty. Uncertainty in *what* I would study, *how* I would go about studying the problem, and *if* the results would ever make sense or have impact. Thankfully, early on, I was able to reduce uncertainty in at least one regard: *who* I would like to work for in my PhD training. It has been a pleasure and privilege to receive mentorship from Mazen Kheirbek throughout my PhD. I immediately felt comfortable to discuss ideas with Mazen, even in our initial meeting. When I first joined the lab it was almost brand new, and was a rather small enterprise with a handful of members. My first few months consisted of many instances of setting up equipment, piloting experiments, and trying out new methods I had never done before. On my own, I would have immediately hit the brakes at many points, and instead pursued what was more comfortable for me, but Mazen's optimism and willingness to try out new ideas encouraged me to embrace discomfort, to stare into the unknown until it becomes known. That approach will last with me.

I am also deeply indebted to Fabio Stefanini. Both a collaborator and great friend, Fabio spent countless hours in creating a real analysis pipeline out of our collective imagined framework. I believe in many ways my graduate studies would have been far lonlier and less insightful had it not been for our ability to work so effortlessly with one another. I am very thankful for the countless conversations (and countless espressos) we have had to weave together our backgrounds and ways of thinking.

I am more thankful to my wife, Maria, than I can possibly convey. Let me simply say she has provided perspective on what is really important in life when I have become fixated on granular details and anxieties. I am also thankful to my friends and family--my mom, dad and brother--who have offered support, kindness, and warmth throughout the last four years.

I am very appreciative of the feedback and support members of my thesis committee--Anatol Kreitzer, Zachary Knight, and Vikaas Sohal--have provided in my training, making time to think critically about my research and probe it in new ways I didn't consider. Lastly, thank you to Mark Anderson and Geri Ehle of the MD/PhD program at UCSF for believing in my potential and allowing me to pursue a career as a physician-scientist. I am a bit further along in my understanding of what I can contribute to better the human condition, and I have a little less uncertainty now in how to do that.

Contributions

Chapter 2 of this thesis is reproduced in an adapted form from the following publication:

Woods, N. I., Stefanini, F.*, Apodaca-Montano, D. L., Tan, I. M. C., Biane, J. S., & Kheirbek, M. A. (2020). The Dentate Gyrus Classifies Cortical Representations of Learned Stimuli. Neuron.* https://doi.org/10.1016/j.neuron.2020.04.002

Conceptualization and Writing, N.I.W., F.S., and M.A.K.; Methodology, N.I.W., J.S.B., and M.A.K.; Investigation, N.I.W., D.L.A.-M., and I.M.C.T.; Formal Analysis, N.I.W., F.S., and M.A.K.; Supervision and Funding Acquisition, M.A.K.

Olfactory representations in an entorhinal-dentate pathway

By Nicholas Woods

Abstract

Modern tools of neuroscience have permitted increasing levels of detail and sophistication in our study of how the brain works. Yet, many of the basic questions on the functioning of the nervous system have remained unchanged over centuries. One long-lasting question is how can the brain transform physical stimuli from the external world into a pattern of internal signals that can be utilized for meaningful behavior? Such a broad and all encompassing topic, of course, cannot be addressed by a single set of experiments, but the intent of this thesis is to contribute a sliver of understanding to this foundational question. I've attempted over the course of my graduate studies to use cutting edge tools and analysis methods in order to revisit some lines of investigation pursued many decades earlier, but were not comprehensively addressed due to technical limitations in those periods.

Animals must be able to take external stimuli from their environment and create an internal representation that can be used for survival. The neocortex conveys general representations of sensory events to the hippocampus, and the hippocampus is thought to classify and sharpen the distinctions between these events. We recorded populations of dentate gyrus granule cells (DG GCs) and lateral entorhinal cortex (LEC) neurons across days to understand how sensory representations are modified by experience. We found representations of odors in DG GCs that required synaptic input

from the LEC. Odor classification accuracy in DG GCs correlated with future behavioral discrimination. In associative learning, DG GCs, more so than LEC neurons, changed their responses to odor stimuli, increasing the distance in neural representations between stimuli, responding more to the conditioned and less to the unconditioned odorant. Thus, with learning, DG GCs amplify the decodability of cortical representations of important stimuli, which may facilitate information storage to guide behavior.

In Chapter 1 (Introduction), I provide an introduction to the hippocampus, with special emphasis on one of its circuits, the lateral perforant pathway to the dentate gyrus. Over the last few decades, the dentate gyrus has been chipped away at by various methodologies to try to understand how this structure both receives and transmits information, and I will illustrate how past approaches, which have tended to focus on the spatial domain, leave many basic questions unanswered.

In Chapter 2 (The dentate gyrus classifies cortical representations of learned stimuli), I present evidence of a robust anatomic and functional pathway providing olfactory information to the dentate gyrus. Using 2-photon imaging in awake, behaving mice, I demonstrate how olfactory information is represented at the level of a cortical input, the lateral entorhinal cortex, and its downstream site, the dentate gyrus. Chronic interruption of neural transmission within this pathway degrades the richness of olfactory information, further supporting a functional pathway for olfactory processing. I interrogate this olfactory pathway to better understand basic aspects of

experience-dependent changes in neural representations within the lateral entorhinal cortex and dentate gyrus. Using two simple learning paradigms, one aversive and one appetitive, I examine how experience shapes the single cell and population level responses within this circuit. Whereas neurons in the entorhinal cortex exhibit small changes in response to learning, the dentate granule cells exhibit large shifts to preferentially encode learned stimuli, and as an ensemble, faithfully represent the extent to which an animal is able to behaviorally discriminate odors.

In Chapter 3 (Conclusions), I place these experimental findings within the larger context of our knowledge of the hippocampus to date. I propose that the dentate gyrus can be better appreciated by further studies examining its nonspatial roles, and suggest future experimental approaches which could utilize the strategies described here to expand our knowledge of dentate function in health and disease states.

Finally, in Chapter 4 (Appendix on analysis pipeline), I provide a simple “how-to” user guide on the code and analysis methods used throughout these studies. The reader is provided some simple background and documentation both on why and how we developed a custom python-based analysis pipeline for analyzing calcium imaging neural data, with the goal of a future graduate student or researcher to easily utilize, adapt, and build upon the blueprint of code established for these experiments. A basic demonstration of the flow of data through the pipeline is provided, followed by brief descriptions of the essential analyses performed on these datasets to provide a framework for employing these methods.

Table of Contents

List of Figures

Chapter 1

Chapter 2

Chapter 3

Chapter 1: Introduction

The hippocampus has traditionally been studied as a spatial memory structure

As humans, our interest in understanding memory predates any formal study of the brain. Our keen ability to take information from our surroundings, store it, and later retrieve it for use informs a large part of who we are, where we have been, and what we have done with our lives. In this way, memory helps to bind the past with the present, and helps orient ourselves toward future goals (Zeidman and Maguire, 2016). Forms of memory are also maintained in simpler organisms to various degrees, indicating that the underlying biology of memory is a critical process of life and underwent successive gradations of complexity throughout evolutionary history (Dere et al., 2006; Eichenbaum, 1992; Spear, 1973). When memory is impaired or lost, as is the case with certain diseases, we see the devastating consequences not just in the ability to remember facts or events, but also in personality, identity, and cohesion of the individual (Addis and Tippett, 2004; Bishop et al., 2010). Understandably, then, a large focus of neuroscience in the last century has been to identify the neurobiological substrates and mechanisms of memory (Squire and Knowlton, 1995), both to understand these basic processes and find new ways to treat memory-related pathologies.

At a general level, memory refers to any process that can receive information and store it for later use, and it can be further subclassified into several categories

(Eichenbaum, 2017; Eichenbaum et al., 2007). The domain of declarative memory is divided into two types: semantic memory refers to knowledge of facts, and episodic memory is composed of subjective, first-hand experiences, from the mundane example like where you parked your car, to the more meaningful instance as the day you were married (Squire and Knowlton, 1995; Tulving and Markowitsch, 1998). The sensory experiences that shape an episodic memory contain a mixture of context ("where," place and time) and content ("what," objects and events) (Hainmueller and Bartos, 2020; Knierim et al., 2014). Our scientific approach at understanding episodic memory has aimed at pinpointing brain systems that participate in the reception, storage, and recall of conscious information.

The effort to assign a region or set of regions involved in episodic memory largely began in the 1950s with an influential paper on the patient Henry Molaison, a.k.a. 'H.M,' who, at the age of 15, received bilateral, partial temporal lobectomies as a treatment for his drug-refractory epilepsy (Scoville and Milner, 1957). He reportedly suffered fewer and less severe seizures after his surgery, but unfortunately exhibited unanticipated anterograde memory loss, or the inability to form new declarative memories (Augustinack et al., 2014). His memory of life events prior to the surgery were mostly intact, as was his ability to learn non-declarative, procedural memory tasks, indicating that the resected structures were critical in the *formation and/or consolidation* of episodic memories (Milner et al., 1968). It was often reported that the hippocampus was selectively resected in 'H.M', however, using high-resolution MRI

shortly after his death in 2008, it was found that other temporal lobe structures were also resected, including portions of the amygdala, the entire entorhinal cortex on both sides, subiculum, and the piriform cortex (Annese et al., 2014; Augustinack et al., 2014). Follow-up studies in other humans with lesions of the medial temporal lobe--via disease processes or trauma--corroborated the findings in H.M, and further implicated the hippocampus as critical hub in the formation of episodic memory (Rosenbaum et al., 2000, 2014; Squire, 1992).

Following the enthusiasm generated over H.M, the momentum of studying the hippocampus as a locus of memory was furthered by landmark findings in the field of animal research. In 1971, John O'Keefe and John Dostrovsky performed extracellular electrophysiological recordings from pyramidal cells in the hippocampus of behaving rats and found that a subset of neurons fired exclusively when a rat was in a particular location of its environment (O'Keefe and Dostrovsky, 1971). These cells became known as "place cells" due to their firing when an animal entered a specific area in the outside world, termed the "place field" for that cell. Place cells were subsequently found as a common feature throughout various subregions of the hippocampus, including CA3, CA1, and the dentate gyrus (Alme et al., 2014; Kim et al., 2020; Senzai and Buzsáki, 2017; Stefanini et al., 2020; Zhang et al., 2020; Ziv et al., 2013). These early studies were integrated with prior observations into a thesis of "cognitive map theory" by O'Keefe, in which he hypothesized that animals relate to their surroundings by forming a neural representation of the external world, an idea first articulated much earlier by

the animal psychologist Edward Tolman (McNaughton et al., 2006; O'keefe and Nadel, 1978; Olton et al., 1979; Tolman, 1948). Tolman observed that rats were capable of learning the physical layout of a maze and using cues in their environment to mentally navigate the best possible route to reward, without needing to physically explore every portion of the maze beforehand. Such a feat, he claimed, could only be possible if the outside physical surroundings were coded somewhere in the brain into an internal coordinate framework (Tolman, 1948). The discovery of place cells by O'Keefe and Dostrovsky provided the first neural basis of this cognitive map, and implicated the hippocampus as the area of the brain where such an internal representation is formed. Importantly, O'Keefe noted in his cognitive map theory that the existence of place cells indicated hippocampal cognitive maps utilized allocentric, or externally objective spatial relationships from the environment. That is, the actual physical relationships between cues are represented faithfully in patterns of cell activity. This is opposed to the use of egocentric, or self-oriented cues that are the basis for mapping other sensory functions, such as touch (Fyhn et al., 2004; O'keefe and Nadel, 1978; Stein, 1989; Wang et al., 2018).

The existence of place cells in the hippocampus sparked interest into how these cells came about, that is, where does the information arise that permits their exquisitely fine-tuned firing to the outside world? The entorhinal cortex provides the main excitatory input to subregions of the hippocampus (discussed more below), and indeed, it was found in a series of studies by May-Britt Moser, Edvard Moser, and

colleagues that cells in the medial entorhinal cortex (a subdivision of the entorhinal cortex) provide the necessary information for place cells to emerge in the hippocampus (Hafting et al., 2005; Strange et al., 2014). Within the medial entorhinal cortex (MEC), certain cells fire in response to the animal exploring its environment, with patterns of activity distributed in a lattice-like arrangement in regard to the external surroundings. Such cells were called 'grid cells' since the firing in space resembled a geometric, triangular-like grid (Hafting et al., 2005). Intact grid cell activity is necessary for the formation and stability of place cells in the hippocampus (Fyhn et al., 2004; Leutgeb et al., 2004; Moser et al., 2008). Later studies found similar, complementary types of spatially relevant cells in the MEC, such as head-direction cells, border cells, and speed cells (Høydal et al., 2019; Kropff et al., 2015; Solstad et al., 2008), all of which furthered the idea of the entorhinal-hippocampal system as a spatially-dedicated network.

The impact of these recent studies combined with the previous discovery of place cells provided compelling groundwork to further dissect and understand all elements of the hippocampal spatial map. Many research groups have gone on to contribute much detail into the mechanisms of entorhinal-hippocampal circuitry in forming and maintaining spatial representations (Alme et al., 2014; Igarashi et al., 2014; Zhang et al., 2014; Ziv et al., 2013), including a major finding in CA1 pyramidal cells that interrupting long-term potentiation (LTP) interferes with the stability of place fields, implying that ongoing synaptic changes are required to form lasting spatial

representations (Rotenberg et al., 1996). This enthusiasm for place cells, grid cells, and viewing the 'hippocampus as a spatial map', however, has led to a relative paucity of knowledge for the non-spatial roles of the hippocampus (moreover, due to the relative ease of studying CA1 pyramidal neurons, essentially all of the nonspatial studies of hippocampal function to-date have been carried out in the CA1 subregion) (Aronov et al., 2017; Igarashi et al., 2014; MacDonald et al., 2013). The intention of this historical perspective is to provide some context on how the initial excitement about one feature of hippocampal processing--a neural basis of a spatial cognitive map--led to an intense focus and perhaps a constrained view of all hippocampal functioning (Nilssen et al., 2019). There are at the very least two major reasons to reappraise the hippocampus and inquire about its nonspatial roles. First, by looking at nonspatial coding, such as features of objects, tones, and odors, we may unveil previously unknown roles of individual neurons or of neural ensembles. Indeed, each subregion of the hippocampus is purported to carry out certain defined roles, but many of these functions have only been thoroughly explored in regard to the spatial domain (Knierim and Neunuebel, 2016). Second, the dedicated nonspatial cortical-hippocampal circuits are involved in the early phases of neurodegenerative disease, particularly Alzheimer's Disease, and their activity differences from spatial circuits may offer clues to selective vulnerability under disease states (Khan et al., 2014; Reagh and Yassa, 2014).

Anatomy of the hippocampus and flow of information throughout its subregions

The adult mammalian hippocampus is a bilateral structure embedded deep within the medial temporal lobes. The latin meaning of *hippocampus* translates directly to "seahorse," due to its prototypical appearance upon dissection in the human brain. In the rodent, the hippocampus resembles more of an elongated crescent shape, extending most of the ventral-dorsal axis of the forebrain. In humans and other mammals, portions along the axis of the hippocampus subserve various functions, ranging from strictly spatial/cognitive functions in the dorsal regions to largely emotional/stress regulation functions in the ventral subregions (Fredes et al., 2020; Jimenez et al., 2018; Kesner et al., 2011; Kheirbek et al., 2013; Okuyama et al., 2016). During embryonic development, the telencephalon gives rise to the neocortex with six distinct cell layers, and the ventral limbic structures (the hippocampus included) with three layers: a deep plexiform layer, followed by a layer of principal cells, with a diffuse fiber (largely acellular) layer on top (Michael and László, 2006; Stanfield and Cowan, 1979). The hippocampus follows this folded three-layer patterning, and is composed of four main areas in the mammalian brain: the dentate gyrus, the cornu ammonis (due to the "ram's head" appearance of this area), the presubiculum, and the subiculum (Amaral and Witter, 1989). Almost a century ago, anatomist Lorente de No further subdivided the cornu ammonis (abbreviated CA) into CA1, CA2, CA3, and CA4, a classification that is still used today to refer to regions of principal glutamatergic cells.

Albeit an oversimplification of a complex circuit, the canonical trisynaptic loop is a useful starting point to understand hippocampal function and how neural information is transmitted throughout its subregions (**Figure 1.1**). Every primary sensory modality relays information to the entorhinal cortex, a six-layered band of cortical tissue that receives sensory information within the deeper layers and sends efferents to the hippocampus via stellate cells in layers II and III (Witter et al., 2017). Axons originating from the entorhinal cortex cross the hippocampal fissure and constitute an axonal tract called the perforant pathway. The perforant path splits into two divisions, the indirect and direct pathway, contacting separate portions of the hippocampus (Hjorth-Simonsen and Jeune, 1972). In the direct pathway, layer III cells of the entorhinal cortex send axons to the apical dendrites of CA1 pyramidal cells, which are also the main output neurons of the hippocampus and sends projections back to deeper layers of entorhinal cortex (van Groen, 2001; van Groen et al., 2003). The direct pathway has been studied extensively in regard to associative learning processes, largely due to the superficial location of CA1 making it amenable to in vivo study, and will not be covered in extensive detail here (Brun et al., 2008; Igarashi et al., 2014; Masurkar et al., 2017). Entorhinal projections from layer II, on the other hand, form the indirect perforant pathway (Andersen et al., 1966). These axons synapse onto apical dendrites of granule cells and interneurons located in the dentate gyrus (the first synapse of the trisynaptic loop) (van Groen et al., 2003; Lømo, 1971). Entorhinal input to the dentate gyrus (DG) is further segregated: the lateral entorhinal cortex (LEC)

selectively innervates the outer molecular layer (OML), whereas the medial entorhinal cortex (MEC) sends projections to the middle molecular layer (MML) (van Groen, 2001). Finally, granule cell dendrites along the inner molecular layer (IML) are innervated by glutamatergic mossy cells from both the ipsi- and contralateral hilus (a plexiform layer of cells embedded within the granule cell layer) (Scharfman, 2016, 2018). The inner molecular layer also receives innervation from hilar interneurons, namely, basket cells, which ramify large spans of the DG (Freund and Buzsaki, 1996). Hence, within the DG, there is a highly organized, laminated input along the length of granule cell dendrites that conveys segregated entorhinal information (Deller, 1998; Phinney et al., 2004). Granule cells extend axons through the hilus and form the mossy fiber pathway, terminating with large axonal boutons onto CA3 pyramidal cells dendrites (the second synapse of the trisynaptic loop). A single granule cell typically contacts 10-15 CA3 pyramidal cells, and multiple granule cells contact any given CA3 cell (Acsady et al., 1998). Thus, firing of granule cells leads to a high probability of downstream activation in CA3 pyramidal neurons (Henze et al., 2002; Nicoll and Schmitz, 2005). These cells also form recurrent excitatory connections with one another which generates an 'auto-associative' network, in which just a few active cells can spread activation to an entire ensemble of cells (Miles et al., 2014; van Strien et al., 2009). From here, CA3 axons form schaffer collaterals and synapse upon the proximal dendrites of CA1 pyramidal cells (the third synapse), which send outgoing signals back to deep layers of the entorhinal cortex (van Strien et al., 2009).

The structure of the hippocampus leads us naturally to enquire about its function. Namely, what type of modulation of input is occurring at each step along the trisynaptic loop before information is delivered back to the entorhinal cortex? And how do the patterns of activity along the trisynaptic loop facilitate aspects of episodic memory? We will focus on the first step of information processing in the indirect pathway, the entorhinal to dentate gyrus.

The dentate gyrus plays a role in disambiguating similar experiences

Animals must distinguish features of their environment in order to optimally explore them to obtain food, mates, and safety. Any given element of their surroundings may not carry any immediate meaning, but with reinforcement, animals will learn to approach/avoid those cues that predict salient outcomes while ignoring others. One way that neural circuits may implement this form of learning is by amplifying the differences between relevant and irrelevant stimuli. In daily life, experiences often have overlapping features or contextual elements, and it is important to be able to distinguish those experiences. In terms of formation and recall of episodic memories, we depend on this ability to form specific associations, as interference between similar episodes will generate confusion and poor decisions (Kesner, 2013; Spear, 1973). By increasing the distance between neural representations of cues with learning, certain circuits in the brain are thought to effectively “separate” a salient from

a non-salient stimulus, thus this general phenomenon is broadly called pattern separation (Rolls, 2013; Yassa and Stark, 2011).

As the entrypoint to the trisynaptic hippocampal circuit, the dentate gyrus (DG) has several notable features that implicate its functioning in part as a pattern separator, including a "sparse" network design (Boss et al., 1985; Rolls et al., 1998), laminated inputs carrying distinct informational content (Knierim et al., 2014; Witter, 2007), and the participation of mature granule cells alongside the continuous integration of newly generated neurons (Ming and Song, 2011; Overstreet-Wadiche and Westbrook, 2006). Hippocampal granule cells receive highly laminar inputs from the entorhinal cortex within the molecular layer of the DG. Input from the medial entorhinal cortex, conveying spatial cues, is restricted to the middle molecular layer (MML) (Ferbinteanu et al., 1999; Hafting et al., 2005; Hargreaves et al., 2005; Van Cauter et al., 2013; Witter, 2007; Yasuda and Mayford, 2006), whereas input from the lateral entorhinal cortex conveying contextual information is restricted to the outer molecular layer (OML) (Deshmukh and Knierim, 2011; Hargreaves et al., 2005; Hunsaker et al., 2007; Tsao et al., 2013; Witter, 2007; Woods et al., 2018; Yoganarasimha et al., 2011). Despite being substantially outnumbered by mature granule cells, newly integrated granule cells are thought to contribute heavily to pattern separation (Clelland et al., 2009; Nakashiba et al., 2012; Sahay et al., 2011; Tronel et al., 2012). The overall number of granule cells (newborn and mature) within the DG greatly outnumbers the amount of entorhinal cells by nearly ten-fold, which allows for the feature of "expansion recoding"--that is, a very similar

pattern of activity in a subset of overlapping entorhinal neurons can transform into more distinctive patterns of activity within non-overlapping subsets of dentate granule cells, in part due to the sheer number of available neurons for coding an experience (Amaral and Witter, 1989; Boss et al., 1985; Marr, 1969; McNaughton and Morris, 1987; McNaughton and Nadel, 1990; Myers and Scharfman, 2009; Severa et al., 2017; Treves and Rolls, 1994). In addition, granule cells exhibit sparse network activity with high levels of feedback and feedforward inhibition, a feature that is thought to facilitate active granule cells to suppress the firing of neighboring neurons (Hashimotodani et al., 2017; Luna et al., 2019). This aspect of dentate function can also permit a high likelihood of non-overlapping activity in response to similar upstream input (Aimone et al., 2011).

The phenomenon of pattern separation is visualized in the input-output activity change graphs plotted in **Figure 1.2**. Here the similarity between two arriving stimuli from either lateral or medial entorhinal cortex is visualized on the x-axis, whereas the subsequent firing differences for the DG (change in output) are shown in the y-axis. For the DG, a small input difference generates a larger output difference in DG firing (Figure 1.2, left panel), in fact, the DG decorrelates experiences to a maximum with very little input differences. This is in contrast to the downstream areas CA3 and CA1, which require larger changes in upstream activity profiles to elicit differences in firing in the output layer (Figure 1.2, middle and right panels). In these downstream regions (namely the distal parts of CA3), the function of ‘pattern completion’ is more prevalent,

whereupon incomplete input can trigger an entire network of cells to become active in association with a previously learned experience (Knierim and Zhang, 2012). Thus, the process of pattern separation at the level of DG allows unique experiences to be coded into distinct downstream networks, which can later be retrieved by partial cues in the environment via pattern completion (Knierim and Neunuebel, 2016).

Experimental evidence supports a role for the DG in pattern separation, both in animal subjects and humans. In transgenic mice lacking the NR1 subunit of the NMDA receptor within the DG, for example, they exhibit deficits in coding small contextual changes between learned fear environments, but larger distinctions between environments allows the animals to learn normally (McHugh et al., 2007). Likewise, changes in firing rates in granule cells across similar environments showed greater remapping than CA3 pyramidal cells, indicating that granule cells are sensitive to subtle contextual changes (Leutgeb et al., 2007). However, subsequent analysis of this study revealed that many of the putative granule cells in DG were likely mossy cells, which now are understood to also contribute to the process of pattern separation in DG microcircuits (GoodSmith et al., 2017, 2019; Senzai and Buzsáki, 2017). In humans, when repeated comparisons between visual objects are used (called lures), the DG is heavily recruited in an fMRI measure of brain activity, specifically when the visual differences between objects are very small (**Figure 1.2**) (Bakker et al., 2008). More recently, a case study of a patient with very selective ischemic damage to the DG bilaterally showed deficits only when discriminating between similar visual objects in a

basic discriminatin learning task (Baker et al., 2016). A common issue with human neuroimaging or lesion studies, however, is that they are unable to record directly from the DG, and damage/activity measures are usually not of sufficient high-resolution to rule out involvement of other nearby areas (Bakker et al., 2008). Although the DG is thought to participate in many more forms of learning than just pattern separation (and this process occurs within other cognitive domains and brain networks), it is a useful framework to identify the *types* of computations the DG carries out.

One common aspect of these studies on the DG is their reliance on understanding the hippocampus as a spatial map (as discussed above). Indeed, it is difficult to study the exact role of an individual or population of granule cells in their responsivity to individual elements of their physical surroundings. Any given part of the spatial context could be eliciting a response in a granule cell, and the ongoing experience of a freely moving mouse is constantly changing. Therefore, in an effort to simplify analysis, place cells offer a convenient exception to this difficulty; they sharply respond to a defined area of physical space in the animal's surroundings (Moser et al., 2008). However, the probability of finding responsive 'place cells' in the dentate gyrus is much lower than in other hippocampal subregions, due to the inherently sparse firing nature of this region (Danielson et al., 2016; Senzai and Buzsáki, 2017). Moreover, properties of single neurons and population level dynamics exceed the simple one dimension coding properties of place fields--in order to study high-dimensional processing in the DG, it is necessary to record from a large population of cells with

well-controlled stimulus space (Stefanini et al., 2020). This is one reason why studying large populations of cells in the dentate has been so difficult--they do not consistently respond to elements of the physical space, and there are relatively few studies that have examined how individual neurons or ensembles could “separate” neural input arriving from the entorhinal cortex (Danielson et al., 2016; GoodSmith et al., 2017).

Some early anatomical and physiology studies on the nonspatial roles of the hippocampus offer a unique vantage point to escape the difficulty noted above in studying dentate granule cells. In the 1970s, a simple physiology experiment by Oswald Steward demonstrated that electrical activation of olfactory bulb efferents elicited polysynaptic activity downstream measurable in the lateral entorhinal cortex (LEC) and DG (Wilson and Steward, 1978). Interestingly, if LEC was ablated, stimulation of the olfactory tract no longer generated dentate responses, whereas ablation of the medial entorhinal cortex left the olfactory tract stimulation responses intact, indicating that LEC specifically conveyed these olfactory messages to the DG (**Figure 1.3**). This was the first demonstration of a structural pathway providing olfactory input to the DG. Several decades later, this observation was complemented in a series of studies by C.H. Vanderwolf in which he subjected awake, behaving rats to odors, and measured fast wave responses in the DG with local field electrodes (Heale and Vanderwolf, 1994, 1999; Heale et al., 1994; Vanderwolf, 1992). These 15-30hz rhythmic odor-elicited responses were absent in other hippocampal subfields, and only odorants, not other sensory modality stimuli, were able to generate robust responses (Vanderwolf, 1992).

Importantly, the rats used by Vanderwolf did not learn anything in association with the odors or have previous experience--they exhibited responses upon initial presentation. The significance of a robust way to trigger reliable activity in DG granule cells is that it offers unprecedented access to their activity. Instead of spatial environments, which only elicit very sparse firing, the findings of Vanderwolf et al. indicate olfactory cues may be of use as a simple sensory stimulus to trigger widespread activation of responsive cells, and more interestingly, track changes in activity in regard to stages of memory.

The olfactory neural network is well studied in early stages of odor processing--first as distinctly activated glomeruli in the olfactory bulb (Ressler et al., 1994; Vassar et al., 1994), and later processed as ensembles coding for odor identity and intensity at the level of piriform cortex (primary olfactory cortex) (Choi et al., 2011; Giessel and Datta, 2014; Iurilli and Datta, 2017). One downstream target of both the olfactory bulb itself and the piriform cortex is the LEC (Sosulski et al., 2011), and recently, a 2-photon imaging experiment demonstrated odor-evoked responses in anesthetized mice within superficial layers of LEC (Leitner et al., 2016). Other groups have elaborated upon hippocampal involvement in odor processing--especially in the context of odor-object associations and sequence learning--but this body of work has been exclusively done in CA1 pyramidal cells (Igarashi et al., 2014; Li et al., 2017; MacDonald et al., 2013; Taxidis et al., 2020). Taken together, the existence of a entorhinal-hippocampal olfactory pathway (both to CA1 and DG) is well-evidenced,

and it could be studied with a similar type of scrutiny as the spatial cognitive map of entorhinal-hippocampal networks. Thus, the purpose of this thesis is to further contribute to the understanding of how the DG responds to odors. We aimed to see if this olfactory pathway could be leveraged to assess baseline properties of entorhinal inputs and dentate granule cell outputs, and understand changes across learning conditions.

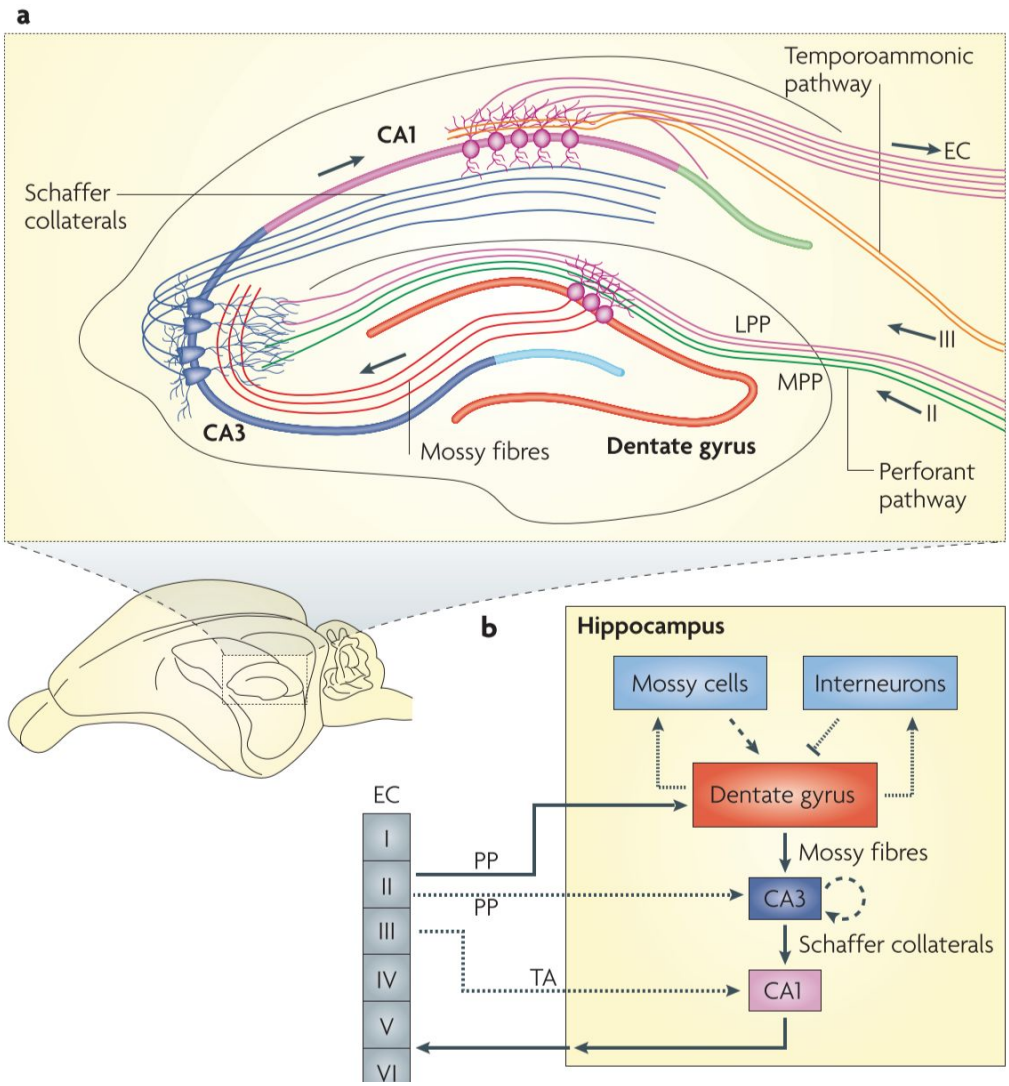

Figure 1.1: (a) The canonical trisynaptic loop is shown (solid arrows show EC-DG-CA3-CA1-EC unidirectional flow of information along principal cell layers of hippocampus), with layer II entorhinal fibers innervating the dentate gyrus and layer III axons contacting CA1 pyramidal cells. Layer II fibers originating from the MEC target the middle third of granule cell dendrites, and LEC fibers contact the outer third of granule cell dendrites in the molecular layer of the dentate gyrus. Granule cell axons form the mossy fiber pathway and terminate onto CA3 pyramidal cells. From here, CA3 pyramidal cell axons comprise the schaffer collateral pathway and contact CA1 pyramidal cells. Finally, CA1 pyramidal cells send projections that exit the hippocampus and target deep layers of entorhinal cortex. In (b), the schematic organization of the trisynaptic loop is shown. Granule cell activity in the dentate gyrus is gated by the excitation/inhibition balance established through the synchrony of mossy cells and inhibitory interneurons, which provide feedforward and feedback inhibition onto granule cells. Figure adapted from (Deng et al., 2010).

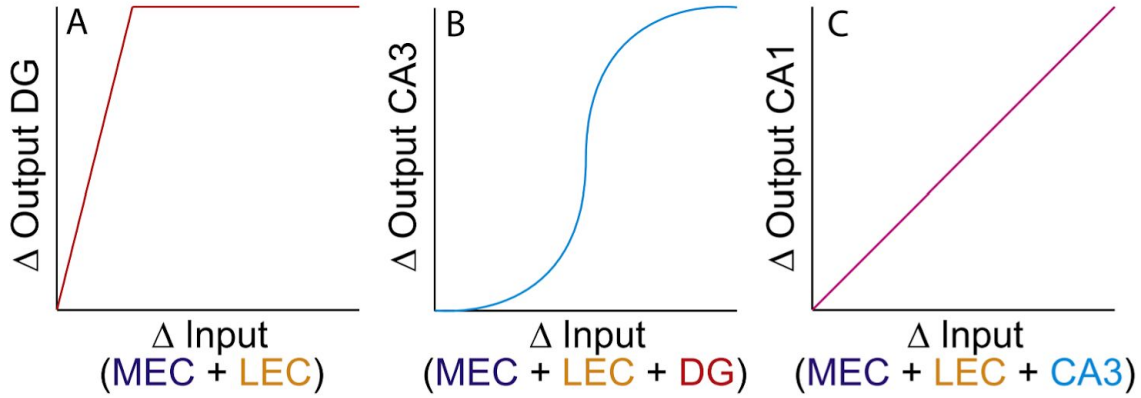

Figure 1.2: A depiction of input-output changes in hippocampal subregions. Similarity of input is depicted along the x-axis, for example, the correlated activity profiles represented in the entorhinal cortex from two experiences. With a very small change in input differences, the resulting activity profile downstream in DG is highly non-overlapping, reaching its maximum separation at very low levels of difference in input (left). The CA3 region, on the other hand, requires a large separation between inputs to form distinct responses (middle). CA1, finally, is thought to respond in a linear fashion from entorhinal input (right). Figure adapted from (Knierim and Neunuebel, 2016).

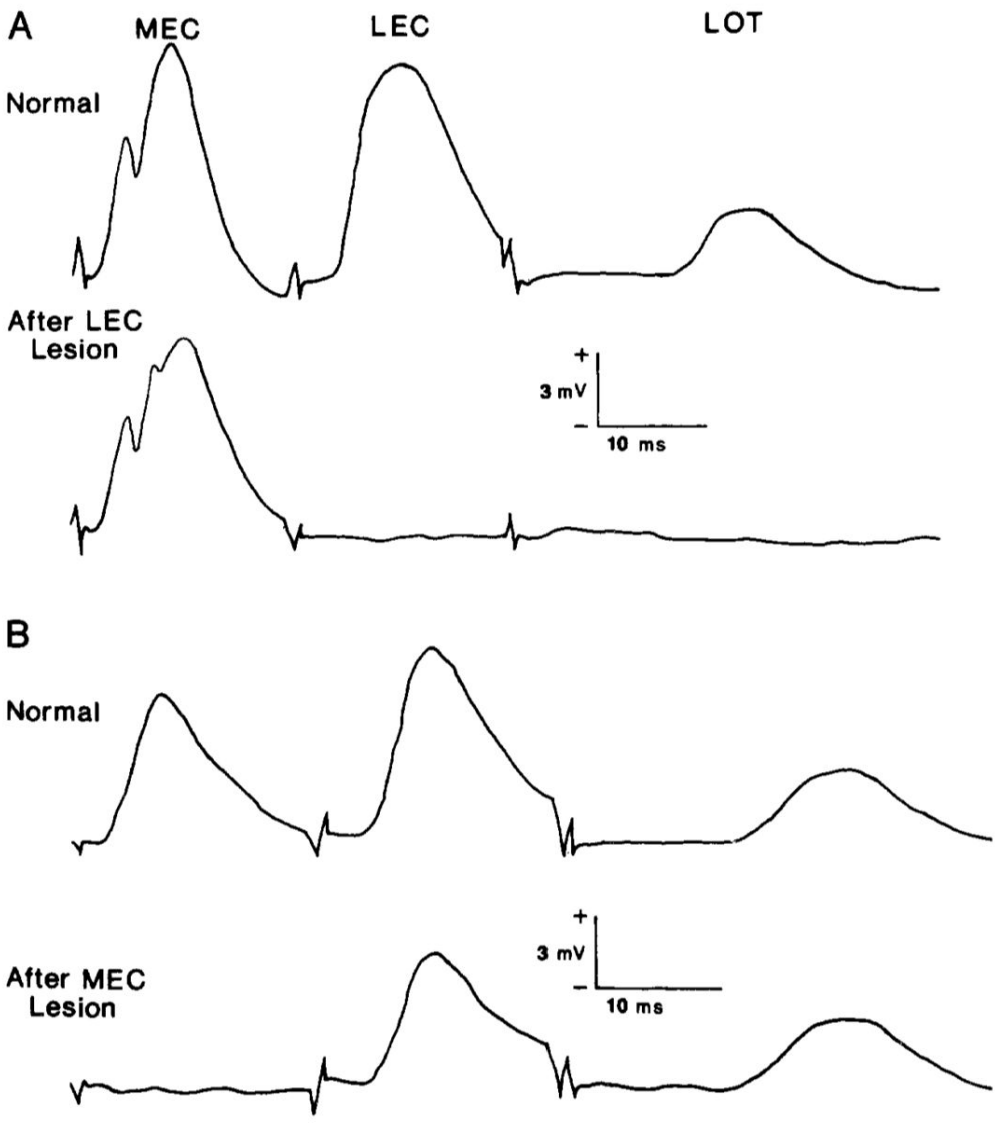

Figure 1.3: The first demonstration of a polysynaptic olfactory-pathway originating in the olfactory bulb and propagating to the dentate gyrus. Extracellular evoked potentials are measured in the dentate gyrus after stimulation of the medial entorhinal cortex (MEC), lateral entorhinal cortex (LEC), or lateral olfactory tract (LOT). In a normal (intact) animal, stimulation of olfactory fibers evokes a distinct response in DG. To determine if the olfactory message is conveyed via MEC or LEC fibers, Wilson and Steward lesioned either the LEC or MEC, and elicited potentials as above. After LEC lesion, the MEC response was intact, but the LOT elicited field potentials were eliminated. MEC lesions left the LOT evoked-potential intact, indicating that LEC conveys the olfactory information to DG. Figure adapted from (Wilson and Steward, 1978).

References for Chapter 1

Acsady, L., Kamondi, A., Sık, A., Freund, T., and Buzsáki, G. (1998). GABAergic cells are the major postsynaptic targets of mossy fibers in the rat hippocampus. Journal of Neuroscience *18*, 3386–3403.

Addis, D.R., and Tippett, L.J. (2004). Memory of myself: autobiographical memory and identity in Alzheimer's disease. Memory *12*, 56–74.

Aimone, J.B., Deng, W., and Gage, F.H. (2011). Resolving new memories: a critical look at the dentate gyrus, adult neurogenesis, and pattern separation. Neuron *70*, 589–596.

Alme, C.B., Miao, C., Jezek, K., Treves, A., Moser, E.I., and Moser, M.-B. (2014). Place cells in the hippocampus: eleven maps for eleven rooms. Proc. Natl. Acad. Sci. U. S. A. *111*, 18428–18435.

Amaral, D.G., and Witter, M.P. (1989). The three-dimensional organization of the hippocampal formation: A review of anatomical data. Neuroscience *31*, 571–591.

Andersen, P., Holmqvist, B., and Voorhoeve, P.E. (1966). Entorhinal activation of dentate granule cells. Acta Physiol. Scand. *66*, 448–460.

Annese, J., Schenker-Ahmed, N.M., Bartsch, H., Maechler, P., Sheh, C., Thomas, N., Kayano, J., Ghatan, A., Bresler, N., Frosch, M.P., et al. (2014). Postmortem examination of patient HM's brain based on histological sectioning and digital 3D

reconstruction. Nat. Commun. *5*, 1–9.

Aronov, D., Nevers, R., and Tank, D.W. (2017). Mapping of a non-spatial dimension by the hippocampal–entorhinal circuit. Nature.

Augustinack, J.C., van der Kouwe, A.J.W., Salat, D.H., Benner, T., Stevens, A.A., Annese, J., Fischl, B., Frosch, M.P., and Corkin, S. (2014). H.M.'s contributions to neuroscience: A review and autopsy studies. Hippocampus *24*, 1267–1286.

Baker, S., Vieweg, P., Gao, F., Gilboa, A., Wolbers, T., Black, S.E., and Rosenbaum, R.S. (2016). The Human Dentate Gyrus Plays a Necessary Role in Discriminating New Memories. Curr. Biol. *26*, 2629–2634.

Bakker, A., Kirwan, C.B., Miller, M., and Stark, C.E.L. (2008). Pattern separation in the human hippocampal CA3 and dentate gyrus. Science *319*, 1640–1642.

Bishop, N.A., Lu, T., and Yankner, B.A. (2010). Neural mechanisms of ageing and cognitive decline. Nature *464*, 529–535.

Boss, B.D., Peterson, G.M., and Cowan, W.M. (1985). On the number of neurons in the dentate gyrus of the rat. Brain Res. *338*, 144–150.

Brun, V.H., Leutgeb, S., Wu, H.-Q., Schwarcz, R., Witter, M.P., Moser, E.I., and Moser, M.-B. (2008). Impaired Spatial Representation in CA1 after Lesion of Direct Input from Entorhinal Cortex. Neuron *57*, 290–302.

Choi, G.B., Stettler, D.D., Kallman, B.R., Bhaskar, S.T., Fleischmann, A., and Axel, R. (2011). Driving opposing behaviors with ensembles of piriform neurons. Cell *146*, 1004–1015.

Clelland, C.D., Choi, M., Romberg, C., Clemenson, G.D., Jr, Fragniere, A., Tyers, P., Jessberger, S., Saksida, L.M., Barker, R.A., Gage, F.H., et al. (2009). A functional role for adult hippocampal neurogenesis in spatial pattern separation. Science *325*, 210–213.

Danielson, N.B., Kaifosh, P., Zaremba, J.D., Lovett-Barron, M., Tsai, J., Denny, C.A., Balough, E.M., Goldberg, A.R., Drew, L.J., Hen, R., et al. (2016). Distinct Contribution of Adult-Born Hippocampal Granule Cells to Context Encoding. Neuron *90*, 101–112.

Deller, T. (1998). The anatomical organization of the rat fascia dentata: new aspects of laminar organization as revealed by anterograde tracing with Phaseolus vulgaris-Leucoagglutinin (PHAL). Anat. Embryol. *197*, 89–103.

Deng, W., Aimone, J.B., and Gage, F.H. (2010). New neurons and new memories: how does adult hippocampal neurogenesis affect learning and memory? Nat. Rev. Neurosci. *11*, 339–350.

Dere, E., Kart-Teke, E., Huston, J.P., and De Souza Silva, M.A. (2006). The case for episodic memory in animals. Neurosci. Biobehav. Rev. *30*, 1206–1224.

Deshmukh, S.S., and Knierim, J.J. (2011). Representation of non-spatial and spatial

information in the lateral entorhinal cortex. Front. Behav. Neurosci. *5*, 69.

Eichenbaum, H. (1992). The hippocampal system and declarative memory in animals. J. Cogn. Neurosci. *4*, 217–231.

Eichenbaum, H. (2017). Memory: Organization and Control. Annu. Rev. Psychol. *68*, 19–45.

Eichenbaum, H., Yonelinas, A.P., and Ranganath, C. (2007). The medial temporal lobe and recognition memory. Annu. Rev. Neurosci. *30*, 123–152.

Ferbinteanu, J., Holsinger, R.M., and McDonald, R.J. (1999). Lesions of the medial or lateral perforant path have different effects on hippocampal contributions to place learning and on fear conditioning to context. Behav. Brain Res. *101*, 65–84.

Fredes, F., Silva, M.A., Koppensteiner, P., Kobayashi, K., Joesch, M., and Shigemoto, R. (2020). Ventro-dorsal Hippocampal Pathway Gates Novelty-Induced Contextual Memory Formation. Curr. Biol. *0*.

Freund, T.F., and Buzsaki, G. (1996). Interneurons of the hippocampus. Hippocampus *6*, 347–470.

Fyhn, M., Molden, S., Witter, M.P., Moser, E.I., and Moser, M.-B. (2004). Spatial representation in the entorhinal cortex. Science *305*, 1258–1264.

Giessel, A.J., and Datta, S.R. (2014). Olfactory maps, circuits and computations. Curr.

Opin. Neurobiol. *24*, 120–132.

GoodSmith, D., Chen, X., Wang, C., Kim, S.H., Song, H., Burgalossi, A., Christian, K.M., and Knierim, J.J. (2017). Spatial Representations of Granule Cells and Mossy Cells of the Dentate Gyrus. Neuron *93*, 677–690.e5.

GoodSmith, D., Lee, H., Neunuebel, J.P., Song, H., and Knierim, J.J. (2019). Dentate Gyrus Mossy Cells Share a Role in Pattern Separation with Dentate Granule Cells and Proximal CA3 Pyramidal Cells. J. Neurosci. *39*, 9570–9584.

van Groen, T. (2001). Entorhinal cortex of the mouse: cytoarchitectonical organization. Hippocampus *11*, 397–407.

van Groen, T., Miettinen, P., and Kadish, I. (2003). The entorhinal cortex of the mouse: organization of the projection to the hippocampal formation. Hippocampus *13*, 133–149.

Hafting, T., Fyhn, M., Molden, S., Moser, M.-B., and Moser, E.I. (2005). Microstructure of a spatial map in the entorhinal cortex. Nature *436*, 801–806.

Hainmueller, T., and Bartos, M. (2020). Dentate gyrus circuits for encoding, retrieval and discrimination of episodic memories. Nat. Rev. Neurosci. 1–16.

Hargreaves, E.L., Rao, G., Lee, I., and Knierim, J.J. (2005). Major dissociation between medial and lateral entorhinal input to dorsal hippocampus. Science *308*, 1792–1794.

Hashimotodani, Y., Nasrallah, K., Jensen, K.R., Chávez, A.E., Carrera, D., and Castillo, P.E. (2017). LTP at Hilar Mossy Cell-Dentate Granule Cell Synapses Modulates Dentate Gyrus Output by Increasing Excitation/Inhibition Balance. Neuron *95*, 928–943.e3.

Heale, V.R., and Vanderwolf, C.H. (1994). Dentate gyrus and olfactory bulb responses to olfactory and noxious stimulation in urethane anaesthetized rats. Brain Res. *652*, 235–242.

Heale, V.R., and Vanderwolf, C.H. (1999). Odor-induced fast waves in the dentate gyrus depend on a pathway through posterior cerebral cortex: effects of limbic lesions and trimethyltin. Brain Res. Bull. *50*, 291–299.

Heale, V.R., Vanderwolf, C.H., and Kavaliers, M. (1994). Components of weasel and fox odors elicit fast wave bursts in the dentate gyrus of rats. Behav. Brain Res. *63*, 159–165.

Henze, D.A., Wittner, L., and Buzsáki, G. (2002). Single granule cells reliably discharge targets in the hippocampal CA3 network in vivo. Nat. Neurosci. *5*, 790–795.

Hjorth-Simonsen, A., and Jeune, B. (1972). Origin and termination of the hippocampal perforant path in the rat studied by silver impregnation. J. Comp. Neurol. *144*, 215–231.

Høydal, Ø.A., Skytøen, E.R., Andersson, S.O., Moser, M.-B., and Moser, E.I. (2019). Object-vector coding in the medial entorhinal cortex. Nature *568*, 400–404.

Hunsaker, M.R., Mooy, G.G., Swift, J.S., and Kesner, R.P. (2007). Dissociations of the medial and lateral perforant path projections into dorsal DG, CA3, and CA1 for spatial and nonspatial (visual object) information processing. Behav. Neurosci. *121*, 742–750.

Igarashi, K.M., Lu, L., Colgin, L.L., Moser, M.-B., and Moser, E.I. (2014). Coordination of entorhinal–hippocampal ensemble activity during associative learning. Nature *510*, 143–147.

Iurilli, G., and Datta, S.R. (2017). Population Coding in an Innately Relevant Olfactory Area. Neuron *93*, 1180–1197.e7.

Jimenez, J.C., Su, K., Goldberg, A.R., Luna, V.M., Biane, J.S., Ordek, G., Zhou, P., Ong, S.K., Wright, M.A., Zweifel, L., et al. (2018). Anxiety Cells in a Hippocampal-Hypothalamic Circuit. Neuron *97*, 670–683.e6.

Kesner, R.P. (2013). An analysis of the dentate gyrus function. Behav. Brain Res. *254*, 1–7.

Kesner, R.P., Hunsaker, M.R., and Ziegler, W. (2011). The role of the dorsal and ventral hippocampus in olfactory working memory. Neurobiol. Learn. Mem. *96*, 361–366.

Khan, U.A., Liu, L., Provenzano, F.A., Berman, D.E., Profaci, C.P., Sloan, R., Mayeux, R., Duff, K.E., and Small, S.A. (2014). Molecular drivers and cortical spread of lateral entorhinal cortex dysfunction in preclinical Alzheimer's disease. Nat. Neurosci. *17*, 304–311.

Kheirbek, M.A., Drew, L.J., Burghardt, N.S., Costantini, D.O., Tannenholz, L., Ahmari, S.E., Zeng, H., Fenton, A.A., and Hen, R. (2013). Differential control of learning and anxiety along the dorsoventral axis of the dentate gyrus. Neuron *77*, 955–968.

Kim, S., Jung, D., and Royer, S. (2020). Place cell maps slowly develop via competitive learning and conjunctive coding in the dentate gyrus. Nat. Commun. *11*, 4550.

Knierim, J.J., and Neunuebel, J.P. (2016). Tracking the flow of hippocampal computation: Pattern separation, pattern completion, and attractor dynamics. Neurobiol. Learn. Mem. *129*, 38–49.

Knierim, J.J., and Zhang, K. (2012). Attractor dynamics of spatially correlated neural activity in the limbic system. Annu. Rev. Neurosci. *35*, 267–285.

Knierim, J.J., Neunuebel, J.P., and Deshmukh, S.S. (2014). Functional correlates of the lateral and medial entorhinal cortex: objects, path integration and local-global reference frames. Philos. Trans. R. Soc. Lond. B Biol. Sci. *369*, 20130369.

Kropff, E., Carmichael, J.E., Moser, M.-B., and Moser, E.I. (2015). Speed cells in the medial entorhinal cortex. Nature *523*, 419–424.

Leitner, F.C., Melzer, S., Lütcke, H., Pinna, R., Seeburg, P.H., Helmchen, F., and Monyer, H. (2016). Spatially segregated feedforward and feedback neurons support differential odor processing in the lateral entorhinal cortex. Nat. Neurosci. *19*, 935–944.

Leutgeb, J.K., Leutgeb, S., Moser, M.-B., and Moser, E.I. (2007). Pattern separation in

the dentate gyrus and CA3 of the hippocampus. Science *315*, 961–966.

Leutgeb, S., Leutgeb, J.K., Treves, A., Moser, M.-B., and Moser, E.I. (2004). Distinct ensemble codes in hippocampal areas CA3 and CA1. Science *305*, 1295–1298.

Li, Y., Xu, J., Liu, Y., Zhu, J., Liu, N., Zeng, W., Huang, N., Rasch, M.J., Jiang, H., Gu, X., et al. (2017). A distinct entorhinal cortex to hippocampal CA1 direct circuit for olfactory associative learning. Nat. Neurosci. *20*, 559–570.

Lømo, T. (1971). Patterns of activation in a monosynaptic cortical pathway: the perforant path input to the dentate area of the hippocampal formation. Exp. Brain Res.

Luna, V.M., Anacker, C., Burghardt, N.S., Khandaker, H., Andreu, V., Millette, A., Leary, P., Ravenelle, R., Jimenez, J.C., Mastrodonato, A., et al. (2019). Adult-born hippocampal neurons bidirectionally modulate entorhinal inputs into the dentate gyrus. Science *364*, 578–583.

MacDonald, C.J., Carrow, S., Place, R., and Eichenbaum, H. (2013). Distinct hippocampal time cell sequences represent odor memories in immobilized rats. J. Neurosci. *33*, 14607–14616.

Marr, D. (1969). A theory of cerebellar cortex. J. Physiol. *202*, 437–470.

Masurkar, A.V., Srinivas, K.V., Brann, D.H., Warren, R., Lowes, D.C., and Siegelbaum, S.A. (2017). Medial and Lateral Entorhinal Cortex Differentially Excite Deep versus Superficial CA1 Pyramidal Neurons. Cell Rep. *18*, 148–160.

McHugh, T.J., Jones, M.W., Quinn, J.J., Balthasar, N., Coppari, R., Elmquist, J.K., Lowell, B.B., Fanselow, M.S., Wilson, M.A., and Tonegawa, S. (2007). Dentate gyrus NMDA receptors mediate rapid pattern separation in the hippocampal network. Science *317*, 94–99.

McNaughton, B.L., and Morris, R.G.M. (1987). Hippocampal synaptic enhancement and information storage within a distributed memory system. Trends Neurosci. *10*, 408–415.

McNaughton, B.L., and Nadel, L. (1990). Hebb-Marr networks and the neurobiological representation of action in space. Neuroscience and Connectionist Theory 1–63.

McNaughton, B.L., Battaglia, F.P., Jensen, O., Moser, E.I., and Moser, M.-B. (2006). Path integration and the neural basis of the'cognitive map'. Nat. Rev. Neurosci. *7*, 663.

Michael, F., and László, S. (2006). Morphological Development of the Hippocampus. The Hippocampus Book 115–132.

Miles, R., Le Duigou, C., Simonnet, J., Telenczuk, M., and Fricker, D. (2014). Recurrent synapses and circuits in the CA3 region of the hippocampus: an associative network. Front. Cell. Neurosci. *7*, 262.

Milner, B., Corkin, S., and Teuber, H.-L. (1968). Further analysis of the hippocampal amnesic syndrome: 14-year follow-up study of H.M. Neuropsychologia *6*, 215–234.

Ming, G.-L., and Song, H. (2011). Adult neurogenesis in the mammalian brain:

significant answers and significant questions. Neuron *70*, 687–702.

Moser, E.I., Kropff, E., and Moser, M.-B. (2008). Place cells, grid cells, and the brain's spatial representation system. Annu. Rev. Neurosci. *31*, 69–89.

Myers, C.E., and Scharfman, H.E. (2009). A role for hilar cells in pattern separation in the dentate gyrus: a computational approach. Hippocampus *19*, 321–337.

Nakashiba, T., Cushman, J.D., Pelkey, K.A., Renaudineau, S., Buhl, D.L., McHugh, T.J., Rodriguez Barrera, V., Chittajallu, R., Iwamoto, K.S., McBain, C.J., et al. (2012). Young dentate granule cells mediate pattern separation, whereas old granule cells facilitate pattern completion. Cell *149*, 188–201.

Nicoll, R.A., and Schmitz, D. (2005). Synaptic plasticity at hippocampal mossy fibre synapses. Nat. Rev. Neurosci. *6*, 863–876.

Nilssen, E.S., Doan, T.P., Nigro, M.J., Ohara, S., and Witter, M.P. (2019). Neurons and networks in the entorhinal cortex: A reappraisal of the lateral and medial entorhinal subdivisions mediating parallel cortical pathways. Hippocampus *29*, 1238–1254.

O'Keefe, J., and Dostrovsky, J. (1971). The hippocampus as a spatial map. Preliminary evidence from unit activity in the freely-moving rat. Brain Res. *34*, 171–175.

O'keefe, J., and Nadel, L. (1978). The hippocampus as a cognitive map (Oxford: Clarendon Press).

Okuyama, T., Kitamura, T., Roy, D.S., Itohara, S., and Tonegawa, S. (2016). Ventral CA1 neurons store social memory. Science *353*, 1536–1541.

Olton, D.S., Becker, J.T., and Handelmann, G.E. (1979). Hippocampus, space, and memory. Behav. Brain Sci. *2*, 313–322.

Overstreet-Wadiche, L.S., and Westbrook, G.L. (2006). Functional maturation of adult-generated granule cells. Hippocampus *16*, 208–215.

Phinney, A.L., Calhoun, M.E., Woods, A.G., Deller, T., and Jucker, M. (2004). Stereological analysis of the reorganization of the dentate gyrus following entorhinal cortex lesion in mice. Eur. J. Neurosci. *19*, 1731–1740.

Reagh, Z.M., and Yassa, M.A. (2014). Object and spatial mnemonic interference differentially engage lateral and medial entorhinal cortex in humans. Proc. Natl. Acad. Sci. U. S. A. *111*, E4264–E4273.

Ressler, K.J., Sullivan, S.L., and Buck, L.B. (1994). Information coding in the olfactory system: evidence for a stereotyped and highly organized epitope map in the olfactory bulb. Cell *79*, 1245–1255.

Rolls, E.T. (2013). The mechanisms for pattern completion and pattern separation in the hippocampus. Front. Syst. Neurosci. *7*, 74.

Rolls, E.T., Treves, A., and Rolls, E.T. (1998). Neural networks and brain function.

Rosenbaum, R.S., Priselac, S., Köhler, S., Black, S.E., Gao, F., Nadel, L., and Moscovitch, M. (2000). Remote spatial memory in an amnesic person with extensive bilateral hippocampal lesions. Nat. Neurosci. *3*, 1044–1048.

Rosenbaum, R.S., Gilboa, A., and Moscovitch, M. (2014). Case studies continue to illuminate the cognitive neuroscience of memory. Ann. N. Y. Acad. Sci. *1316*, 105–133.

Rotenberg, A., Mayford, M., Hawkins, R.D., Kandel, E.R., and Muller, R.U. (1996). Mice expressing activated CaMKII lack low frequency LTP and do not form stable place cells in the CA1 region of the hippocampus. Cell *87*, 1351–1361.

Sahay, A., Scobie, K.N., Hill, A.S., O'Carroll, C.M., Kheirbek, M.A., Burghardt, N.S., Fenton, A.A., Dranovsky, A., and Hen, R. (2011). Increasing adult hippocampal neurogenesis is sufficient to improve pattern separation. Nature *472*, 466–470.

Scharfman, H.E. (2016). The enigmatic mossy cell of the dentate gyrus. Nat. Rev. Neurosci. *17*, 562–575.

Scharfman, H.E. (2018). Advances in understanding hilar mossy cells of the dentate gyrus. Cell Tissue Res. *373*, 643–652.

Scoville, W.B., and Milner, B. (1957). Loss of recent memory after bilateral hippocampal lesions. J. Neurol. Neurosurg. Psychiatry *20*, 11–21.

Senzai, Y., and Buzsáki, G. (2017). Physiological Properties and Behavioral Correlates of Hippocampal Granule Cells and Mossy Cells. Neuron *93*, 691–704.e5.

Severa, W., Parekh, O., James, C.D., and Aimone, J.B. (2017). A Combinatorial Model for Dentate Gyrus Sparse Coding. Neural Comput. *29*, 94–117.

Solstad, T., Boccara, C.N., Kropff, E., Moser, M.-B., and Moser, E.I. (2008). Representation of geometric borders in the entorhinal cortex. Science *322*, 1865–1868.

Sosulski, D.L., Bloom, M.L., Cutforth, T., Axel, R., and Datta, S.R. (2011). Distinct representations of olfactory information in different cortical centres. Nature *472*, 213–216.

Spear, N.E. (1973). Retrieval of memory in animals. Psychol. Rev. *80*, 163–194.

Squire, L.R. (1992). Memory and the hippocampus: a synthesis from findings with rats, monkeys, and humans. Psychol. Rev. *99*, 195–231.

Squire, L.R., and Knowlton, B.J. (1995). Memory, hippocampus, and brain systems.

Stanfield, B.B., and Cowan, W.M. (1979). The development of the hippocampus and dentate gyrus in normal and reeler mice. J. Comp. Neurol. *185*, 423–459.

Stefanini, F., Kushnir, L., Jimenez, J.C., Jennings, J.H., Woods, N.I., Stuber, G.D., Kheirbek, M.A., Hen, R., and Fusi, S. (2020). A Distributed Neural Code in the Dentate Gyrus and in CA1. Neuron.

Stein, J.F. (1989). Representation of egocentric space in the posterior parietal cortex. Q. J. Exp. Physiol. *74*, 583–606.

Strange, B.A., Witter, M.P., Lein, E.S., and Moser, E.I. (2014). Functional organization of the hippocampal longitudinal axis. Nat. Rev. Neurosci. *15*, 655–669.

van Strien, N.M., Cappaert, N.L.M., and Witter, M.P. (2009). The anatomy of memory: an interactive overview of the parahippocampal–hippocampal network. Nat. Rev. Neurosci. *10*, 272–282.

Taxidis, J., Pnevmatikakis, E.A., Dorian, C.C., Mylavarapu, A.L., Arora, J.S., Samadian, K.D., Hoffberg, E.A., and Golshani, P. (2020). Differential Emergence and Stability of Sensory and Temporal Representations in Context-Specific Hippocampal Sequences. Neuron.

Tolman, E.C. (1948). Cognitive maps in rats and men. Psychol. Rev. *55*, 189–208.

Treves, A., and Rolls, E.T. (1994). Computational analysis of the role of the hippocampus in memory. Hippocampus *4*, 374–391.

Tronel, S., Belnoue, L., Grosjean, N., Revest, J.-M., Piazza, P.-V., Koehl, M., and Abrous, D.N. (2012). Adult-born neurons are necessary for extended contextual discrimination. Hippocampus *22*, 292–298.

Tsao, A., Moser, M.-B., and Moser, E.I. (2013). Traces of experience in the lateral entorhinal cortex. Curr. Biol. *23*, 399–405.

Tulving, E., and Markowitsch, H.J. (1998). Episodic and declarative memory: role of the hippocampus. Hippocampus *8*, 198–204.

Van Cauter, T., Camon, J., Alvernhe, A., Elduayen, C., Sargolini, F., and Save, E. (2013). Distinct roles of medial and lateral entorhinal cortex in spatial cognition. Cereb. Cortex *23*, 451–459.

Vanderwolf, C.H. (1992). Hippocampal activity, olfaction, and sniffing: an olfactory input to the dentate gyrus. Brain Res. *593*, 197–208.

Vassar, R., Chao, S.K., Sitcheran, R., Nuñez, J.M., Vosshall, L.B., and Axel, R. (1994). Topographic organization of sensory projections to the olfactory bulb. Cell *79*, 981–991.

Wang, C., Chen, X., Lee, H., Deshmukh, S.S., Yoganarasimha, D., Savelli, F., and Knierim, J.J. (2018). Egocentric coding of external items in the lateral entorhinal cortex. Science *362*, 945–949.

Wilson, R.C., and Steward, O. (1978). Polysynaptic activation of the dentate gyrus of the hippocampal formation: an olfactory input via the lateral entorhinal cortex. Exp. Brain Res. *33*, 523–534.

Witter, M.P. (2007). The perforant path: projections from the entorhinal cortex to the dentate gyrus. Prog. Brain Res. *163*, 43–61.

Witter, M.P., Doan, T.P., Jacobsen, B., Nilssen, E.S., and Ohara, S. (2017). Architecture of the Entorhinal Cortex A Review of Entorhinal Anatomy in Rodents with Some Comparative Notes. Front. Syst. Neurosci. *11*, 46.

Woods, N.I., Vaaga, C.E., Chatzi, C., Adelson, J.D., Collie, M.F., Perederiy, J.V., Tovar, K.R., and Westbrook, G.L. (2018). Preferential Targeting of Lateral Entorhinal Inputs onto Newly Integrated Granule Cells. J. Neurosci. *38*, 5843–5853.

Yassa, M.A., and Stark, C.E.L. (2011). Pattern separation in the hippocampus. Trends Neurosci. *34*, 515–525.

Yasuda, M., and Mayford, M.R. (2006). CaMKII activation in the entorhinal cortex disrupts previously encoded spatial memory. Neuron *50*, 309–318.

Yoganarasimha, D., Rao, G., and Knierim, J.J. (2011). Lateral entorhinal neurons are not spatially selective in cue-rich environments. Hippocampus *21*, 1363–1374.

Zeidman, P., and Maguire, E.A. (2016). Anterior hippocampus: the anatomy of perception, imagination and episodic memory. Nat. Rev. Neurosci. *17*, 173–182.

Zhang, S.-J., Ye, J., Couey, J.J., Witter, M., Moser, E.I., and Moser, M.-B. (2014). Functional connectivity of the entorhinal-hippocampal space circuit. Philos. Trans. R. Soc. Lond. B Biol. Sci. *369*, 20120516.

Zhang, X., Schlögl, A., and Jonas, P. (2020). Selective Routing of Spatial Information Flow from Input to Output in Hippocampal Granule Cells. Neuron *107*, 1212–1225.e7.

Ziv, Y., Burns, L.D., Cocker, E.D., Hamel, E.O., Ghosh, K.K., Kitch, L.J., El Gamal, A., and Schnitzer, M.J. (2013). Long-term dynamics of CA1 hippocampal place codes. Nat. Neurosci. *16*, 264–266.

Chapter 2: The dentate gyrus classifies cortical representations of learned stimuli

Introduction

Animals have a cognitive map of their surroundings that is constantly updated to optimize behavior (McNaughton et al., 2006; Olton et al., 1979). Any given element of their surroundings may not carry immediate meaning, but with reinforcement, animals will learn to approach or avoid cues that predict salient outcomes and ignore others. How the brain discerns stimuli, and transforms an initially irrelevant stimulus into something meaningful that can be retrieved for future action, remains largely unclear. One way that neural populations may implement this form of encoding is by increasing the distance between neural representations of cues through the process of learning, effectively "separating" a salient from a non-salient stimulus.

One potential locus of this computation may be the hippocampus (HPC), which not only contributes to spatial navigation and memory (Eichenbaum et al., 2007; Olton et al., 1979; Tulving and Markowitsch, 1998), but also encodes non-spatial stimuli and the relationship between these behaviorally relevant variables (Aronov et al., 2017a; Igarashi et al., 2014; Li et al., 2017; MacDonald et al., 2013; Martin et al., 2007). However, how experience can impact the representations of non-spatial stimuli in the HPC has remained largely unexplored. Here, we turned to olfactory stimuli to investigate how DG GCs encode and separate incoming sensory information. Early anatomists noted the extensive connectivity and

proximate location of the hippocampus with other parts of the olfactory system, and accordingly included the hippocampus as a central node in the rhinencephalon, or “nose brain” (Broca, 1878; Eichenbaum and Otto, 1992). Subsequent electrophysiological studies revealed that odorants were uniquely capable as sensory stimuli in eliciting a burst of activity in the DG, however, technical constraints limited a more complete understanding of how the DG encodes and processes this information (Vanderwolf, 1992; Wilson and Steward, 1978). Extensive work has elucidated how olfactory information is represented at initial sensory processing centers, such as the olfactory bulb and piriform cortex (Bathellier et al., 2008; Bolding and Franks, 2017; Iurilli and Datta, 2017; Meister and Bonhoeffer, 2001; Roland et al., 2017; Sosulski et al., 2011; Stettler and Axel, 2009; Uchida and Mainen, 2003; Xu and Wilson, 2012), yet, little is known of the logic by which odorant stimuli are represented or learned within the DG. Anatomical studies suggest odor-related information is transmitted to the DG via inputs from the LEC (Eichenbaum et al., 2007; Hargreaves et al., 2005; Leitner et al., 2016; Witter et al., 2017), which itself receives olfactory inputs via both direct projections from the olfactory bulb and afferents originating in the piriform cortex and cortical amygdala (Heale and Vanderwolf, 1994, 1999; Krettek and Price, 1977; Leitner et al., 2016; Room et al., 1984; Shipley and Adamek, 1984; Vanderwolf, 1992; Wilson and Steward, 1978). In addition, the DG has been hypothesized to disambiguate cortical representation of sensory stimuli, so as to create less or non-overlapping outputs to the downstream CA3 subfield of the HPC (Aimone et al., 2011; Knierim and Neunuebel, 2016; Yassa and Stark, 2011). However, how learning

impacts this process, and whether olfactory representations are separated at the level of DG neural activity, remains largely unknown.

In order to understand how the DG classifies cortical representations of salient olfactory stimuli, we performed in vivo chronic 2-photon imaging of the LEC and DG. We investigated 1) how DG GCs and LEC neurons represent olfactory stimuli, 2) whether LEC is the main input for olfactory information to DG, and 3) how DG GCs and LEC neurons change their responses with learning. We found that odor identity is robustly represented in the DG, and that the degree to which the DG classified odorants was directly related to discrimination of these cues during context recall. Odors were more accurately classified in populations of cells within the DG than LEC, and with learning the DG GCs flexibly changed their representations of odor stimuli more so than LEC neurons, increasing the distance in neural representation between stimuli and responding more to the conditioned odorant. These data reveal that DG GCs are a key node of the extended network that represents the olfactory world and for learning the associations between olfactory stimuli and behaviorally relevant outcomes.

Results

Representations of olfactory stimuli in LEC and DG

To determine if odor information is represented in the DG, we performed chronic high resolution 2-photon calcium imaging of DG GCs in awake, head-fixed mice (Danielson et al., 2016). We visualized GC activity by injecting AAV-DJ-CaMKII-GCaMP6f into the DG and

imaged fields of view (FOVs) within the DG granule cell layer (GCL, **Figure 2.1A-B**). To characterize baseline responses to odorants, mice were imaged during delivery of a panel of diverse monomolecular odorants (**Figure 2.1A**). Olfactory stimuli evoked robust responses in a fraction of GCs (**Figures 2.1C, S2.1D,G, and S2.2B-C**) that remained stable across multiple trials (**Figure 2.1D**). As is also the case for odor-evoked responses in upstream piriform cortex (Roland et al., 2017; Stettler and Axel, 2009) which innervates LEC, (Heale and Vanderwolf, 1994, 1999; Krettek and Price, 1977; Leitner et al., 2016; Room et al., 1984; Shipley and Adamek, 1984; Vanderwolf, 1992; Wilson and Steward, 1978), odor-modulated GCs were distributed across the FOV without apparent spatial clustering (**Figures 2.1E, S2.1F, and S2.2A**). In order to understand how odor information may be differentially represented in the DG and its upstream input, LEC, we developed a method for 2-photon imaging of GCaMP6f-expressing LEC neurons in awake head-fixed mice (**Figure 2.2B**). As in DG, a subset of LEC neurons showed time-locked responses to odor delivery, with no discernable spatial clustering of modulated cells (**Figure 2.2A-C and S2.1E and S2.2B-C**).

We next sought to compare odor responses in LEC neurons, DG GCs and DG GCs in which input from LEC was inhibited. In our six-odor delivery design, we imaged DG GCs, LEC neurons, and DG GCs from mice in which we silenced LEC-DG synaptic transmission using tetanus toxin light chain (LEC-DG TeLC, see Methods) (**Figure 2.3A and S2.1C**). The identity of presented odorants could be accurately decoded using linear decoders (Bishop, 2006) from the population activity of DG GCs and LEC neurons, but not from LEC-DG TeLC mice (Figures 3B-C, S2D-F, see Methods), suggesting the LEC is the major source of odor input to

the DG. By comparing decoding accuracies in LEC and DG, we found that a decoder trained on DG GC data could more accurately classify odor identity than one trained on LEC activities, suggesting that odor identity is more reliably represented in DG than LEC (**Figure 2.3C**). This was true both in experiments using a 6 odor panel and a 3 odor panel (**Figure S2.2D-E**). We obtained complementary results by constructing population vectors of DG GCs or LEC activity during odor presentations and measuring trial by trial similarity; we found responses across odors were less correlated in DG when compared to LEC (**Figures 2.3E, S2.2G-H**), indicating that distinct odor representations are decorrelated in DG compared to LEC, and that odor correlations were disrupted in LEC-DG TeLC mice (**Figure 2.3E**). Finally, we constructed a model based on random connectivity (Schaffer et al., 2018) between LEC and the target GCs (see Methods) to determine if this could recapitulate the high decoding accuracy in DG GCs seen in our data. The property of random connectivity in the model maintained correlations in odor representations within the input structure (LEC) and enabled expansion of the dimensionality of patterns onto its output structure (DG), via a non-linear transformation, which in general can be beneficial for decoding (Rigotti et al., 2010). However, random connectivity alone, at all tested DG sparsity levels in our model, was not sufficient to obtain the high decoding performance we observed in our DG recordings, using either the six odor panel or the three odor panel (**Figures S2.2G-H**). These data suggest that LEC input to DG is required for odor classification, and that local circuit operations within the DG itself may enhance odor representations rather than arising solely from random connectivity between LEC and DG.

Odor classification accuracy in the DG is related to behavioral discrimination in an odor-guided contextual memory task

We next asked whether odor coding in the DG was related to the discrimination of odors when used as cues for contextual recall. In DG-dependent contextual fear discrimination/generalization experiments, a main cue used to distinguish contexts is the ambient odor cue present in each context (Danielson et al., 2016; McHugh et al., 2007; Sahay et al., 2011). We thus asked whether the accuracy of odor classification in the DG was related to use of these cues for contextual recall. To test this, we developed an odor-guided contextual fear memory task where mice discriminated contexts that differed in the ambient odor present. We used two chemically similar odorants, ethyl butyrate (EB) and methyl butyrate (MB), and one distinct odorant, isoamyl acetate (IAA)) . On day 1, mice explored the three contexts in order to assess baseline levels of freezing. The next day, mice received mild footshocks in a novel context (context d) infused with the MB odor from context b, and finally on day 3 were re-exposed to the three pre-training contexts and tested for freezing in three contexts (Figure 4A). Compared to control mice, LEC-DG TeLC mice showed lower levels of freezing in the context infused with the odor present during conditioning, and did not differ in freezing levels across contexts (**Figure 2.4A**). This suggests that LEC-DG TeLC mice did not use the odor as a cue for memory recall of the conditioned context. This was consistent with a role for the DG in context encoding and for the LEC in integrating contextual representations with non-spatial stimulus representations (Basu et al., 2016; Danielson et al.,

2016; Hargreaves et al., 2005; Kheirbek et al., 2013; Knierim et al., 2014; McHugh et al., 2007; Wilson et al., 2013).

As the odor present was likely the primary cue that elicited recall of the conditioning context, we asked if odor decoding accuracy in DG or LEC was related to contextual discrimination post-conditioning. For this, we ran mice in same protocol, except that we imaged odor responses before (Pre) and after (Post) conditioning with the footshock. Analysis of context discrimination scores after conditioning revealed considerable individual variability in discrimination of contexts a and b post conditioning (but not b/c, see **Figure S2.3B**), due to the chemical similarity of the EB and MB odorants, as some mice generalized their fear across contexts, while others discriminated (**Figure 2.4C-E and S2.3B**), similar to that seen in auditory fear discrimination (Likhtik et al., 2014). We thus asked whether behavioral discrimination was correlated with odor classification in the DG and LEC. We computed pairwise context discrimination scores on day 3 (see Methods) to compare to odor decoding accuracy scores. In DG GC recordings, odor decoding accuracy for the similar a/b pair (EB/MB) of odorants before conditioning correlated with context a/b discrimination scores after conditioning, as the mice with lower decoding accuracy scores before conditioning generalized their freezing responses, and the mice with the highest neural decoding scores went on to become the best behavioral discriminators (**Figures 2.4D**). A similar relationship between neuronal and behavioral discrimination was found when analyzing decoding scores after conditioning, or when using similarity of population vectors as a neural readout of discrimination (**Figures S2.3F,K**). This relationship was only found for the similar a/b (EB/MB)

odor pair, in which mice showed individual differences in the level of freezing in the contexts in which these odors were present, as mice were significantly better as a group at behaviorally discriminating the contexts where the distinct odors a/c (EB/IAA) were present (**Figure S2.3B,H-I**). This relationship between odor decoding accuracy and contextual discrimination was not seen in mice where recordings were taken from LEC neurons. While LEC mice showed similar individual variability in the ability to behaviorally discriminate the a/b contexts (**Figure 2.4E, S2.3B**), this did not correlate with neural decoding accuracy scores from LEC before conditioning (**Figure 2.4F**). These results show for the first time that the neural discrimination of odor cues in the DG, but not LEC, is correlated with the use of these cues to drive to drive discrimination between contexts.

Changes in odor representations in DG and LEC with reward learning

Next, we asked how odor representations in DG GCs and LEC change during associative reward learning. We trained mice in an appetitive conditioning task using the same 3 odors that were used in our context fear discrimination experiment. Odors were delivered for 4s, then a sucrose reward was delivered after a 2s trace period after presentation of one of the odorants, (conditioned stimulus, CS+, odor b, **Figure 2.5A**). We assessed learning by measuring licking during the CS+/- odor/trace period (**Figures 2.5B-C, S2.4A**), and recorded calcium dynamics in DG GCs, LEC neurons and DG GCs with silenced input from LEC (LEC-DG TeLC mice, as in Figures 3 and 4). Unlike in fear conditioning, where aversive reinforcement is known to drive stimulus generalization (Fletcher and Wilson, 2002; Ghosh

and Chattarji, 2015; Likhtik et al., 2014; Pavesi et al., 2012; Resnik and Paz, 2015), mice did not generalize the odor a/b pair, as all mice discriminated by day 3 (**Figures 2.5B-C and S2.5A-B**). The same cells in LEC and DG were imaged before learning (Pre, day 1) and after odor learning (Post, day 3) (**Figures 2.5D-E, S2.4B**). First, we found that, before learning, both in DG and LEC, neurons that responded to one odor also tended to respond to another odorant. However, after learning, DG GCs but not LEC neurons, were less likely to respond to multiple odorants, reducing overlapping odor representations (**Figures 2.5F-G, S2.4C-D**). In LEC-DG TeLC mice, in this experiment, we did not find cells that reached the statistical significance cutoff for odor responsivity, again supporting the role of this input in olfactory coding in the DG. In addition to reducing overlap, we found an increase in the proportion of DG GCs that were active during CS+ odor, and a decrease in the number active during the CS- (odor a) (**Figure 2.5H, S2.4E**). This again was not observed in LEC neurons (**Figure 2.5I**). In LEC-DG TeLC mice an increase in proportion of active cells was seen indiscriminately during both CS+ and CS- odors (**Figures 2.5J**). In line with our results in the DG and LEC, by limiting our analysis to those cells that responded to each odor on day 1 (Pre), we found that, CS- responsive DG GCs were more likely than LEC neurons to switch their response to the CS+ odor after learning (**Fig 2.5K**). Analysis of populations of DG GCs and LEC neurons, we found that with learning, odor representations became sparser in the DG, but not LEC (**Figure 2.5L**). In addition, odor classification performance prominently increased in the DG, with a more modest increase in LEC (**Figure 2.5M**). This again was not seen in LEC-DG TeLC mice, as while these mice could learn this simple association (**Figure S2.4B**), odor decoding

accuracy in the DG was poor both before and after learning (**Figure 2.5M**). Finally, a cross-session decoder performed significantly worse in DG than in LEC (**Figure 2.5N**), indicating that the geometry of the population code for odor stimuli in the DG dynamically changes with associative learning. These differential changes in DG and LEC during learning were not due to differences in signal-to-noise in recordings, or differences in lick related, breathing-related, or reward-related activity between the DG and LEC (**Figure S2.4I-L**). In addition, increasing the numbers of CS+ and CS- odors generated a similar pattern of results in DG GC recordings, as odor decoding accuracy increased with learning (**Figure S2.4H**). Finally, we recorded DG GCs during extinction session, where reward was not delivered, and found that odor decoding accuracy was reduced as compared to the post learning session, raising the intriguing possibility that learning generates new, odor-reward, representations in the DG (**Figure S2.4H**). Taken together, these results suggest that during associative learning LEC provides relatively stable odor representations to DG, where these representations change or generate new odor-reward representations to amplify the contrast between a CS+ odorant and a CS- odorant.

Discussion

Here, we have used measures of olfactory coding to show how the DG transforms external sensory stimuli into internal neural representations. We demonstrate that DG GCs effectively encode odor stimulus identities, and this process is correlated with future contextual discrimination. We find that inhibition of input from the LEC impairs odor coding in

DG GCs, and the use of odor cues to guide contextual recall. By recording in both DG and LEC, we find that odor identity could be more accurately classified from DG GCs than from LEC neurons. In addition, we found that during olfactory learning, odor representations were more flexible in DG than in LEC. Odor representations dynamically changed in DG with odor learning inducing an increase in the proportion of cells responding to the CS+ odorant and a decrease in those responding to the CS- odorant. This process of expanding the distance in representations with learning may serve as a substrate for memory formation within the DG and downstream HPC regions.

These findings expand upon recent work describing odor representations in upstream areas, such as piriform cortex and olfactory bulb (Bolding and Franks, 2017, 2018; Franks et al., 2011; Iurilli and Datta, 2017; Sosulski et al., 2011; Stettler and Axel, 2009) and studies reporting non-spatial representations in downstream CA1 (Aronov et al., 2017b; Hargreaves et al., 2005; Igarashi et al., 2014; McKenzie et al., 2016). Our studies support the hypothesis that every stage of processing along the OB to HPC stream applies some degree of pattern separation to decorrelate odor representations. We find that across odor correlations in DG and LEC are very low, and in some trials, correlations are less than zero, indicating that the LEC-DG circuit strongly separates different odor representations, to a greater degree than previously found in OB and piriform cortex (Choi et al., 2011; Roland et al., 2017; Schaffer et al., 2018). In addition, we report key differences between odor representations in the DG and those in its primary input region, LEC. While previous studies in anesthetized mice showed odor-evoked responses in LEC neurons (Leitner et al., 2016), it remained unclear how these

responses differ from DG, and how they changed with learning. By recording activity in both LEC and DG using a tightly controlled odor-based experimental paradigm, we observed that odor decoding accuracy was better in DG GCs when compared to LEC neurons, which is in line with previous studies proposing a role of DG GCs for an expansion of dimensionality through sparsity (Rolls et al., 1998). However, we also found that a model of LEC-DG based on random projections alone was not sufficient to obtain comparable levels of decoding as true DG data. Exploration of other models with random projections that introduce additional non-linearities, or ones that incorporate a rich heterogeneity of cell types and plasticity functions (Litwin-Kumar et al., 2017) may more accurately model the expansion of dimensionality and facilitation of associative learning we observe in the DG.

Using an odor-guided contextual fear memory task, we found that in DG, but not LEC, odor decoding accuracy scores correlated with individual animals' discrimination between contexts that differed in the presented odorant. Mice with the highest odor classification accuracies showed the best discrimination during context recall. In this task, mice use the odor cue for pattern completion; rapid recall of a full contextual representation from the partial cue. Recent studies have highlighted the role of mature DG GCs in pattern completion-mediated contextual recall (Nakashiba et al., 2012), and our work suggests that LEC-DG input facilitates the use of olfactory information in this process. We found that silencing LEC-DG transmission with TeLC impaired use of the odor cues in a different context to recall the conditioning context, in line with a role for the LEC recognizing non-spatial stimuli that have been experienced in a specific context (Wilson et al., 2013). While the mechanism

for this remains unclear, it may be the case that odor information is separated at the level of the DG and can drive distinct recurrent networks in CA3 to facilitate recall (McNaughton and Morris, 1987; Nakazawa et al., 2002). Thus, in a situation where odors are better separated in the DG, conditioning can drive a distinct CA3 recurrent network state that supports high fidelity recall and thus effective context discrimination (O'reilly and McClelland, 1994; Treves and Rolls, 1994). This may explain why odor decoding accuracies in LEC did not correlate with behavioral discrimination, as the added level of separation provided by the DG may be required for fine-tuning CA3 networks. However, future population level imaging studies in CA3 and in LEC-DG projection neurons in use odor-guided contextual memory tasks that vary the balance between pattern completion and separation will lend further insight into this process. Silencing LEC-DG transmission, while impairing learning-induced changes in population activity in the DG, did not worsen odor-reward learning, in the multi-trial, headfixed task used here. This would indicate that either the chronic nature of our silencing leads to compensation by other circuits, or that other brain areas are sufficient to perform this kind of associative learning task (Abraham et al., 2012; Boisselier et al., 2014; Gschwend et al., 2015; Han et al., 2018; Igarashi et al., 2014; Komiyama et al., 2010; Lepousez and Lledo, 2013; Li et al., 2018, 2017; Liu et al., 2014; Otazu et al., 2015; Zhu et al., 2018). Use of more temporally precise silencing methods, or more complex behavioral designs, may provide new evidence for the role of LEC-DG in pure odor-reward associations.

We found that CS+ specific changes that occur in DG during associative learning are less prominent in LEC. The strengthening we observe in neural representations through

learning may serve as a substrate for memory formation within the DG and downstream HPC regions. This phenomenon appears as an experience-dependent reduction of dimensionality in DG since the CS+ odor becomes over represented at the expense of the CS- odor and odor representations become minimally overlapping, i.e., orthogonal. We didn't observe similar changes in LEC, in line with other studies that describe cortical activities as a high dimensional computational substrate that is useful to flexibly learn new tasks (Fusi et al., 2016; Rigotti et al., 2013). An alternative interpretation may be that, with learning, the DG may generate new odor-reward representations. Studies aimed and manipulating CS-US contingencies and recording LEC and DG population responses will shed light on these different scenarios. Taken together, our experiments have potentially identified a location in a cortex-to-HPC circuit where information is transformed into a format that is potentially behaviorally relevant to the animal. The odor code in the DG becomes more explicit, i.e., by orthogonalizing odor representations, perhaps to allow for easier recall by downstream areas, such as CA3 and CA1, to guide behavior. This may be via plasticity mechanisms at perforant path synapses, neuromodulatory effects on the excitability of DG GCs, or enhancement of local microcircuit function (such as recruitment of adult generated GCs or local inhibitory/excitatory circuits) to optimize sparsity levels for classification (Drew et al., 2016; Luna et al., 2019). Experiments identifying how any or all of these processes facilitate learning will provide new insight into the ways in which the DG actively classifies odor representation as a consequence of appetitive conditioning. Identification of this process of separating

cortical representations of sensory stimuli with learning may represent a novel population-level substrate for associative learning.

Recent work has shown that place cell responses within GCs are stable over days, and do not remap in response to global contextual changes (Hainmueller and Bartos, 2018). Thus, while overall spatial maps in the DG remain stable over time, representations of discrete elements of the environment, such as the odorant cues used here, may change with learning providing downstream areas updated information on the saliency of non-spatial stimuli in the environment. This may reflect differences in the response properties of DG GCs to complex spatial contexts as opposed to specific discrete cues, which may arise from the distinct input pathways to the DG that are activated by spatial vs. non-spatial information, with spatially tuned DG GCs relying on medial entorhinal inputs and odor-responsive GCs relying on LEC inputs (Hafting et al., 2005; Hargreaves et al., 2005). In addition, recent work indicates that newly integrated GCs preferentially receive LEC inputs (Vivar et al., 2012; Woods et al., 2018), and this LEC-DG input was recently shown to directly increase the inhibition of mature GCs via adult-born GC activity (Luna et al., 2019), effectively enhancing the sparsity of activation in the DG. Thus, discrete stimuli that recruit LEC over MEC activity may distinctly modulate the activity of downstream mature GCs, or selectively drive the highly plastic population of newly-integrated GCs (Schmidt-Hieber et al., 2004).

Our findings offer insight to the population level and single cell encoding properties of the healthy DG, and future studies can leverage these tools to understand how the DG becomes dysfunctional in diseases such as Alzheimer's disease. The earliest aggregation of

amyloid-beta plaques in Alzheimer's disease occurs specifically in lateral entorhinal cortex, and hypometabolic-associated cognitive impairment has been localized to the LEC-DG circuit in mouse models and human subjects (Braak and Braak, 1991; Khan et al., 2014). As the loss of sense of smell has been identified as a potent risk factor for development of Alzheimer's disease, (Conti et al., 2013; Lafaille-Magnan et al., 2017; Morgan et al., 1995; Vassilaki et al., 2017) it will be of interest to explore how LEC-DG olfactory coding circuits are impacted in early stages of disease progression in mouse models. Taken together, our results suggest that olfactory coding may represent a novel proxy to study memory formation in the hippocampus in health and in disease.

Methods

Mice

All procedures were conducted in accordance with the U.S. NIH Guide for the Care and Use of Laboratory Animals and the institutional Animal Care and Use Committees at UCSF. Adult male C57BL/6J mice were supplied by Jackson Laboratory and were used beginning at 8-12 weeks of age. Mice were co-housed with litter mates (2-5 per cage). Mice were maintained with unrestricted access to food and water on a 12-hour light/dark cycle and experiments were conducted during the dark cycle portion.

Viral Constructs

For calcium imaging, AAVdj-CaMKII-GCaMP6f-WPRE-SV40 was packaged and supplied by Stanford Viral Vector Core at titer of 2.05 X 10^13 vg/ml. For tetanus toxin experiments, AAV-EF1a-DIO-TeLC-mCherry and AAV-EF1a-DIO-mCherry plasmids (Boehringer et al., 2017) were generously provided by Dr. Thomas McHugh (RIKEN) and packaged into AAVdj at Stanford Vector Core at a titer of 1.92 X 10^12 vg/ml and 6.34 x 10^12 vg/ml, respectively. AAV2retro-CAG-Cre was packaged and supplied by UNC Vector Core and injected at a titer of 2.8 x 10^12 vg/ml.

Surgery

Animals were 8-12 weeks of age at time of initial viral injection surgery. Mice were anesthetized with 1.5% isoflurane with an oxygen flow rate of ~1 L / min, and head-fixed in a stereotactic frame (David Kopf, Tujunga, CA). Eyes were lubricated with an ophthalmic ointment, and body temperature was maintained at 34-37°C with a warm water re-circulator (Stryker, Kalamazoo, MI). Fur was shaved and incision site sterilized with isopropyl alcohol three times and betadine solution three times prior to beginning surgical procedures. Lidocaine HCl 2% solution was injected subcutaneously local to incision, and post-surgical analgesia was provided by meloxicam and slow-release buprenorphine. For calcium imaging experiments, viral injections preceded lens implantation by 2-3 weeks to allow viral expression. For stereotactic viral injections, a craniotomy was made at injection site with a round 0.5 mm drill bit (David Kopf, Tujunga, CA). A nanoject syringe (Drummond Scientific,

Broomall, PA) was used with a pulled glass pipette (tip width 20-30 microns) to inject a total of 483 nl of AAVdj-CaMKII-GCaMP6f-WPRE-SV40 into the dorsal dentate gyrus at coordinates of AP -2.15, ML +/-1.25, DV -2.3, -2.15, -2.05, all relative to bregma (Paxinos and Franklin's, 4th edition). At each dorsal-ventral site of the dentate gyrus, 5 x 32.2nl pulses were delivered separated by 10 seconds. The needle was held in place for 5 minutes prior to moving to the next D/V coordinate, and remained in place for 10 minutes following the final injection before being slowly withdrawn from the brain. For injections into lateral entorhinal cortex, the following coordinates were used: AP -3.6, ML +/-4.4 (AP and ML coordinates from bregma), DV -2.6 (from medial brain surface at craniotomy site).

We modified a previously published procedure for imaging DG GCs, which has been shown to preserve DG structure, activity and DG-dependent behaviors (Danielson et al., 2016). Lens implantation surgery occurred 2-3 weeks following GCaMP6f virus injection. 30 minutes prior to anesthesia, dexamethasone was injected subcutaneously (0.2mg/kg dissolved in sterile saline). The animal was prepared on the stereotax as mentioned above. After making a longitudinal midline incision exposing the upper extent of the cranium, a no. 15 scalpel blade was used to scrape periosteum from the skull surface, as well as most superficial (~0.5mm) of posterior neck muscles attaching to the dorsal portion of the caudal skull surface. The skull surface was wiped with hydrogen peroxide for 15 seconds to further remove residual periosteum, then rinsed 3x with saline. Finally, the skull was lightly scored with a scalpel blade in a cross-hatched pattern to increase surface area contact for dental acrylic. A craniotomy approximating 1.1 mm in diameter was drilled by hand with a rounded

drill bit centered on the same AP (-2.15) and ML (-1.25) coordinates as the GCaMP injection for DG. For LEC, the craniotomy was made at AP (-3.6) and ML (-4.4). Dura was removed with a fish-hooked 27 gauge needle, and a 30 gauge blunt end needle was used to aspirate neural tissue superficial of the dentate gyrus or lateral entorhinal cortex. For DG surgeries, the hippocampal fissure surface was used to determine proper aspiration depth. For LEC implantation, 1mm of cortex was aspirated above implant location, estimated by marked depth on aspiration needle. The cranial cavity was filled with saline and collagen hemostat (Avitene) for 10 mins or until bleeding ceased when collagen plug was removed. The cavity was re-filled with saline, and a 1mm wide x 4.1mm long ProView GRIN lens (GLP-1042, Inscopix, Palo Alto, CA) was stereotactically implanted (AP -2.15, ML -1.25, DV -1.95) above the dentate gyrus,or LEC (AP -3.6, ML -4.4, DV -2 from skull surface at craniotomy). A miniaturized microscope (Inscopix) was used for visual guidance and fluorescence monitoring, and once placed, the lens was fixed to the skull with Metabond adhesive cement (Parkell, Edgewood, NY). The lens was lowered with an electronically controlled stereotax arm attachment (Scientifica, Uckfield, UK), and lowered at a rate of 0.2 mm per min until target depth was reached. Final depth was adjusted within 0.1 mm of target depth based upon maximizing the quality of the visualized fluorescence signal. Animals without fluorescence visible thru the miniscope were not used and lenses were retrieved. A custom-made titanium headbar was then attached to the skull using dental cement (Dentsply Sinora, Philadelphia, PA). Finally, a protective cap over the lens was applied with Kwik-Sil silicone elastomer (World Precision Instruments, Sarasota, Fl), which was removed and re-applied for each imaging

session. Mice were allowed to recover from lens implant surgery for at least 2 weeks prior to imaging experiments.

Post-mortem verification of imaging sites and histological analysis

DG and LEC imaging sites were verified in each animal included in final analysis (Figure S1). After imaging, mice were perfused transcardially with PBS followed by 4% PFA (both ~20 ml at a rate of 7-8ml per min). Entire mouse heads were placed in 4% PFA solution for 2-3 days to allow ample fixation of the area around the lens, allowing for dissection with the lens indent intact. Serial coronal sections (50 microns) around the lens site were collected and visualized and cross-registered with a mouse brain atlas.

For LEC-DG TeLC silencing experiments, animals were perfused as noted above, and a 1-in-6 series of coronal sections (50 microns) were collected. TeLC-mCherry expressing cell counts in the lateral entorhinal cortex were assessed for each mouse by identifying the section nearest to the targeted stereotactic injection (AP -3.6) site based on cross-registering with the Allen Brain Atlas, then counting the mCherry positive cells within the lateral entorhinal cortex to establish a total cell count for each animal, normalized by tissue area. An average count per mouse is provided and each mouse was verified for mCherry expression delimited to LEC cells projecting to DG (and not CA1) by visualizing mCherry positive terminals within the outer molecular layer of the dentate gyrus (Figure S1).

Odor-guided contextual fear memory task

Mice were run through a three day odor-guided contextual fear memory paradigm, where on day 1 mice were exposed to 3 contexts (Pre-conditioning), day 2 were conditioned in a different context (Conditioning), and day 3 tested in the same 3 contexts as day 1 (Post-conditioning). In imaging experiments, on Pre-conditioning and Post-conditioning days, mice were exposed to the contexts in the AM, then imaged with 2-photon microscopy in the PM (three hours after last context exposure). On day 1 and 3 (Pre-conditioning and Post-conditioning), mice were placed in a standard fear conditioning box (MedAssociates, Fairfax VT) with the following contextual cues: acrylic floor and rounded walls, floor with alpha-dry bedding, lights off, fan off, and ambient white noise at 60 decibels. Each pre-conditioning and post-conditioning context differed in the presence of the odors, one of 3 odors was present below the grid floor (odor a: ethyl butyrate, odor b: methyl butyrate, odor c: isoamyl acetate). Odors were applied directly to a clean cotton tip applicator for a few seconds until saturated, and placed under grating 1-2 minutes prior to an animals' entry into the conditioning box. One hour separated each context exposure, and odorant was cleared from room with a charcoal vacuum filter, and order of exposure was randomized among mice. For pre and post conditioning, mice were allowed to explore the context for 5 mins before removal, and percent freezing was evaluated. On conditioning day, the mice were placed in the fear conditioning boxes with odor b (methyl butyrate) present, and the following contextual cues: (conditioning context (context d): bare metal grating floor, squared walls, lights on, fan on, room lights on). Mice were allowed to explore the context for 3 minutes prior

to receiving three footshocks 60s apart (2s, 0.7mA). After the final shock, mice were immediately removed from the shock box. Behavioral freezing data was collected and analyzed using FreezeFrame video software (Actimetrics) with a freezing epoch threshold of 1 second, and automatic movement signal detection. Freezing percentages represent the entire 5 minutes of re-exposure and were performed with the experimenter blind to odor or experimental group. Context discrimination index for any context pair was calculated as (percent time freezing to context 1- percent time freezing to context 2)/(percent time freezing to context 1+ percent time freezing to context 2).

Head-fixed odor delivery

Animals were handled and habituated to the experimenter, training environment and head-fixation setup for 30 mins a day for at least two days before imaging experiments were ran. On imaging days, monomolecular odors were delivered through a custom built 6 channel olfactometer equipped with a mass flow controller (Alicat Scientific, Tucson, AZ) that monitored and maintained air flow at 2 liters per min and prevented momentary pressure changes from solenoid valve switches upstream of the controller. The olfactometer solenoids were triggered by an Arduino Mega with custom circuit boards (OpenMaze.org), and stimulus delivery recorded via CoolTerm software. One side of the nose cone had a tubing insert that delivered odors, the other side containing an outlet in which a gentle vacuum was applied to evacuate residual odor. Additionally, an ongoing charcoal filter vacuum system (Hydrobuilders Inc.) was placed in the 2P isolation box to evacuate odors that leaked out of the nosecone

apparatus. For all experiments, mice were habituated to the 2p head fixed setup for 10 mins prior to imaging, and imaged for 30s at baseline before a structured trial of odors were delivered for 4 seconds with a 16 second ITI, presented in pseudo-randomized fashion. For 6 odor experiments, 20 trials were performed for each odor for a total continuous imaging session of ~30 mins. For 3 odor experiments, 30 presentations of each odor were performed in a session (~30 mins). Several different odor panels were run on cohorts of imaged animals. For a 6 neutral odor panel (Figures 1-3), we used: benzaldehyde (BA), eugenol (EU) , heptanal (HEP), hexanal (HEX), alpha-pinene (PIN), and eucalyptol (EUC). For a 3 odor panel testing odor discrimination and learning (Figures 4-5) we used methyl butyrate (MB) ethyl butyrate (EB) and isoamyl acetate (IAA). For mixed tone/odor experiments (Supplementary Figure 1), mice were given 3 tones at 4, 9 and 10Khz, 4s each with 16s ITI presented in a pseudorandom order, 30 presentations each, identical in trial design to the 3 odor experiment. Following tone trials (in the same session), the same FOV was recorded for 3 odor responses as above (EB, MB, IAA) so that we could directly compare overlapping tone/odor responses within the same population of neurons. For 4 odor associative learning experiments, we used: limonene, benzaldehyde, eugenol, and isoamyl acetate. For all associative or fear learning experiments, separate cohorts of mice were used.

2-photon imaging

2-photon imaging of the DG was performed using an Ultima IV laser scanning microscope (Bruker Nano, Middleton, WI) equipped with an 8Khz resonance galvanometer

and high speed optics set, dual GaAsP PMTs (Hamamatsu model 7422PA-40), and motorized z focus (100nm step size). Approximately 30-90 mW of laser power (at 920nm, from MaiTai DeepSee mode-locked Ti:Sapphire laser source (Spectra-Physics, Irvine, CA)) was used during imaging, with adjustments in power levels to accommodate varying window clarity. Once a given power level was established for an animal, identical power was used across experiments to increase reliability in fluorescence detection across sessions. To optimize light transmission, we adjusted the angle of the mouse's head using two goniometers in the anterior-posterior and medial-lateral axis (Edmund Optics, +/-10 degree range) such that the GRIN lens was parallel to the objective. After focusing on the lens surface, optical viewing was switched to live view thru the 2-photon laser, and an FOV was located by moving the objective between ~50-300 microns upwards. FOVs were chosen in the GCL, avoiding those FOVs where hilus was visible as previously shown (Danielson et al 2016). Once an FOV was set for a given animal, each imaging session was manually aligned to approximate the same FOV across sessions. All images were acquired with a Nikon 20X NIR long working distance objective (0.45 NA, 8.3 mm WD). GCaMP6f signal was filtered through an ET-GFP (FITC/CY2) filter set. Acquisition speed was 30Hz for 512 x 512 pixel images. Images were averaged online for every 8 frames, yielding a final acquisition rate of 3.7 frames per second.

Appetitive Odor Conditioning

For the appetitive odor conditioning task, water-deprived mice were first habituated to the 2P setup with lick spout. Mice were given 50ul 10% sucrose by volume reward 100x

(reward following regular intervals every 15 trials) for 3 days, or until mice successfully licked for reward <1,000 times in under 10 minutes of head-fixation. After mice exhibited sufficient lick training, water-deprived mice were imaged under pseudorandom presentation of a three neutral odor panel, EB, MB, IAA (see above), with a 2 second trace delay followed by 50ms reward delivery window following each MB (odor b, CS+) trial (in order to isolate odor responses distinct from reward delivery), simultaneously with 2-photon imaging, and a variable ITI of 12-16 seconds. Reward was delivered regardless of whether the animal licked during odor b (CS+, MB) trials, and no punishment or time outs were administered if mice licked during the CS- trials. Mice were run once a day for 3 days through this task. All mice used in this study showed highly accurate licking to the CS+ odor by the 3rd day as analyzed by lick rates to the odor/trace period. Respiration was monitored using a Honeywell Airflow Sensor (AWM3300V). In the 4 odor task, mice were run in the same manner as above, but with 2 odors acting as the CS+, and 2 odors as the CS-. Separate cohorts of mice were run in either the 3 odor or 4 odor associative learning experiment. As with the 3 odor associative learning task, a total of 30x odor trials were delivered in pseudorandom order with a 4s odor delivery period, 2s trace, and 50ms reward window for two CS+ odors, followed by variable ITI between 12-16s. The odorant identities of CS+ or CS- were randomly assigned for each mouse. Odorants used were: limonene, benzaldehyde, eugenol and isoamyl acetate. In this 4 odor associative learning task, mice were run for a 4th day of imaging, in which the lick spout was removed from the head-fixed setup to image mice in the absence of reward delivery.

Calcium data processing

Videos were motion corrected offline with the TurboReg registration plugin in FIJI. An average intensity z-projection of the first 100 stable frames (assessed manually) was used as a template with the translation model of motion correction. Cell segmentation and calcium transient time series data were extracted using Constrained Non-negative Matrix Factorization for microEndoscopic data (CNMF-E), a semi-automated algorithm optimized for GRIN lens Ca2+ imaging to denoise, deconvolve and demix calcium imaging data (Zhou et al., 2018). Briefly, this software uses a non-negative matrix factorization algorithm to extract the putative denoised calcium signals and spatial footprints. Putative neurons were identified, and sorted by visible inspection for appropriate spatial configuration and Ca2+ dynamics as described above, and putative units were manually merged or split from visual inspection. We ran the CNMF-e algorithm on each recording session separately to extract denoised calcium traces, inferred calcium events and spatial footprints. For all plots, we used the inferred calcium events for analysis unless otherwise specified.

Registration of cells across pre and post-conditioning sessions imaged at the same FOV was achieved using probabilistic modeling of similarities between cell pairs across sessions (Sheintuch et al., 2017). Briefly, spatial footprint maps were generated for each session by projecting the spatial filter of each cell onto a single image. Spatial footprint images from sessions imaged at the same FOV were then aligned. The distribution of similarities between pairs of neighboring cells were subsequently modeled via centroid distance to obtain an estimation for their probability of being the same cell (Psame). Cells

were then registered across pre and post sessions via a clustering procedure that utilizes the previously obtained probabilities, with a probability threshold of 0.8. The average Psame value for registered cells was 0.96.

Data analysis

Odor responsivity

We defined cells as responsive to an odor by comparing the calcium events identified within all presentations of that odor with the events identified in the baseline period of 4 seconds preceding odor presentations. We used a two-sided Mann-Whitney-U test to assess if the difference in activity levels were statistically significant (**$p<0.01$, *$p<0.05$ for all tests in manuscript, see Supplementary Table 1). Then, a cell was considered responsive if the FDR-adjusted p-value of the statistical test was lower than 0.05 for a given odor or combination of odors (i.e., responsive to more than one odor). For raster plots of odor responses, normalized Ca event magnitude was generated by dividing each event magnitude by the mean event magnitude across the session and average across trial.

In learning experiments where we computed the stability of odor responses across sessions, by pooling all cells across all the mice and identifying the same cells in the pre-(day 1) and post-conditioning (day 3) sessions through registration (see above). We considered cells that were responsive to one odor in the pre-conditioning session and their response profile in the post-conditioning session. We expressed the percentage of responsive cells in

the post-conditioning session with respect to the subgroup of cells considered in the pre-conditioning session.

We also determined whether activity of LEC or DG neurons were modulated by reward consumption or correlated with licking or breathing. For reward responsivity, we generated peristimulus time histograms of normalized Ca^{2+} activity (by dividing the event magnitude by the mean event magnitude across the session) centered at the first lick after reward availability. Activity was averaged across trials (10) and cells for each mouse, and averaged across mice. Lick rates were computed in each time bin and averaged across trials and across mice.

To look for a relationship between licking or breathing and neural activity, we regressed the lick rates or the breathing rates across the session against the calcium events. We fit a linear regression model to predict lick rates or breathing rates and used the explained variance (r^2) as a measure goodness of fit to compare the results across animals and days. We divided each analyzed session in 10 time-contiguous blocks and computed the generalization performance of the model with 10-fold cross-validation over these blocks to avoid overfitting. Regression was performed with regular linear regression with L2 norm or with Lasso, and verified that the results are not qualitatively different in either case (we report the more stringent case of Lasso in Figure S4).

Modulation index

For each odor presentation, we first extracted the raw calcium trace in a window between 5 seconds prior to the odor onset and 10 seconds after odor offset. We then divided all the traces by their standard deviation computed across all presentations of that odor as normalization. Finally, the modulation index was computed as:

$$\delta_f = \frac{r_s - r_b}{r_b} \times 100$$

where r_s is the mean calcium trace during odor presentation of a cell, averaged across trials, and r_b is the same quantity but computed on the 4 seconds preceding odor presentation.

Decoding

We used a linear decoder to discriminate patterns of activity into two discrete categories (Bishop, 2006):

$$y(t) = \theta(W\vec{r}(t) + b)$$

where y_i is the predicted label of the population activity pattern $\vec{r}$ recorded at time t and takes two values corresponding to the two classes of patterns to decode (for instance, the two odor identities), W is the vector of weights assigned to each cell and b is a constant bias term. Decoding parameters were obtained through a supervised learning protocol on labeled data using a support-vector machine (SVM) with a linear kernel (python/scikit/linearSVC). Data

is reported as the generalized performance of the decoder using cross-validation, a standard machine learning procedure to avoid data overfitting. When multiple categories were involved, i.e., more than two odors, multiple linear decoders were trained on pairs of discrete categories combined using majority-based error-correction codes.

For decoding odor identity, we used a linear decoder trained on the recorded population activities. For each odor presentation, we defined the patterns of calcium activity by computing the mean event rates during the 4 seconds of odor presentation. We then evaluated the ability of the decoder to predict the odor identity based on the calcium activity on 10-fold cross-validated data, unless specified otherwise. To determine differences in the ability of our decoder to discriminate between single odor pairs, we used only the trials corresponding to that odor pair and measured performance in this subset with cross validation. For reporting decoding performance for single animals, we compared to a distribution of chance decoding performances computed by training our decoder on data in which odor identities were randomly shuffled with respect to the population activity patterns (n=100 datapoints). When combining animals to compute average decoding performance of a group, we computed mean performance for each animal across different choices of training and test data (cross-validation) and performed a tests for significance from chance or between groups. When comparing decoding performance between neural populations of different size, we trained our decoder on a subsample of randomly chosen cells from the more numerous population equal to that of the smaller population. We repeated the operation 100 times and then combined the cross-validated decoding accuracies of all random choices

together to get a single sample of decoding accuracies. In conditions where we pooled cells across animals, we generated pseudo-population recordings by combining cells across multiple FOVs. For decoding odor identity from the pseudo-population, we divided the dataset in two. Then, from one of the two halves, we generated odor patterns of each odor by choosing the activation level of every neuron independently from a random trial, within that half, corresponding to that odor. We then generated test data in the same way but from the remaining half of the data to evaluate the decoder's generalization performance. We repeated the procedure to generate pseudo-population and cells subsampling 1000 times to perform statistical comparisons across groups and against chance decoding performance.

To decode odor identity around stimulus onset, we first averaged the event rates in 1 second long time bins between 3 seconds before odor presentation onset and 6 seconds after offset. We then trained a separate decoder for each time bin separately and assessed its performance on 5-fold cross-validated data.

For the DG model, we determined whether a model based upon random connectivity could generate the observed increase decoding performance in DG with respect to LEC. We first generated pseudopopulation data as explained above. We calibrated the sparsity in the model, i.e., the fraction of cells with a larger than zero calcium activity for any pattern, based on the training half of the pseudo-simultaneous population data Then we equalized the number of cells across different groups to compare decoder performances by subsampling at random from the population of cells in a number equal to the minimum number of cells available across groups. We repeated the procedure to generate pseudo-population and cells

subsampling 1000 times to perform statistical comparisons.

In the model, each LEC cell is connected through a synaptic matrix W to a fixed number of DG cells ($n = 10$) (Abusaad et al., 1999) with weights drawn from a gaussian distribution of zero mean and unitary variance. DG cells are modeled as threshold-linear units, therefore the activity pattern in DG in the model $\vec{r}_{DG}$ is obtained from the activity pattern of LEC cells $\vec{r}_{LEC}$ as follows:

$$\vec{r}_{DG} = \theta\,(W\vec{r}_{LEC} - b)$$

where $\theta = 0$ is its argument is lower than zero and b is a threshold. The sparsity of activations in DG is regulated by the threshold b which is adjusted to match the sparsity levels across patterns of each odor in the DG data.

Ensemble similarity

To compute pattern similarities (McKenzie et al., 2016), we computed the mean event rates during each odor presentation in a session as well as the patterns during 4 seconds prior to odor onset as baseline. We then computed the mean cosine similarities (Pearson correlation) between every two pairs of patterns as:

$$s = \frac{1}{N}\sum_{i,j\neq i}^{N}\frac{\vec{r}_i\vec{r}_j}{|\vec{r}_i||\vec{r}_j|}$$

where $\vec{r}_i$ and $\vec{r}_j$ are the patterns of population activities for trial i and j and N is the total number of pairs of patterns. The similarity values where then pooled to verify for statistical

differences across categories of stimuli, for instance patterns of same odors versus patterns different odors, or patterns from the same session versus patterns from different sessions.

Overlaps

In order to compute overlapping responses, we determined the number of cells that showed statistically significant responses to two odors (or 3 odors for 3 odor overlap) (See *Odor responsivity* above). To assess statistical significance, we pooled together cells from all mice in each region to generate pseudo-simultaneous recordings. To generate chance distributions, we randomly assigned odor responses to all cells for each of the two odors (or 3 odors for 3 odor overlap) with probabilities that matched the proportion of responsive cells for each odor as in the real data. We computed the overlap for each random assignment and repeated the procedure 10000 times to obtain a chance distribution. We finally assessed the statistical significance of the actual overlap between the two (or 3) odors by computing the probability of obtaining that value from the chance distribution assuming a normal distribution of estimated mean and variance.

Lifetime sparseness

We computed lifetime sparseness by:

$$S = \frac{1-A}{(1-\frac{1}{N})}$$

where N is number of odor stimuli and A is the activity fraction (Rolls and Tovee, 1995):

$$A = \frac{\left(\sum_i \frac{r_i}{N}\right)^2}{\sum_i \frac{r_i^2}{N}}$$

The activity fraction is computed on the average activity pattern r_i for each odor i (Vinje and Gallant, 2000):

$$r_i = \frac{1}{M} \sum_j r_i^j$$

where $j = 1, \ldots, M$ and M is the total number of trials.

Signal to noise (SNR)

We computed the Signal-to-Noise ratio by:

$$SNR = \frac{|S|^2}{|S - S_{raw}|^2}$$

Where S is the convolved calcium trace and S_{raw} is the raw calcium trace.

Figure 2.1: Odor responses in DG GCs

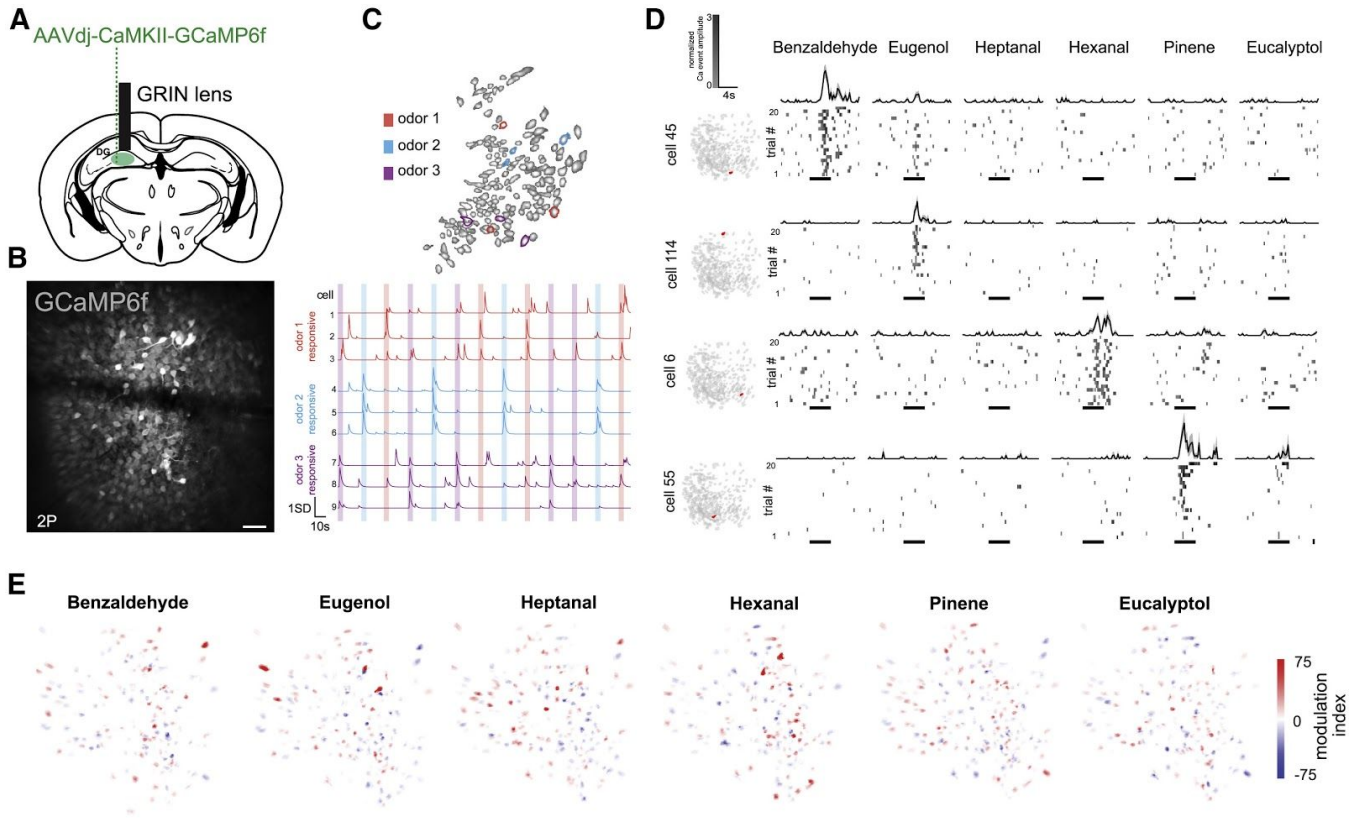

A. Experimental design. GCaMP6f is expressed in DG GCs for 2-photon microscopy imaging of odor responses in DG GCs in awake behaving mice. B. Standard-deviation projection of *in vivo* 2-photon image from a representative DG FOV. Scale bar 50 μm C. Odor-evoked neural responses in 9 example DG GCs, spatial footprints of identified ROIs on left, with denoised calcium traces on right (odor delivery periods indicated with shading). D. Normalized calcium events and cell maps from DG GC FOVs. Example cell responses during exposure to a six odor panel (20 trials). Normalized Ca event magnitude was generated by dividing each event magnitude by the mean event magnitude across the session and average across trial. 4s odor delivery times noted below raster, with average responses in above trace (mean (black) plus SEM (grey)). D. Odor responses are sparse and randomly distributed in the FOV. Spatial footprints shown from an example mouse, with overlaid modulation index for each cell (see Methods).

Figure 2.2: Odor responses in LEC

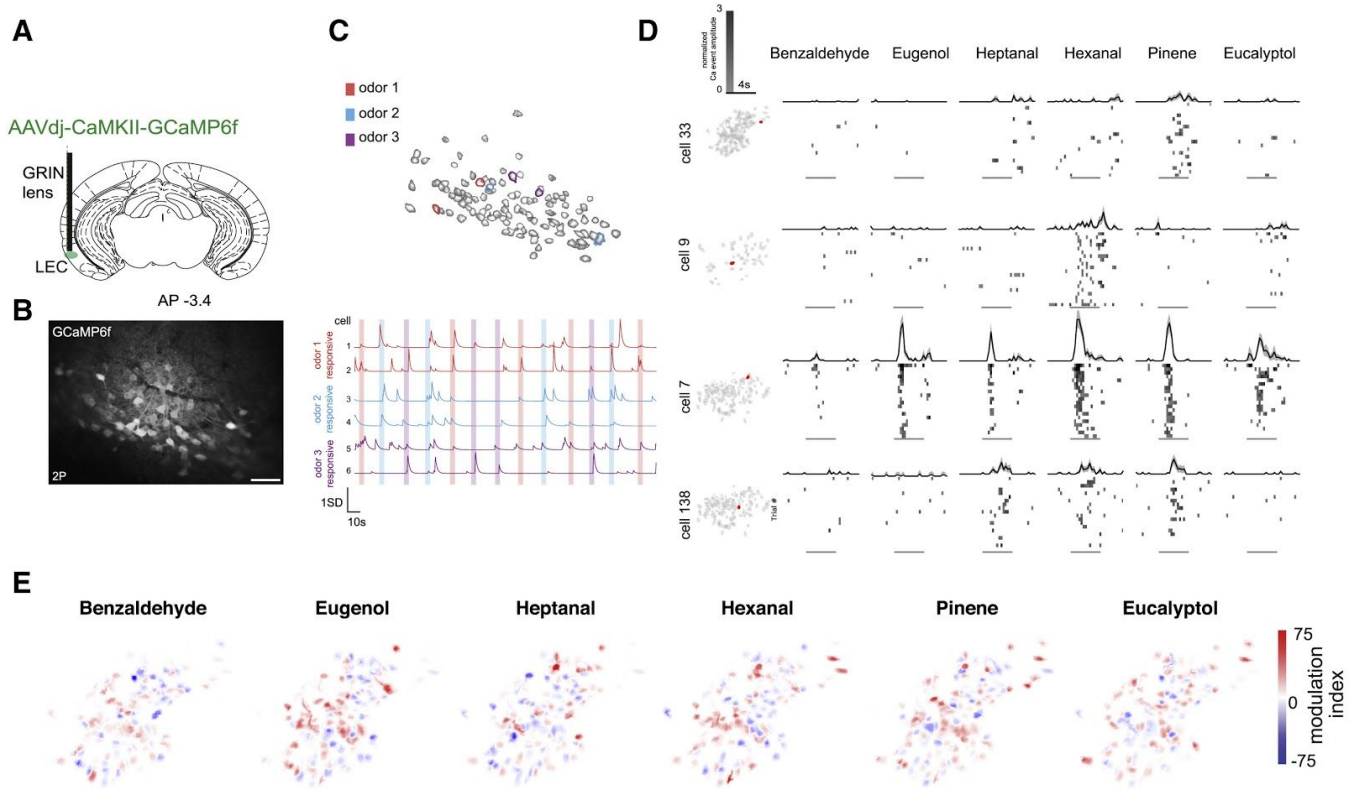

A. Experimental design. GCaMP6f is expressed in LEC neurons for 2-photon microscopy imaging of odor responses in awake behaving mice. B. Standard-deviation projection of *in vivo* 2-photon image from a representative LEC FOV. Scale bar 50 μm C. Odor-evoked neural responses in 9 example LEC neurons, spatial footprints of identified ROIs on left, with denoised calcium traces on right (odor delivery periods indicated with shading). D. Normalized calcium events and cell maps from LEC FOVs. Example cell responses during exposure to a six odor panel (20 trials). Normalized Ca event magnitude was generated by dividing each event magnitude by the mean event magnitude across the session and average across trial. 4s odor delivery times noted below raster, with average responses in above trace (mean (black) plus SEM (grey)). D. Odor responses are sparse and randomly distributed in the FOV. Spatial footprints shown from an example mouse, with overlaid modulation index for each cell (see Methods).

Figure 2.3: Neural representations of olfactory stimuli in DG, LEC and LEC-DG TeLC mice

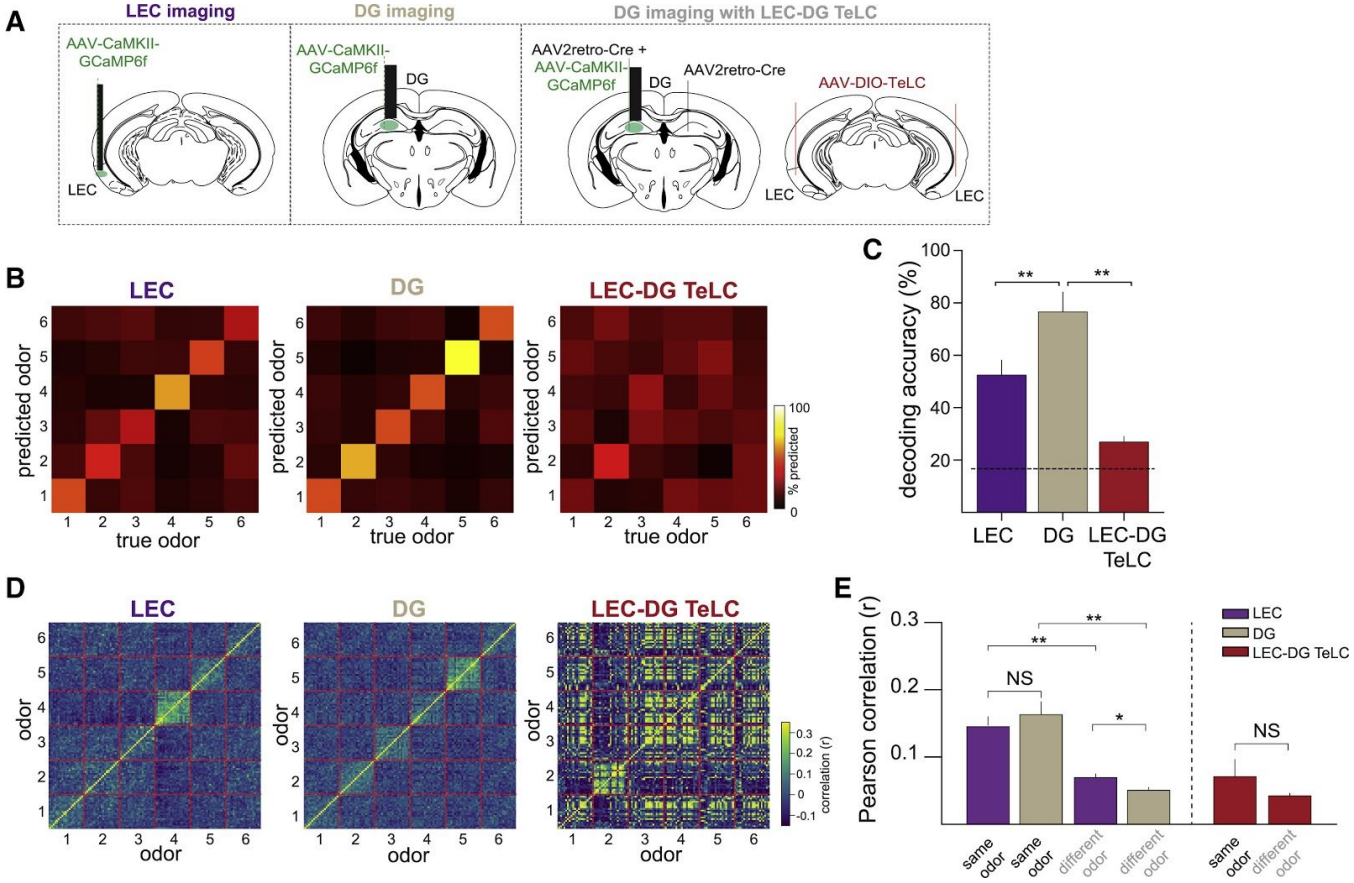

A. Experimental cohorts for imaging DG, LEC and the DG of LEC-DG TeLC mice (see Methods) B. Confusion matrix for decoding of 6 odors (1: benzaldehyde, 2: eugenol, 3: heptanal, 4: hexanal, 5: pinene, 6: eucalyptol) from LEC neurons, DG GCs, and DG GCs from LEC-DG TeLC mice C. Quantification of odor decoding accuracies. Odor decoding accuracy was significantly better in DG GCs than LEC neurons, and decoding accuracy was significantly reduced in LEC-DG TeLC DG GCs (linear SVM classifier with matched number of cells in DG, LEC, and LEC-DG TeLC mice n=189 cells (n-matched) from 8 DG, 7 LEC and 3 LEC-DG TeLC mice, Mann-Whitney U test, **p<0.01. D. Trial by trial similarity matrix for same 6 odors as in B (1: benzaldehyde, 2: eugenol, 3: heptanal, 4: hexanal, 5: pinene, 6: eucalyptol) from recordings of LEC neurons, DG GCs and DG GCs from LEC-DG TeLC mice. D. Quantification of Pearson correlation coefficients revealed lower across odor correlations in DG GCs as compared to LEC neurons. No significant difference was found between within and across odor correlations in DG GCs from LEC-DG TeLC mice n=8 DG, 7 LEC and 3 LEC-DG TeLC mice, t-test, *p<0.05, **p<0.01. Error bars represent +/- SEM. For exact *P* values, see Supplementary Table 1.

Figure 2.4: Odor classification in the DG but not LEC correlates with discrimination of odors for contextual recall

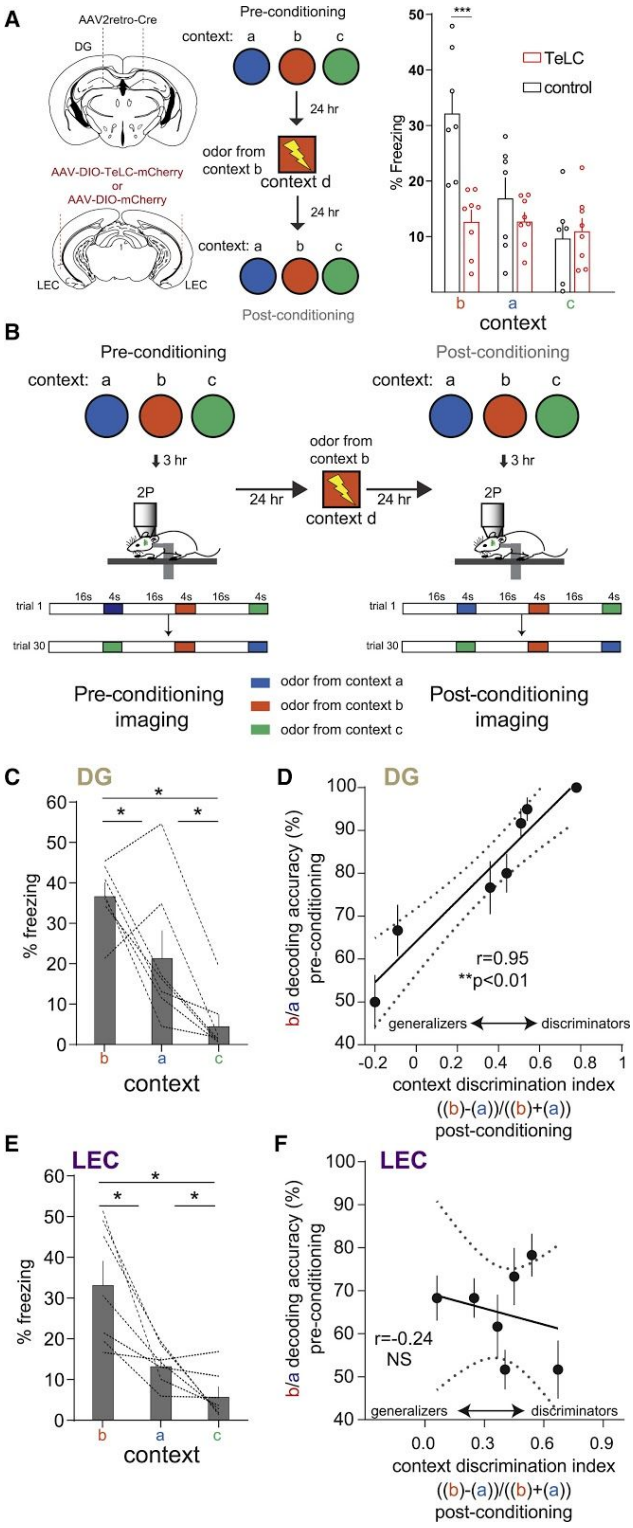

Figure 2.4 (continued) A. LEC-DG TeLC and control mice were pre-exposed to three contexts that differed in the infused odor (context a: ethyl butyrate, b: methyl butyrate, c: isoamyl acetate) to assess pre-conditioning freezing (see Supplementary Figure 2). The next day, mice were given foot shocks in a novel context infused with the odor from context b (methyl butyrate). Twenty four hours later, mice were re-exposed to contexts a-c, and freezing measured. *Right.* LEC-DG TeLC showed reduced freezing in the context infused with the odor from the conditioning context. (n=8 LEC-DG TeLC, 7 control, repeated measures ANOVA with post hoc t-test with Holm-Sidak correction **$p<0.01$) Error bars represent +/- SEM B. Experimental design for imaging. Design was identical as in A, except that mice were imaged on pre-conditioning and post-conditioning days. Error bars represent +/- SEM C. Percent freezing in the DG imaging mice three contexts post conditioning (n=7 DG mice,t-test with Holm-Sidak correction, * $p<0.05$) Error bars represent +/- SEM D. A context fear discrimination index (context a vs. context b) was calculated based on freezing scores for each animal and plotted against the decoding accuracy obtained from 2P imaging pre-conditioning (Pearson's correlation, $r=0.95$, n=7 mice, linear fit with solid line, 95% confidence interval in dashed lines, $p<0.001$. Error bars represent +/- SEM for 30 cross validations of the decoder (see Methods)). E. Percent freezing in the LEC imaging mice in the three contexts post conditioning (n=7 LEC mice t-test with Holm-Sidak correction, * $p<0.05$) . F. Context discrimination indices (context a vs. context b) plotted against the decoding accuracies obtained from LEC imaging pre-conditioning. Pearson's correlation, $r=-.24$, n=7 mice, linear fit with solid line, 95% confidence interval in dashed lines, $p=0.3$. Error bars represent +/- SEM for 30 cross validations of the decoder (see Methods)). For exact *P* values, see Supplementary Table 1.

Figure 2.5: Associative learning amplifies cortical representations of salient stimuli in DG GCs

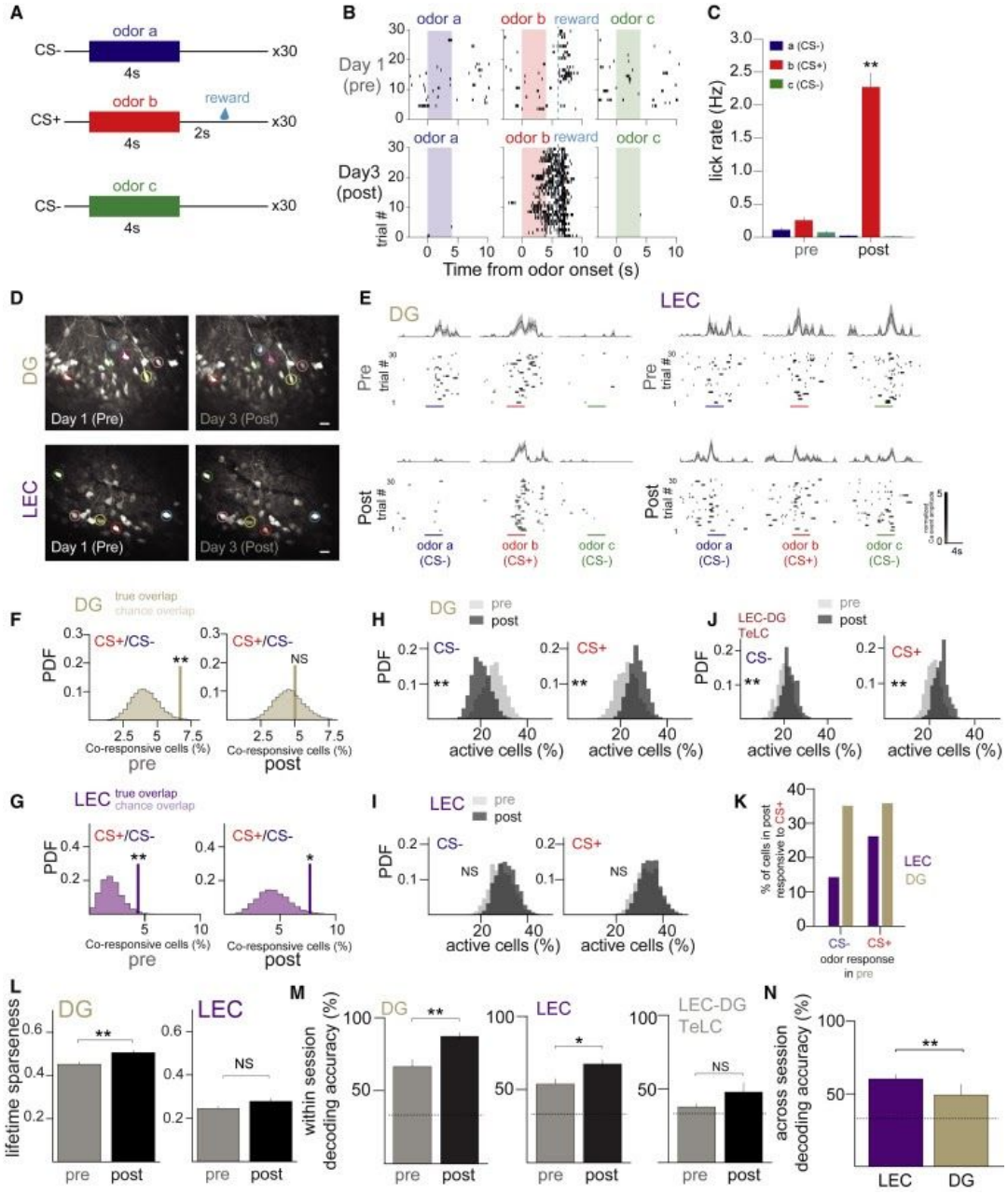

A. Experimental schematic for associative odor conditioning. A sucrose reward was delivered on CS+ trials. B. Lick rasters showing behavioral performance on day 1 (Pre) and day 3 (Post) of learning. C. Average lick rates during the odor and trace period on day 1 (Pre) and day 3 (Post) (Mann-Whitney U test, **p<0.01, n=3 DG mice). D. Cell registration across days in the same FOV. Circled cells are examples of registered neurons (see Methods and S5 for cell registration approach). E Example rasters and normalized activity for cross registered, odor responsive DG (left) and LEC (right) cells. F-G. In the DG (F) odor overlaps for CS+/CS- odors fall to levels comparable to the shuffled distribution after learning, but in LEC (G) neurons overlaps remain stable across learning (level of significance for 10,000 shufflings **p<0.01,

*p<0.05, n=359 DG cells, n=182 LEC cells). H-J. Comparison of proportion of active cells during odor presentation in pre and post (pseudo-simultaneous recordings across multiple FOVs, where each bin represents the proportion of odor trials in which we found a given percentage of active cells). Proportion active is significantly increased in the post session for the CS+ odor and decreased for the CS- odor in DG (H), but not in LEC (I), and increased to both CS+ and CS- odors in (J) LEC-DG TeLC mice (t-test, **p<0.01, n=3 DG mice, n=3 LEC mice, n=2 LEC-DG mice). K. Odor responses in Post for cross-session registered cells. Cells were classified as odor responsive in Pre, and then their responses were determined in Post. Compared to LEC neurons, odor a responsive DG GCs were more likely to become responsive to odor b (CS+ odor) after learning. (n=3 DG mice, 359 cells; n=3 LEC mice, 182 cells X2 test, p<0.01) L. Lifetime sparsity increases in DG but not LEC across learning (Mann-Whitney, p<0.01, n=3 DG mice, n=3 LEC mice). M. Odor decoding accuracy improved across learning in both DG and LEC, but not LEC-DG TeLC mice (Mann-Whitney, **p<0.01, *p<0.05, n=3 DG mice, n=3 LEC mice, 2 LEC-DG mice) N. Across-session odor decoding accuracy (training on Pre data and testing on Post data) was significantly higher in LEC compared to DG, indicating greater stability in representations within LEC across learning (n=3 pre group, Mann-Whitney, **p<0.01). Error bars represent +/- SEM. For exact *P* values, see Supplementary Table 1.

References for Chapter 2

Abusaad, I., MacKay, D., Zhao, J., Stanford, P., Collier, D.A., and Everall, I.P. (1999). Stereological estimation of the total number of neurons in the murine hippocampus using the optical disector. J. Comp. Neurol. *408*, 560–566.

Abraham, N.M., Guerin, D., Bhaukaurally, K., and Carleton, A. (2012). Similar odor discrimination behavior in head-restrained and freely moving mice. PLoS One *7*, e51789.

Abusaad, I., MacKay, D., Zhao, J., Stanford, P., Collier, D.A., and Everall, I.P. (1999). Stereological estimation of the total number of neurons in the murine hippocampus using the optical disector. J. Comp. Neurol. *408*, 560–566.

Aimone, J.B., Deng, W., and Gage, F.H. (2011). Resolving new memories: a critical look at the dentate gyrus, adult neurogenesis, and pattern separation. Neuron *70*, 589–596.

Aronov, D., Nevers, R., and Tank, D.W. (2017a). Mapping of a non-spatial dimension by the hippocampal–entorhinal circuit. Nature.

Aronov, D., Nevers, R., and Tank, D.W. (2017b). Mapping of a non-spatial dimension by the hippocampal–entorhinal circuit. Nature *543*, 719.

Basu, J., Zaremba, J.D., Cheung, S.K., Hitti, F.L., Zemelman, B.V., Losonczy, A., and Siegelbaum, S.A. (2016). Gating of hippocampal activity, plasticity, and memory by entorhinal cortex long-range inhibition. Science *351*, aaa5694.

Bathellier, B., Buhl, D.L., Accolla, R., and Carleton, A. (2008). Dynamic ensemble odor coding

in the mammalian olfactory bulb: sensory information at different timescales. Neuron *57*, 586–598.

Bishop, C. (2006). Pattern Recognition and Machine Learning (Springer-Verlag New York).

Boehringer, R., Polygalov, D., Huang, A.J.Y., Middleton, S.J., Robert, V., Wintzer, M.E., Piskorowski, R.A., Chevaleyre, V., and McHugh, T.J. (2017). Chronic Loss of CA2 Transmission Leads to Hippocampal Hyperexcitability. Neuron *94*, 642–655.e9.

Boisselier, L., Ferry, B., and Gervais, R. (2014). Involvement of the lateral entorhinal cortex for the formation of cross-modal olfactory-tactile associations in the rat. Hippocampus *24*, 877–891.

Bolding, K.A., and Franks, K.M. (2017). Complementary codes for odor identity and intensity in olfactory cortex. Elife *6*.

Bolding, K.A., and Franks, K.M. (2018). Recurrent cortical circuits implement concentration-invariant odor coding. Science *361*, eaat6904.

Braak, H., and Braak, E. (1991). Neuropathological stageing of Alzheimer-related changes. Acta Neuropathol. *82*, 239–259.

Broca, P. (1878). Anatomie compared des circonvolutions cerebrales. Le Grand Lobe.

Choi, G.B., Stettler, D.D., Kallman, B.R., Bhaskar, S.T., Fleischmann, A., and Axel, R. (2011). Driving opposing behaviors with ensembles of piriform neurons. Cell *146*, 1004–1015.

Conti, M.Z., Vicini-Chilovi, B., Riva, M., Zanetti, M., Liberini, P., Padovani, A., and Rozzini, L. (2013). Odor identification deficit predicts clinical conversion from mild cognitive impairment to dementia due to Alzheimer's disease. Arch. Clin. Neuropsychol. *28*, 391–399.

Danielson, N.B., Kaifosh, P., Zaremba, J.D., Lovett-Barron, M., Tsai, J., Denny, C.A., Balough, E.M., Goldberg, A.R., Drew, L.J., Hen, R., et al. (2016). Distinct Contribution of Adult-Born Hippocampal Granule Cells to Context Encoding. Neuron *90*, 101–112.

Drew, L.J., Kheirbek, M.A., Luna, V.M., Denny, C.A., Cloidt, M.A., Wu, M.V., Jain, S., Scharfman, H.E., and Hen, R. (2016). Activation of local inhibitory circuits in the dentate gyrus by adult-born neurons. Hippocampus *26*, 763–778.

Eichenbaum, H., and Otto, T. (1992). The Hippocampus and the Sense of Smell. In Chemical Signals in Vertebrates 6, R.L. Doty, and D. Müller-Schwarze, eds. (Boston, MA: Springer US), pp. 67–77.

Eichenbaum, H., Yonelinas, A.P., and Ranganath, C. (2007). The medial temporal lobe and recognition memory. Annu. Rev. Neurosci. *30*, 123–152.

Fletcher, M.L., and Wilson, D.A. (2002). Experience modifies olfactory acuity: acetylcholine-dependent learning decreases behavioral generalization between similar odorants. J. Neurosci. *22*, RC201.

Franks, K.M., Russo, M.J., Sosulski, D.L., Mulligan, A.A., Siegelbaum, S.A., and Axel, R. (2011). Recurrent circuitry dynamically shapes the activation of piriform cortex. Neuron *72*,

49–56.

Fusi, S., Miller, E.K., and Rigotti, M. (2016). Why neurons mix: high dimensionality for higher cognition. Curr. Opin. Neurobiol. *37*, 66–74.

Ghosh, S., and Chattarji, S. (2015). Neuronal encoding of the switch from specific to generalized fear. Nat. Neurosci. *18*, 112–120.

Gschwend, O., Abraham, N.M., Lagier, S., Begnaud, F., Rodriguez, I., and Carleton, A. (2015). Neuronal pattern separation in the olfactory bulb improves odor discrimination learning. Nat. Neurosci. *18*, 1474–1482.

Hafting, T., Fyhn, M., Molden, S., Moser, M.-B., and Moser, E.I. (2005). Microstructure of a spatial map in the entorhinal cortex. Nature *436*, 801–806.

Hainmueller, T., and Bartos, M. (2018). Parallel emergence of stable and dynamic memory engrams in the hippocampus. Nature.

Han, Z., Zhang, X., Zhu, J., Chen, Y., and Li, C.T. (2018). High-Throughput Automatic Training System for Odor-Based Learned Behaviors in Head-Fixed Mice. Front. Neural Circuits *12*, 15.

Hargreaves, E.L., Rao, G., Lee, I., and Knierim, J.J. (2005). Major dissociation between medial and lateral entorhinal input to dorsal hippocampus. Science *308*, 1792–1794.

Heale, V.R., and Vanderwolf, C.H. (1994). Dentate gyrus and olfactory bulb responses to olfactory and noxious stimulation in urethane anaesthetized rats. Brain Res. *652*, 235–242.

Heale, V.R., and Vanderwolf, C.H. (1999). Odor-induced fast waves in the dentate gyrus depend on a pathway through posterior cerebral cortex: effects of limbic lesions and trimethyltin. Brain Res. Bull. *50*, 291–299.

Igarashi, K.M., Lu, L., Colgin, L.L., Moser, M.-B., and Moser, E.I. (2014). Coordination of entorhinal-hippocampal ensemble activity during associative learning. Nature *510*, 143–147.

Iurilli, G., and Datta, S.R. (2017). Population Coding in an Innately Relevant Olfactory Area. Neuron *93*, 1180–1197.e7.

Khan, U.A., Liu, L., Provenzano, F.A., Berman, D.E., Profaci, C.P., Sloan, R., Mayeux, R., Duff, K.E., and Small, S.A. (2014). Molecular drivers and cortical spread of lateral entorhinal cortex dysfunction in preclinical Alzheimer's disease. Nat. Neurosci. *17*, 304–311.

Kheirbek, M.A., Drew, L.J., Burghardt, N.S., Costantini, D.O., Tannenholz, L., Ahmari, S.E., Zeng, H., Fenton, A.A., and Hen, R. (2013). Differential control of learning and anxiety along the dorsoventral axis of the dentate gyrus. Neuron *77*, 955–968.

Knierim, J.J., and Neunuebel, J.P. (2016). Tracking the flow of hippocampal computation: Pattern separation, pattern completion, and attractor dynamics. Neurobiol. Learn. Mem. *129*, 38–49.

Knierim, J.J., Neunuebel, J.P., and Deshmukh, S.S. (2014). Functional correlates of the lateral and medial entorhinal cortex: objects, path integration and local-global reference frames. Philos. Trans. R. Soc. Lond. B Biol. Sci. *369*, 20130369.

Komiyama, T., Sato, T.R., O'Connor, D.H., Zhang, Y.-X., Huber, D., Hooks, B.M., Gabitto, M., and Svoboda, K. (2010). Learning-related fine-scale specificity imaged in motor cortex circuits of behaving mice. Nature *464*, 1182–1186.

Krettek, J.E., and Price, J.L. (1977). Projections from the amygdaloid complex and adjacent olfactory structures to the entorhinal cortex and to the subiculum in the rat and cat. J. Comp. Neurol. *172*, 723–752.

Lafaille-Magnan, M.-E., Poirier, J., Etienne, P., Tremblay-Mercier, J., Frenette, J., Rosa-Neto, P., Breitner, J.C.S., and PREVENT-AD Research Group (2017). Odor identification as a biomarker of preclinical AD in older adults at risk. Neurology *89*, 327–335.

Leitner, F.C., Melzer, S., Lütcke, H., Pinna, R., Seeburg, P.H., Helmchen, F., and Monyer, H. (2016). Spatially segregated feedforward and feedback neurons support differential odor processing in the lateral entorhinal cortex. Nat. Neurosci. *19*, 935–944.

Lepousez, G., and Lledo, P.-M. (2013). Odor discrimination requires proper olfactory fast oscillations in awake mice. Neuron *80*, 1010–1024.

Li, W.L., Chu, M.W., Wu, A., Suzuki, Y., Imayoshi, I., and Komiyama, T. (2018). Adult-born neurons facilitate olfactory bulb pattern separation during task engagement. Elife *7*.

Li, Y., Xu, J., Liu, Y., Zhu, J., Liu, N., Zeng, W., Huang, N., Rasch, M.J., Jiang, H., Gu, X., et al. (2017). A distinct entorhinal cortex to hippocampal CA1 direct circuit for olfactory associative learning. Nat. Neurosci. *20*, 559–570.

Likhtik, E., Stujenske, J.M., Topiwala, M.A., Harris, A.Z., and Gordon, J.A. (2014). Prefrontal entrainment of amygdala activity signals safety in learned fear and innate anxiety. Nat. Neurosci. *17*, 106–113.

Litwin-Kumar, A., Harris, K.D., Axel, R., Sompolinsky, H., and Abbott, L.F. (2017). Optimal Degrees of Synaptic Connectivity. Neuron *93*, 1153–1164.e7.

Liu, D., Gu, X., Zhu, J., Zhang, X., Han, Z., Yan, W., Cheng, Q., Hao, J., Fan, H., Hou, R., et al. (2014). Medial prefrontal activity during delay period contributes to learning of a working memory task. Science *346*, 458–463.

Luna, V.M., Anacker, C., Burghardt, N.S., Khandaker, H., Andreu, V., Millette, A., Leary, P., Ravenelle, R., Jimenez, J.C., Mastrodonato, A., et al. (2019). Adult-born hippocampal neurons bidirectionally modulate entorhinal inputs into the dentate gyrus. Science *364*, 578–583.

MacDonald, C.J., Carrow, S., Place, R., and Eichenbaum, H. (2013). Distinct hippocampal time cell sequences represent odor memories in immobilized rats. J. Neurosci. *33*, 14607–14616.

Martin, C., Beshel, J., and Kay, L.M. (2007). An olfacto-hippocampal network is dynamically involved in odor-discrimination learning. J. Neurophysiol. *98*, 2196–2205.

McHugh, T.J., Jones, M.W., Quinn, J.J., Balthasar, N., Coppari, R., Elmquist, J.K., Lowell, B.B., Fanselow, M.S., Wilson, M.A., and Tonegawa, S. (2007). Dentate gyrus NMDA receptors mediate rapid pattern separation in the hippocampal network. Science *317*, 94–99.

McKenzie, S., Keene, C.S., Farovik, A., Bladon, J., Place, R., Komorowski, R., and Eichenbaum, H. (2016). Representation of memories in the cortical–hippocampal system: Results from the application of population similarity analyses. Neurobiol. Learn. Mem. *134*, 178–191.

McNaughton, B.L., and Morris, R.G.M. (1987). Hippocampal synaptic enhancement and information storage within a distributed memory system. Trends Neurosci. *10*, 408–415.

McNaughton, B.L., Battaglia, F.P., Jensen, O., Moser, E.I., and Moser, M.-B. (2006). Path integration and the neural basis of the'cognitive map'. Nat. Rev. Neurosci. *7*, 663.

Meister, M., and Bonhoeffer, T. (2001). Tuning and topography in an odor map on the rat olfactory bulb. J. Neurosci. *21*, 1351–1360.

Morgan, C.D., Nordin, S., and Murphy, C. (1995). Odor identification as an early marker for Alzheimer's disease: impact of lexical functioning and detection sensitivity. J. Clin. Exp. Neuropsychol. *17*, 793–803.

Nakashiba, T., Cushman, J.D., Pelkey, K.A., Renaudineau, S., Buhl, D.L., McHugh, T.J., Rodriguez Barrera, V., Chittajallu, R., Iwamoto, K.S., McBain, C.J., et al. (2012). Young dentate granule cells mediate pattern separation, whereas old granule cells facilitate pattern completion. Cell *149*, 188–201.

Nakazawa, K., Quirk, M.C., Chitwood, R.A., Watanabe, M., Yeckel, M.F., Sun, L.D., Kato, A., Carr, C.A., Johnston, D., Wilson, M.A., et al. (2002). Requirement for hippocampal CA3 NMDA

receptors in associative memory recall. Science *297*, 211–218.

Olton, D.S., Becker, J.T., and Handelmann, G.E. (1979). Hippocampus, space, and memory. Behav. Brain Sci. *2*, 313–322.

O'reilly, R.C., and McClelland, J.L. (1994). Hippocampal conjunctive encoding, storage, and recall: Avoiding a trade-off. Hippocampus *4*, 661–682.

Otazu, G.H., Chae, H., Davis, M.B., and Albeanu, D.F. (2015). Cortical Feedback Decorrelates Olfactory Bulb Output in Awake Mice. Neuron *86*, 1461–1477.

Pavesi, E., Gooch, A., Lee, E., and Fletcher, M.L. (2012). Cholinergic modulation during acquisition of olfactory fear conditioning alters learning and stimulus generalization in mice. Learn. Mem. *20*, 6–10.

Resnik, J., and Paz, R. (2015). Fear generalization in the primate amygdala. Nat. Neurosci. *18*, 188–190.

Rigotti, M., Ben Dayan Rubin, D., Morrison, S.E., Salzman, C.D., and Fusi, S. (2010). Attractor concretion as a mechanism for the formation of context representations. Neuroimage *52*, 833–847.

Rigotti, M., Barak, O., Warden, M.R., Wang, X.-J., Daw, N.D., Miller, E.K., and Fusi, S. (2013). The importance of mixed selectivity in complex cognitive tasks. Nature *497*, 585–590.

Roland, B., Deneux, T., Franks, K.M., Bathellier, B., and Fleischmann, A. (2017). Odor identity coding by distributed ensembles of neurons in the mouse olfactory cortex. eLife Sciences *6*,

e26337.

Rolls, E.T., and Tovee, M.J. (1995). Sparseness of the neuronal representation of stimuli in the primate temporal visual cortex. Journal of Neurophysiology *73*, 713–726.

Rolls, E.T., Treves, A., and Rolls, E.T. (1998). Neural networks and brain function.

Room, P., Groenewegen, H.J., and Lohman, A.H.M. (1984). Inputs from the olfactory bulb and olfactory cortex to the entorhinal cortex in the cat. Exp. Brain Res. *56*, 488–496.

Sahay, A., Wilson, D.A., and Hen, R. (2011). Pattern separation: a common function for new neurons in hippocampus and olfactory bulb. Neuron *70*, 582–588.

Schaffer, E.S., Stettler, D.D., Kato, D., Choi, G.B., Axel, R., and Abbott, L.F. (2018). Odor Perception on the Two Sides of the Brain: Consistency Despite Randomness. Neuron *98*, 736–742.e3.

Schmidt-Hieber, C., Jonas, P., and Bischofberger, J. (2004). Enhanced synaptic plasticity in newly generated granule cells of the adult hippocampus. Nature *429*, 184–187.

Sheintuch, L., Rubin, A., Brande-Eilat, N., Geva, N., Sadeh, N., Pinchasof, O., and Ziv, Y. (2017). Tracking the Same Neurons across Multiple Days in Ca2+ Imaging Data. Cell Rep. *21*, 1102–1115.

Shipley, M.T., and Adamek, G.D. (1984). The connections of the mouse olfactory bulb: a study using orthograde and retrograde transport of wheat germ agglutinin conjugated to horseradish peroxidase. Brain Res. Bull. *12*, 669–688.

Sosulski, D.L., Bloom, M.L., Cutforth, T., Axel, R., and Datta, S.R. (2011). Distinct representations of olfactory information in different cortical centres. Nature *472*, 213–216.

Stettler, D.D., and Axel, R. (2009). Representations of odor in the piriform cortex. Neuron *63*, 854–864.

Treves, A., and Rolls, E.T. (1994). Computational analysis of the role of the hippocampus in memory. Hippocampus *4*, 374–391.

Tulving, E., and Markowitsch, H.J. (1998). Episodic and declarative memory: role of the hippocampus. Hippocampus *8*, 198–204.

Uchida, N., and Mainen, Z.F. (2003). Speed and accuracy of olfactory discrimination in the rat. Nat. Neurosci. *6*, 1224–1229.

Vanderwolf, C.H. (1992). Hippocampal activity, olfaction, and sniffing: an olfactory input to the dentate gyrus. Brain Res. *593*, 197–208.

Vassilaki, M., Christianson, T.J., Mielke, M.M., Geda, Y.E., Kremers, W.K., Machulda, M.M., Knopman, D.S., Petersen, R.C., Lowe, V.J., Jack, C.R., Jr, et al. (2017). Neuroimaging biomarkers and impaired olfaction in cognitively normal individuals. Ann. Neurol. *81*, 871–882.

Vinje, W.E., and Gallant, J.L. (2000). Sparse coding and decorrelation in primary visual cortex during natural vision. Science *287*, 1273–1276.

Vivar, C., Potter, M.C., Choi, J., Lee, J.-Y., Stringer, T.P., Callaway, E.M., Gage, F.H., Suh, H., and van Praag, H. (2012). Monosynaptic inputs to new neurons in the dentate gyrus. Nat.

Commun. *3*, 1107.

Wilson, R.C., and Steward, O. (1978). Polysynaptic activation of the dentate gyrus of the hippocampal formation: an olfactory input via the lateral entorhinal cortex. Exp. Brain Res. *33*, 523–534.

Wilson, D.I.G., Watanabe, S., Milner, H., and Ainge, J.A. (2013). Lateral entorhinal cortex is necessary for associative but not nonassociative recognition memory. Hippocampus *23*, 1280–1290.

Witter, M.P., Doan, T.P., Jacobsen, B., Nilssen, E.S., and Ohara, S. (2017). Architecture of the Entorhinal Cortex A Review of Entorhinal Anatomy in Rodents with Some Comparative Notes. Front. Syst. Neurosci. *11*, 46.

Woods, N.I., Vaaga, C.E., Chatzi, C., Adelson, J.D., Collie, M.F., Perederiy, J.V., Tovar, K.R., and Westbrook, G.L. (2018). Preferential Targeting of Lateral Entorhinal Inputs onto Newly Integrated Granule Cells. J. Neurosci. *38*, 5843–5853.

Xu, W., and Wilson, D.A. (2012). Odor-evoked activity in the mouse lateral entorhinal cortex. Neuroscience *223*, 12–20.

Yassa, M.A., and Stark, C.E.L. (2011). Pattern separation in the hippocampus. Trends Neurosci. *34*, 515–525.

Zhou, P., Resendez, S.L., Rodriguez-Romaguera, J., Jimenez, J.C., Neufeld, S.Q., Giovannucci, A., Friedrich, J., Pnevmatikakis, E.A., Stuber, G.D., Hen, R., et al. (2018).

Efficient and accurate extraction of in vivo calcium signals from microendoscopic video data. Elife *7*, e28728.

Zhu, Y., Nachtrab, G., Keyes, P.C., Allen, W.E., Luo, L., and Chen, X. (2018). Dynamic salience processing in paraventricular thalamus gates associative learning. Science *362*, 423–429.

Supplementary Figure 2.1

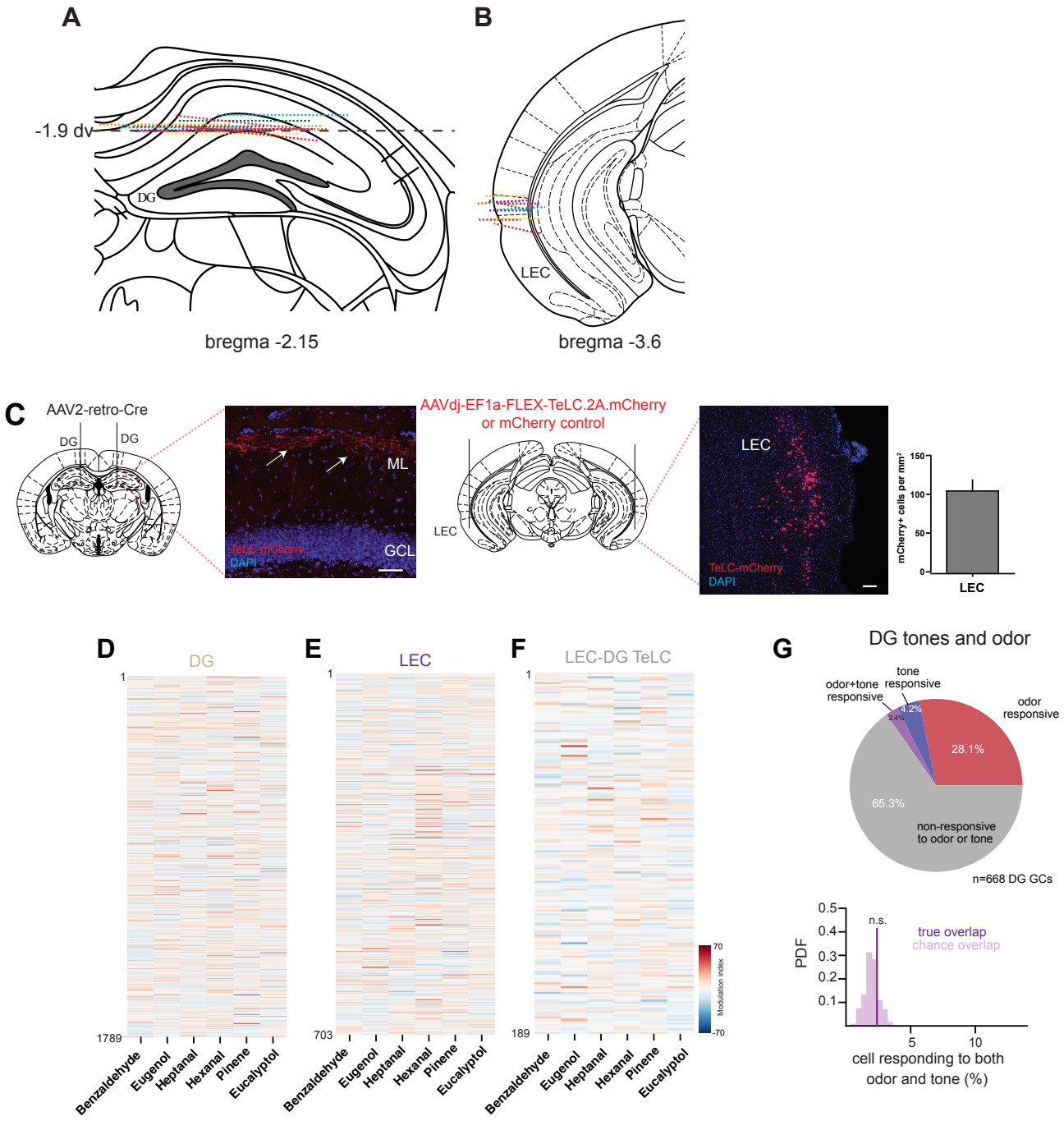

Supplementary figure 2.1 (Related to Figures 2.1-5)
A-B. Reconstructed lens implant locations of total of DG (A) and LEC mice (B) used throughout study, with dotted line indicating the estimated location of the impression left by lens on tissue, superimposed on mouse brain atlas. **C.** LEC-DG TeLC based synaptic silencing, with mCherry positive terminals shown within the outer molecular layer shown on left (arrowheads), and a representative coronal section showing mCherry positive cells located in LEC on right, with mCherry positive cells quantified across animals used throughout study (mean +/- SEM, n=11 mice). Scale bars: 100 microns. **D-F.** Odors elicit distributed responses in the population of recorded DG GCs. Modulation index (see Methods) for each cell (in rows) combined across n = 8 DG mice (D), n=7 LEC mice (E) and n= 3 LEC-DG TeLC mice (F) is color coded for the panel of six neutral odors (in columns). Same 6 neutral odors as labeled in Figure 1. **G.** Cells co-responsive to tones and odors are not more prevalent than expected by shuffling odor and tone responses across cells. Mice were presented 3 neutral odors and 3 tones (see Methods). Odor responsive and tone responsive overlap cells (pie chart, above) are compared to a chance overlap distribution obtained by pooling cells from all mice. Pie chart shows percentage of only tone, only odor, tone+odor co-responsive cells, or non-responsive cells. Odor responsive and tone responsive overlap cells are compared to a chance overlap distribution (n=668 cells in 3 mice, $p>0.05$). Error bars represent SEM. For exact *P* values, see Supplementary Table 2.1.

Supplementary Figure 2.2

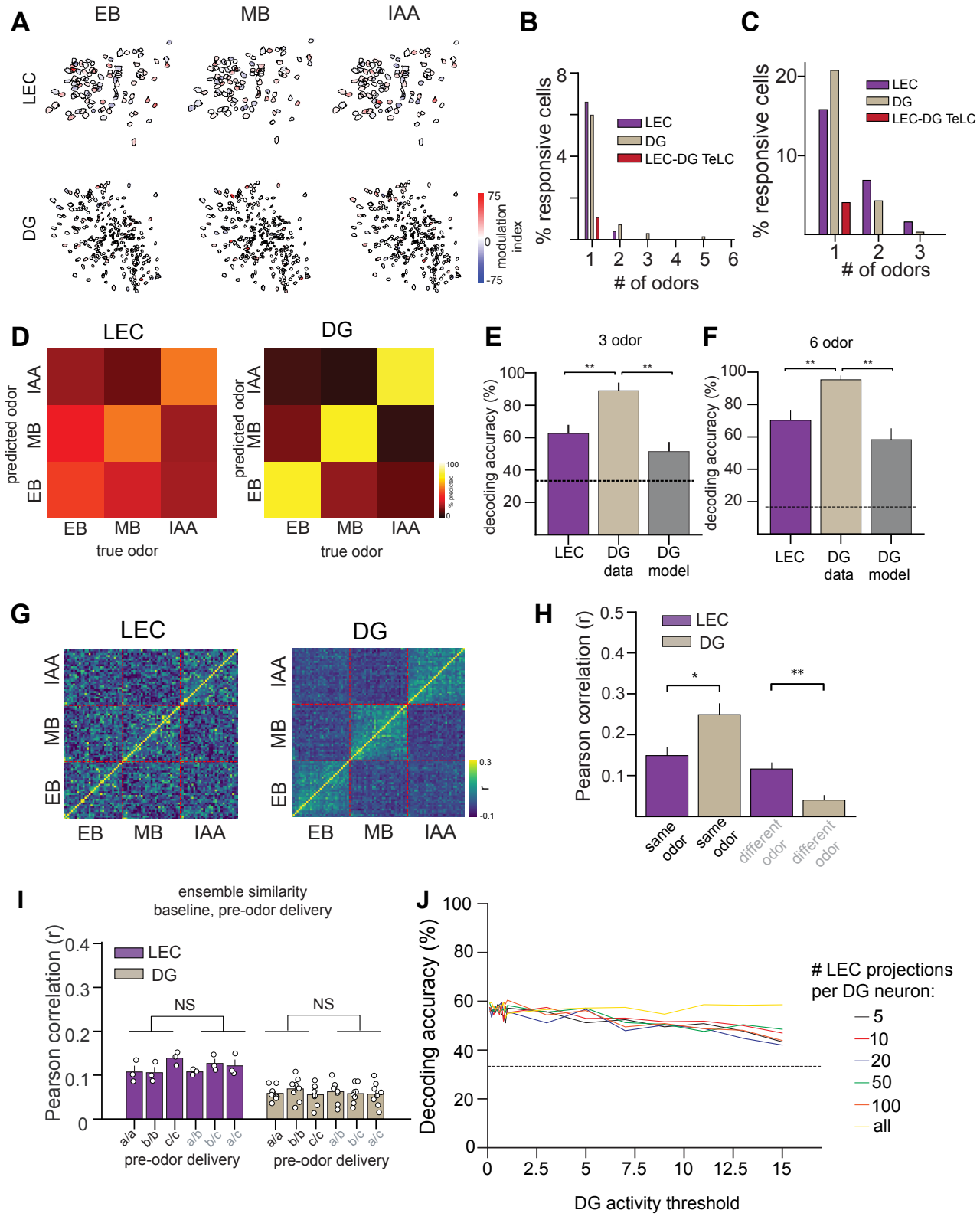

Supplementary figure 2.2 (related to figure 2.4)
A. Odor responses to EB/MB/IAA are sparse and randomly distributed in the FOV. Spatial footprints shown from an example mouse, with overlaid modulation index for each cell (see Methods). **B.** Percent responsive cells in 6 odor (benzaldehyde, eugenol, heptanal, hexanal, pinene, eucalyptol) experiment in DG, LEC and LEC-DG TeLC mice. **C.** Percent responsive cells in 3 odor experiment (ethyl butyrate, methyl butyrate, isoamyl acetate) in DG, LEC and LEC-DG TeLC mice. **D**. Confusion matrices for decoding accuracy in the three odor experiment in DG and LEC. G-H**. E-F.** The accuracy of a decoder to classify odor identity was greater in DG than in LEC activity for both the 3 odor (E) and 6 odor (F) experiment. A model of DG based on random connectivity with comparable levels of sparseness could not perform as well as real DG data in classifying odor identity in either the 3 odor or 6 odor design . (linear SVM classifier with matched number of cells in DG and LEC, 3 odor: n=190 cells (n-matched, from 3 LEC and 8DG mice), 6 odor n=703 cells, (n-matched, from 3 LEC and 8DG mice), t-test, **p<0.01). **G.** Trial by trial similarity matrix in DG and LEC mice for the three odor experiment. **H**. Odor ensembles were more distinct for presentation of different odorants in DG than LEC mice, and in this experiment, within odor correlations were higher in DG compared to LEC mice. (Pearson correlation of activity vectors during odor presentation, n= 8 DG mice, 3 LEC mice, Mann-Whitney, **p<0.01, * p<0.05). **I**. Ensemble similarities computed in non-odor delivery baseline periods. **J**. Decoding accuracy in the DG GCs model doesn't depend on sparsity. We varied the proportion of LEC projections per DG GCs as well as the activation threshold for each model neuron. The parameters effectively change the sparsity of activations across neurons in DG and are the only parameters in the model. For each pair of parameters, we ran 10 models and report here the average decoding accuracy across models. Error bars represent SEM. For exact *P* values, see Supplementary Table 1.

Supplementary Figure 2.3

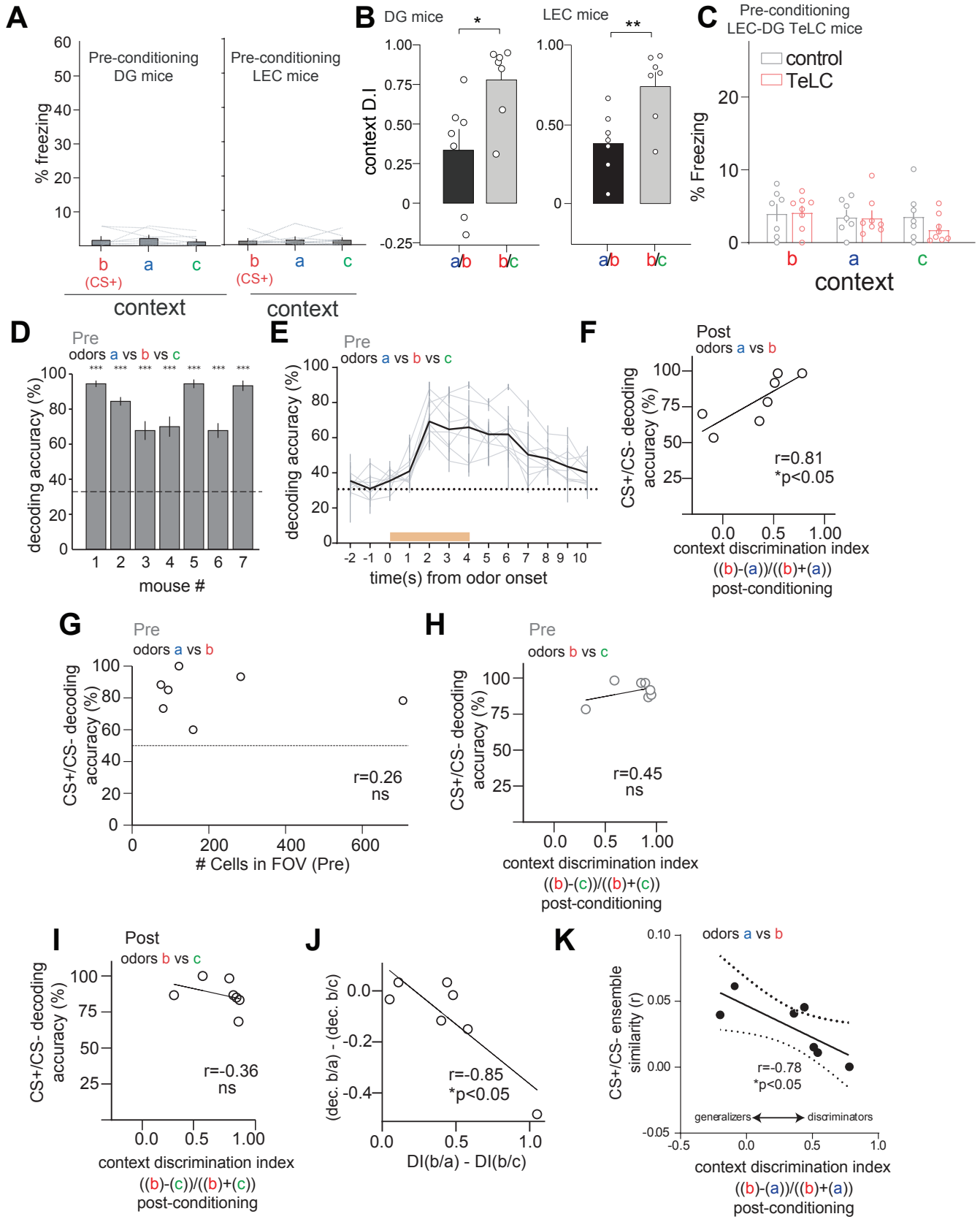

Supplementary figure 3 (related to Figure 2.4)
A. Left DG mice, right, LEC mice. Pre-conditioning percent time spent freezing to each context, showing lack of initial fear responses to neutral odorants (one-way ANOVA, $p>0.05$). **B.** Left DG mice, right, LEC mice. Context discrimination indices comparing a/b contexts and b/c contexts. In both the DG and LEC cohorts, mice were better at discriminating distinct context pairs (b/c) compared to context pairs (a/b) (n=7 mice/group, t-test , $p<0.05$). **C.** Preconditioning context discrimination did not differ between control and LEC-DG TeLC mice. **D.** Baseline, pre-learning odor identity could be decoded in all mice tested (3 odor decoding, SVM with linear kernel, one sample t-test, $p<0.001$ for all mice from chance decoding performance (see Methods for single animal decoding), error bars indicate SEM from cross validation of decoder). **E.** Odor identity could be decoded within 2s of odor onset (n=7 mice, all values mean +/- SEM for each mouse). For each 1s timebin, a different decoder is trained on the data for the corresponding bin. Generalization performance on held-out data is reported as decoding accuracy. The solid black line corresponds to mean across mice in each time bin. For all mice, the decoding performance was significantly higher than chance (dashed line) for several seconds after odor offset. **F.** Decoding accuracy of odor a vs odor b in the post-conditioning session correlated with context freezing behavior (Pearson $r=0.81$, $p<0.05$, n=7 mice). **G.** Decoding performance for a/b does not depend on number of cells per mouse (Pearson $r=0.26$, $p>0.05$, n=7 mice). **H-I.** Decoding accuracy of odors b and c (MB and IAA) before or after fear learning does not correlate with freezing behavior after learning (pre $r=0.45$, post $r=-0.36$, n=7 mice, linear fit with solid line, $p>0.05$, n=7 mice). **J.** Better discriminability of contexts a/b vs b/c correlate with decoding of these odors. (Pearson $r=-0.85$, $p<0.05$, n=7 mice). **K.** Pearson similarity ensemble metric was generated for odors from contexts a/b and plotted against pre-conditioning context discrimination index for contexts a/b. (Pearson $r=-0.78$ and $p<0.05$, n=7 mice). Error bars represent SEM. For exact *P* values, see Supplementary Table 1.

Supplementary Figure 2.4

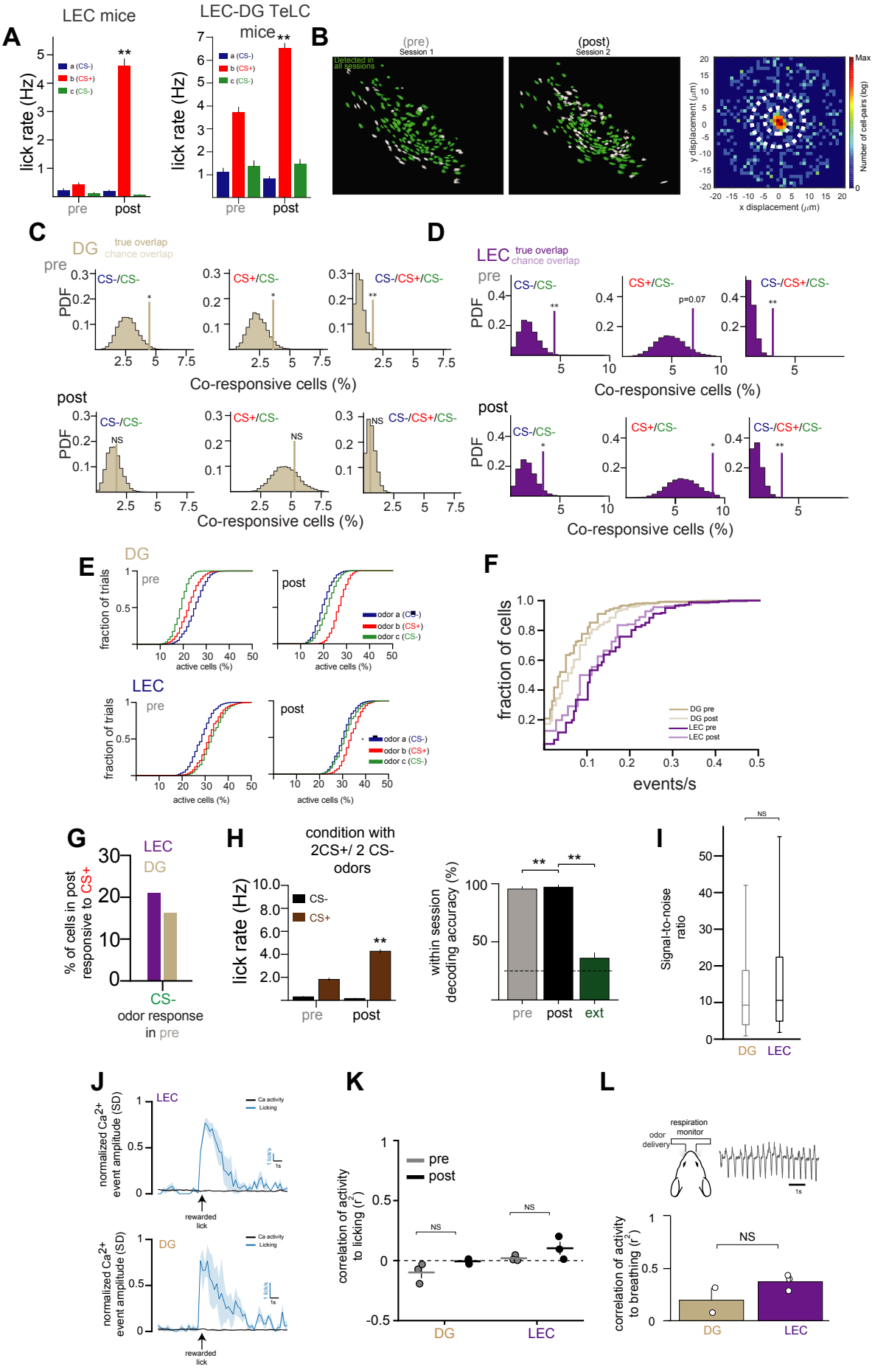

Supplementary Figure 2.4 (related to Figure 5)
A. Average lick rates during the odor and trace period on day 1 (pre) and day 3 (post) in LEC mice, and in LEC-DG TeLC mice, as analyzed in Figure 4 (Mann-Whitney, **p<0.001) **B.** Example pre and post spatial footprints showing registration results of identified ROIs that are within centroid differences established within 95% of a confidence interval. Average centroid displacement shown on right for registering cells pre to post, using *CellReg* algorithm. **C-D.** Overlaps of cell responses for odor pairs and triples before and after learning for all recorded DG GCs (C), and LEC cells (D), (level of significance for 10,000 shufflings, , **p<0.01, *p<0.05, n=3 DG mice and n=3 LEC mice). **E.** Fraction of trials that cells are active, plotted for each individual odor in DG and LEC. After learning, an increased percentage of cells are responsive to the CS+ odor across trials within DG. (DG post, CS+ odor vs all others KS test, P<0.001). **F.** Cumulative distribution plot arranged by calcium event rate pre and post learning (average events per second for each cell during entire imaging period, KS test, p<0.001 between LEC and DG). **G.** Odor responses in Post for cross-session registered cells. Cells were classified as CS- (IAA) responsive Pre, and then their responses were determined in Post. Unlike with the EB/MB pair in Figure 5K,a similar proportion of LEC and DG neurons became responsive to the CS+ odor after learning. (n=3 DG mice, 359 cells; n=3 LEC mice, 182 cells X2 test, p<0.01). **H**. Four odor associative learning task. Four distinct odors were given, and two CS+ odors were followed by a trace period and a sucrose reward (CS+ assignment randomized among mice). *Left*, lick rate to CS+ odors in pre and post learning.(n=2 mice, **p>0.01) Mice show CS+ biased licking on the first day in this design. Proportion of CS+ responding cells in the DG increase after learning (n=2 mice p<0.01) *Right.* High decoding accuracy on D1 with improvement with learning. Decoding accuracy was reduced in an extinction session with the lick spout removed (n=443 cells, from 2 DG mice, **p<0.01). **I.** Signal-to-noise (SNR) for all cells combined across LEC (n=360 in 3 mice) and DG mice (n=531 in 3 mice). The horizontal line represents the median SNR for each population, the boxes represent first and thirds quartile of the distribution and the whiskers represent 9th and 95th percentiles. The two distributions are not significantly different (t-test, p=0.87). **J.** A cohort of DG and LEC mice were imaged for sucrose responses in the absence of odor delivery. For all cells we calculated a peri-stimulus time histogram (PSTH) for normalized Ca^{2+} activity (black line) triggered on the first lick after sucrose availability (licking rate in blue). Reward consumption did not modulate DG (531 cells in 3 mice) or LEC (n=360 cells in 3 mice) activity. Shaded areas are +/-SEM. **K-L.** Linear regression of lick rates (K) and breathing rates (L) and Ca^{2+} in DG and LEC before (pre) and after (post) associative learning (see Methods). We found that neural activity is not significantly correlated to lick rates (R^2 is approximately zero for all animals in both sessions, DG pre n=531 cells in 3 mice, DG post n=627 cells in 3 mice, LEC pre n=360 cells in 3 mice, LEC post n=266 cells in 3 mice, no significant difference between pre and post in either group, p>0.05). In addition, we found that correlations of breathing rates with Ca^{2+} did not differ between LEC and DG recordings (n=2 LEC mice, 3 DG mice, Mann Whitney, p>0.05). All error bars represent mean +/- SEM. For exact *P* values, see Supplementary Table 1.

Supplementary Table 1 (related to all Figures). Summary of statistics in all figure panels in manuscript.

figure	unit of comparison	variable	n	test	results (p-value)
Fig. 2.3c	pseudopopulation of cells, 10000 iterations (see methods)	6 odor decoding accuracy	dg=8, lec=7, tent=3, 189 cells, n matched	mann whitney U	LEC vs DG p<0.0001, DG vs LEC-DG TeLC p<0.0001
Fig. 2.3e	cells from trial pairs	lec same, lec diff	42, 105 (from 7 LEC mice)	t-test for independence	t=5.69, p=6.5E-08
		lec same, dg same	42, 48 (8 DG and 7 LEC mice)		t=-.071, p=0.483
		dg same, dg diff	48, 120 (8 DG mice)		t=-7.81, p=0.6.28E-13
		lec diff, dg diff	105, 120 (8 DG and 7 LEC mice)		t=-2.556, p=0.01
		TeLC same, TeLC diff	18, 45 (3 LEC-DG TeLC mice)		t=-1.65, p=0.104
Fig. 2.4a	mice	percent time spent freezing to each odor	8 TeLC, 7 control	repeated measures ANOVA	odorXgeno interaction F = 6.16 and p<0.0001
				Holm-Sidak's multiple comparison	odor eb(a), p=0.303 odor mb(b), p<0.001 odor iaa (c), p=0.755
Fig 2.4c	mice	percent time spent freezing to each odor	7DG	one-way ANOVA	ANOVA summary: F=37.6, p<0.001
				Holm-Sidak's multiple comparison	odors mb (b) vs. eb (a), p=0.007 odors mb (b) vs. iaa (c), p=<0.001 odors eb (a) vs. iaa (c), p=0.005
Fig. 2.4d	mice	discrimination index of (a/b) vs. PRE-conditionig decoding performance (a/b)	7 DG	pearson correlation coefficient	r=0.959, p=0.0003
Fig 2.4e	mice	percent time spent freezing to each odor	7LEC	one-way ANOVA	ANOVA summary: F=30.26, p<0.001
				Holm-Sidak's multiple comparison	dors mb (b) vs. eb (a), p<0.001 odors mb (b) vs. iaa (c), p<0.001 odors eb (a) vs. iaa (c), p=0.006
Fig. 2.4f	mice	discrimination index of (a/b) vs. PRE-conditionig decoding performance (a/b)	7 DG	pearson correlation coefficient	r=-0.2406, p=0.3016
Fig. 2.5c	animals	lick rate (Hz) during 2s delay vs. baseline	3 DG	Mann-Whitney	U=1187.5, p=8.62e-18
Fig. 2.5f	cells	co-responsive odor a/b cells vs. chance overlap PRE and POST learning	359 (3 DG mice)	p-value relative to shuffle (10,000)	PRE: EB/MB (a/b): p=0.0044 POST: EB/MB (a/b): p=0.312
Fig. 2.5g	cells	co-responsive odor a/b cells vs. chance overlap PRE and POST learning	182 (3 LEC mice)	p-value relative to shuffle (10,000)	PRE: EB/MB (a/b): p=0.00413 POST: EB/MB (a/b): p=0.0129
Fig. 2.5h	cells	fraction total cells active for all odors PRE vs. POST learning	359 (3 DG mice)	t-test for independence, bonferroni correction for n=6	EB (a): p= 3.970e-05 MB (b): p=4.688e-04
Fig. 2.5i	cells	fraction total cells active for all odors PRE vs. POST learning	182 (3 LEC mice)	t-test for independence, bonferroni correction for n=6	EB (a): p=5.49e-01 MB (b): p=1.00
Fig. 2.5j	cells	fraction total cells active for all odors PRE vs. POST learning	150 cells (2 LEC-DG TeLC mice)	t-test for independence	EB (a): t=-4.222 p=4.78E-05 MB (b): t=-6.176 p=9.63E-09
Fig. 2.5K	cells	fraction of responsive cells in POST among responsive cells in PRE for each odor	182 LEC and 359 DG, PRE and POST learning	Chi-square, Bonferroni adjusted	EB (odor a, CS-) chi=56.0, p=9.4439e-10, p_adj=2.8332e-09 MB (odor b, CS+) chi=14.0, p=5.1181e-02, p_adj=1.5354e-01 IAA (odor c) chi=16.0, p=2.5116e-02, p_adj=7.5349e-02
Fig. 2.5l	mice	lifetime sparsity PRE vs. POST	3 DG	Mann-Whitney	U=1.45e+05, p=1.317e-03
	mice	lifetime sparsity PRE vs. POST	3 LEC	Mann-Whitney	U=4.36e+04, p=5.699e-02
Fig. 2.5m	mice	3 odor (a/b/c) decoding accuracy PRE vs. POST	n= 359 cells from 3 DG mice	Mann-Whitney	U=264.00, p=4.692e-03
	mice	3 odor (a/b/c) decoding accuracy pre vs. post	n=182 cells from 3 LEC mice	Mann-Whitney	U=282.00, p=1.1632e-02

figure	unit of comparison	variable	n	test	results (p-value)
	mice	3 odor (a/b/c) decoding accuracy pre vs. post	n=150 cells from 2 mice	Mann-Whitney	U=161.5, p=0.296
Fig. 2.5n	mice	across session decoding accuracy (3 odors (a/b/c))	3 DG and 3 LEC mice	Mann-Whitney	U= 2.28e03, p=1.082e-12
supplementary figures					
Fig. S2.1g	cells	odor and tone co-responsive cells vs. chance overlap	668 (3 DG mice)	p-value relative to shuffle (10,000)	p = 0.238
Fig S2.2e	n matched cells, 1000 iterations (see methods)	3 odor (a/b/c) decoding accuracy in LEC vs. DG vs. DG model	190 LEC vs. 190 DG (n-matched) n=3LEC, 8DG	t-test	LEC vs. DG: t=-25.04, p=2.22e-44
					DG vs. model: t=34.31, p=2.43e-72
Fig S2.2f	n matched cells, 1000 iterations (see methods)	6 odor (a/b/c) decoding accuracy in LEC vs. DG vs. DG model	703 LEC vs. 703 DG (n-matched) from 8 DG mice, 7 LEC mice	t-test	LEC vs. DG: t=-118, p<0.0001 DG vs. model: t=226, p<0.0001
Fig S2.2h	cells from trial pairs	lec same, dg same	(8 DG and 3 LEC mice)	t-test for independence	t=-2.09, p=0.04
		lec diff, dg diff	(8 DG and 3 LEC mice)		t=3.41, p=0.002
Fig. S2.2i	animals	Pearson correlation grouped for same odor vs. different odor	LEC 3 DG 8	Mann-Whitney Mann-Whitney	U=38.00, p=0.859 U=303.00, p=0.765
Fig. S2.3a	mice	percent time spent freezing to each odor	7 DG	one-way ANOVA Holm-Sidak's multiple comparison	ANOVA summary: F=0.5320, p=0.538 odors mb (b) vs. eb (a), p=0.851 odors mb (b) vs. iaa (c), p=0.851 odors eb (a) vs. iaa (c), p=0.330
			7 LEC	one-way ANOVA Holm-Sidak's multiple comparison	ANOVA summary: F=0.05242, p=0.937 odors mb (b) vs. eb (a), p=0.991 odors mb (b) vs. iaa (c), p=0.991 odors eb (a) vs. iaa (c), p=>0.999
Fig. S2.3b	mice	(a/b) discrimination index vs. (b/c) discrimination index	7 DG	t-test	t=-2.78, p=0.0167
Fig. S2.3b	mice	(a/b) discrimination index vs. (b/c) discrimination index	7 LEC	t-test	t=-3.188, p=0.0078
Fig. S2.3c	mice	percent time spent freezing to each odor	8 TeLC, 7 control	one-way ANOVA Holm-Sidak's multiple comparison	ANOVA summary: F=2.335, p=0.148 odors mb (b) vs. eb (a), p=0.560 odors mb (b) vs. iaa (c), p=0.06 odors eb (a) vs. iaa (c), p=0.424
Fig. S2.3d	mice	3 odor (a/b/c) PRE-conditioning decoding score	7 DG	t-test	p<0.0001 for all individual mice comparisons to chance
Fig. S2.3f	mice	discrimination index of (a/b) vs. POST-conditioning decoding performance (a/b)	7 DG	pearson correlation coefficient	r = 0.81, p = 0.0273
Fig. S2.3g	mice	number of cells per FOV vs. PRE-conditioning decoding accuracy (a/b)	7 DG	pearson correlation coefficient	r=0.26, p=0.579
Fig. S2.3h	mice	discrimination index of (b/c) vs. PRE-conditionig decoding performance (b/c)	7 DG	pearson correlation coefficient	r = 0.45, p = 0.312
Fig. S2.3i	mice	discrimination index of (b/c) vs. POST-conditionig decoding performance (b/c)	7 DG	pearson correlation coefficient	r = -0.36, p = 0.4298
Fig. S2.3j	mice	discrimination index difference (b/a-b/c) vs. decoding difference (b/a-b/c)	7 DG	pearson correlation coefficient	r=-0.85, p=0.014

figure	unit of comparison	variable	n	test	results (p-value)
Fig. S2.3k	mice	discrimination index of (a/b) vs. pre-conditionig ensemble pearson similarity metric (a/b)	7 DG	pearson correlation coefficient	r=-0.78, p=0.02
Fig. S2.4a	mice	lick rate (Hz) during 2s delay vs. baseline	3 LEC	Mann-Whitney	U=285.00 , p=2.095e-28
Fig. S2.4a	mice	lick rate (Hz) during 2s delay vs. baseline	2 LEC-DG TeLC	Mann-Whitney	U=514.0 , p=6.634e-12
Fig. S2.4c	cells	co-responsive odor cells vs. chance overlap PRE and POST learning	359 (3 DG mice)	p-value relative to shuffle (10,000)	PRE: EB/IAA (a/c): p=0.0115 PRE: MB/IAA (b/c): p=0.0395 PRE: MB/EB/IAA (a/b/c): p=0.000494 POST: EB/IAA (a/c): p=0.0223 POST: MB/IAA (b/c): p=0.0448 POST: EB/MB/IAA (a/b/c): p=1.39E-06
Fig. S2.4d	cells	co-responsive odor cells vs. chance overlap PRE and POST learning	182 (3 LEC mice)	p-value relative to shuffle (10,000)	PRE: EB/IAA (a/c): p=0.001367 PRE: MB/IAA (b/c): p=0.0710 PRE: MB/EB/IAA (a/b/c): p=6.36E-08 POST: EB/IAA (a/c): p=0.0223 POST: MB/IAA (b/c): p=0.0448 POST: EB/MB/IAA (a/b/c): p=1.39E-06
Fig. S2.4e	cells	cumulative distribution function of percent active cells vs. number of trials active, PRE and POST learning for odors a, b, c	182 LEC and 359 DG, PRE and POST learning	parametric t-test for independence, Bonferroni adjusted for n=12	LEC PRE: EB/MB (a/b): t=-3.11, p=2.87e-03 EB/IAA (a/c): t=-3.83, p=3.12e-04 MB/IAA (b/c): t=-0.654, p=5.15e-01 LEC POST: EB/MB (a/b): t=-3.58, p=6.911e-04 EB/IAA (a/c): t=-3.58, p=7.21e-01 MB/IAA (b/c): t=3.06, p=3.32e-03 DG PRE: EB/MB (a/b): t=2.60, p=1.156e-02 EB/IAA (a/c): t=6.03, p=1.184e-07 MB/IAA (b/c): t=3.31, p=1.57e-03 DG POST: EB/MB (a/b): t=-8.83, p=2.45e-12 EB/IAA (a/c): t=-2.50, p=1.49e-02 MB/IAA (b/c): t=6.18, p=6.79e-08
Fig. S2.4f	cells	cumulative distribution function for event rate, PRE vs. POST learning for LEC and DG	182 LEC and 359 DG, PRE and POST learning	KS 2-samples	LEC p = 0.0124, DG p = 0.00002554, LEC adjusted Bonf. p = 0.02482, DG adjusted Bonf. P<0.001
Fig. S2.4g	cells	fraction of responsive cells in POST among responsive cells in PRE for each odor	182 LEC and 359 DG, PRE and POST learning	Chi-square, Bonferroni adjusted	IAA (odor c, CS-) chi=16.0, p=2.5116e-02, p_adj=7.5349e-02
Fig. S2.4h	mice	lick rate (Hz) during 2s delay vs. baseline	2 mice	Mann-Whitney	pre vs post U=10648.0, p<0.001
Fig. S2.4h	1000 iterations (see methods)	4 odor decoding accuracy	n=443 cells from 2 DG mice	Mann-Whitney	pre vs post U=2.68e+03, p=1.488e-08, post vs ext U=1.00e+04, p=2.455e-34
Fig S2.4i	cells	SNR	n= 3 DG mice (531 cells), 3 LEC mice (360 cells)	t-test	t=-0.160, p=0.87
Fig S2.4k	mice	correlation to licking (pre vs post)	N=3 LEC, 3 DG	Mann-Whitney	DG U=0.0, p=0.08, LEC U=1.0, p=0.19
Fig S2.4l	mice	correlation to breathing (LEC vs DG)	N=2 LEC, 3 DG	Mann-Whitney	U=5.0, p=0.386

Chapter 3: Conclusions

Using 2-photon imaging in adult, behaving mice, we have demonstrated odor-evoked responses within the dentate gyrus (DG), and went on to further demonstrate odor-responses in an upstream input region, the lateral entorhinal cortex (LEC). Looking closely at the characteristics of these responses in each region, we found that both areas have cells that are reliably responsive to specific odors, and a wide range of odors can elicit these robust responses. The lateral entorhinal cortex was more likely to contain multi-odor responsive neurons, whereas dentate granule cells were more likely to exhibit responses to just a single odorant in the panels tested. When we looked at the population-wide responses, both areas encoded odorant identity by recruiting ensembles specific to that odor. Indeed, when a linear decoder was used, the identity of an odor could be classified with around ~90% accuracy in dentate granule neurons. Moreover, the DG, but not LEC, coded for the differences between chemically similar odors to an extent that was correlated with the behavioral performance of an animal in distinguishing those similar odors in a fear learning task. Using appetitive conditioning, these neural-behavior correlations did not exist, but dentate granule neurons shifted their coding of odor information along the course of learning to preferentially encode the conditioned stimulus, lowering responsivity to the non-CS odors. These results collectively demonstrate that the dentate gyrus receives odor information from the lateral entorhinal cortex and enhances the separation

between relevant and irrelevant odorant cues, which may then be used by downstream hippocampal areas to form specific odor memories (**Figure 3.1**).

Olfaction has been studied in pain-staking detail for many decades in initial sensory processing areas, with olfactory information first arriving at the olfactory bulb and broadcasting efferents to several downstream areas, including the piriform cortex and lateral entorhinal cortex (Blazing and Franks, 2020; Giessel and Datta, 2014; Pashkovski et al., 2020; Sosulski et al., 2011; Stettler and Axel, 2009; Vassar et al., 1994). More recently, odor responses in lateral entorhinal cortex have been investigated with 2-photon imaging in anesthetized mice, and they reported similar results to what we observed--robust responses to odorants in a subpopulation of LEC neurons (Leitner et al., 2016). However, our approach has several advantages and provides additional insight to the coding of odors by LEC. By recording in awake, behaving mice, we were able to identify that a large subfraction of cells in the LEC responded to odors, and track these cells as mice learned an associative learning task.

We were especially interested in the type of transformation of odor coding that occurs at the synapse between the LEC and DG (**Figure 3.1**). It is conventionally assumed that the hippocampus translates simple sensory input representations from entorhinal cortex into a higher dimensional code (Igarashi et al., 2014; Zhang et al., 2014). It was perhaps surprising, then, that we witnessed responses in dentate granule neurons that resembled those seen in primary olfactory cortex--reliably responsive, odor selective, sharp responses on a trial-by-trial basis. These neurons with sharp

selectivity, however, only comprise a fraction of the whole population of active granule cells. Some fields of views that we assessed had very few odor-responsive neurons, but the entire neural ensemble was still able to encode odor identity to a very high accuracy, indicating that there is a combination of mixed selectivity cells alongside those that are conventionally defined as 'odor coding' by their sharp response curves. Even by sampling just a few hundred neurons on average, we observed very high levels of odor coding at the population level, indicating that odor representations are robust throughout the dentate gyrus, confirming what Vanderwolf reported decades earlier about dentate-specific fast wave spikes in response to odors (Vanderwolf, 1992).

Compared to a recent study that also looked at the activity of dentate granule neurons in awake mice, our results update our understanding of the DG beyond a role in spatial memory. Hainmuller and Bartos used a virtual 3D environment to look at place cell remapping over several days of learning. They found DG gcs were less likely to remap across environmental changes compared to cells in other hippocampal subregions (Hainmueller and Bartos, 2018). The relative stability of spatial codes in DG neurons contrasts with our finding of dynamic changes in odor responses across learning. Perhaps this has to do with the differential involvement of the MEC (spatial inputs) vs. LEC (nonspatial inputs) pathways in our respective tasks, and the type of connections made by LEC odor cells. It is known that immature granule cells are initially contacted preferentially by LEC inputs for several weeks as they incorporate

into dentate circuitry, and these newly-generated granule cells have higher levels of plasticity than their mature counterparts (Schmidt-Hieber et al., 2004; Vivar et al., 2012; Woods et al., 2018). It is enticing to speculate that the coding changes we see across associative learning in DG are occurring primarily via LEC contacts with immature granule cells. Even in baseline conditions (no learning), we saw a large enhancement in odor coding accuracy between the LEC and DG. Again, perhaps it is selective routing of odor information to newborn granule cells that facilitate this improved odor coding, as these immature cells would have a lower-threshold for LTP, increased inhibitory drive onto neighboring granule cells (increasing signal to noise), and less competing entorhinal input (lower levels of MEC involvement) (van Dijk and Fenton, 2018; Luna et al., 2019; Overstreet-Wadiche and Westbrook, 2006; van Praag et al., 2002; Woods et al., 2018). We witnessed in our computational model that some local circuitry mechanism in the dentate, or a neuromodulatory effect, could explain the observed boost in decoding efficacy. One exciting avenue for future research will be to specifically image these newly-generated neurons with our methods and track how odor responses change over the course of granule cell maturation into dentate circuitry, in part to determine if the LEC-DG odor pathway primarily recruits newborn granule cells.

This research is based entirely at understanding basic aspects of olfactory coding in the dentate gyrus, but the groundwork of these findings have implications for memory-related pathology. In Alzheimer's Disease (AD), the initial presence of amyloid

beta plaques accumulate in the lateral entorhinal cortex, before spreading into downstream hippocampal regions (Khan et al., 2014; Small et al., 2011). In terms of disease progression, plaque accumulation can occur for several decades before overt behavioral and cognitive symptoms develop (Braak and Braak, 1991). However, it has recently been observed that anosmia in individuals with mild cognitive impairment may be a predictive risk factor for the subsequent development of AD many years later (Growdon et al., 2015; Vassilaki et al., 2017). It is possible that early plaque accumulation in entorhinal-dentate circuits affect the perception of odors or related odor-cue associations critical for memory formation. Two possible avenues are opened up by the synthesis of these findings. One, instead of using crude olfactory assays to determine if individuals can smell/cannot smell, highly similar odor-pairs can be used in a learning task to potentially engage lateral entorhinal to dentate circuitry, and a measurable deficit in *odor discrminiation* may be more predictive of Alzheimer's pathology than current methods. Either a behavioral assay on its own, or in combination with functional neuroimaging, this approach could inform if humans engage this circuitry when discriminating odors, and if early stages of AD exhibit deficits in odor-evoke entorhinal-dentate activation. Second, there are several studies that suggest entorhinal deep brain stimulation is an effective method for either preventing the accumulation of amyloid beta plaques, or triggering some molecular cascade that effectively helps to clear plaques from these regions (Suthana et al., 2012; Xia et al., 2017). Importantly, deep brain stimulation in several of these animal

and human studies can restore some cognitive functioning. Yet, obviously, deep brain stimulation is invasive, expensive, and carries inherent risk for long-term use in the individual. What if, instead, odors can be used to conveniently stimulate activity in the lateral entorhinal cortex, and effectively enhance basal levels of synaptic transmission in this pathway? This could be an instance of naturalistic deep brain stimulation using odors as cues to engage the entorhinal-dentate circuitry, and perhaps by facilitating greater levels of ongoing activity, promoting cognitive function.

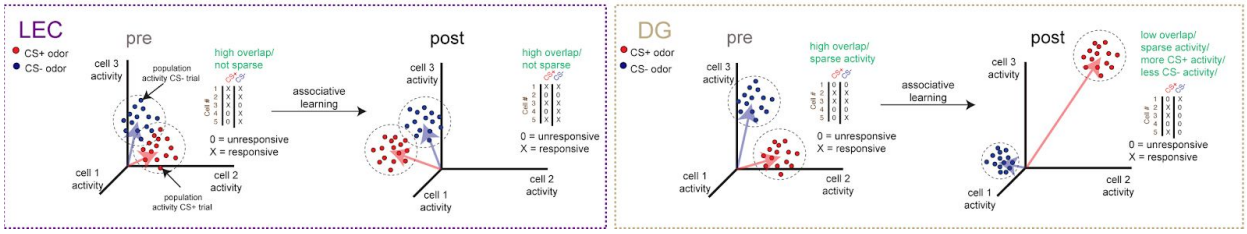

Figure 3.1: A conceptual model for the transformations of LEC and DG neurons in response to learning. On the left, LEC neurons initially have high overlaps in active ensembles for different odor pairs, and the firing of cells in response to odors is not sparse. These coding features remain largely intact in response to an associative learning task. In the DG, on the other hand, initial representations are overlapping but sparse. After learning, these representations enhance their sparsity, and become highly non-overlapping, effectively furthering the distance in coding space between CS+ and CS- stimuli. These changes could account for a pattern separation function of the DG, and may exhibit deficits in memory-related disease states.

References for Chapter 3:

Blazing, R.M., and Franks, K.M. (2020). Neuroscience: Illuminating Principles of Odor Coding. Curr. Biol. *30*, R1279–R1281.

Braak, H., and Braak, E. (1991). Neuropathological stageing of Alzheimer-related changes. Acta Neuropathol. *82*, 239–259.

van Dijk, M.T., and Fenton, A.A. (2018). Optogenetic silencing of immature and mature neurons in dentate gyrus to assess their roles in memory discriminations. bioRxiv.

Giessel, A.J., and Datta, S.R. (2014). Olfactory maps, circuits and computations. Curr. Opin. Neurobiol. *24*, 120–132.

Growdon, M.E., Schultz, A.P., Dagley, A.S., Amariglio, R.E., Hedden, T., Rentz, D.M., Johnson, K.A., Sperling, R.A., Albers, M.W., and Marshall, G.A. (2015). Odor identification and Alzheimer disease biomarkers in clinically normal elderly. Neurology *84*, 2153–2160.

Hainmueller, T., and Bartos, M. (2018). Parallel emergence of stable and dynamic memory engrams in the hippocampus. Nature.

Igarashi, K.M., Lu, L., Colgin, L.L., Moser, M.-B., and Moser, E.I. (2014). Coordination of entorhinal-hippocampal ensemble activity during associative learning. Nature *510*, 143–147.

Khan, U.A., Liu, L., Provenzano, F.A., Berman, D.E., Profaci, C.P., Sloan, R., Mayeux, R., Duff, K.E., and Small, S.A. (2014). Molecular drivers and cortical spread of lateral entorhinal cortex dysfunction in preclinical Alzheimer's disease. Nat. Neurosci. *17*, 304–311.

Leitner, F.C., Melzer, S., Lütcke, H., Pinna, R., Seeburg, P.H., Helmchen, F., and Monyer, H. (2016). Spatially segregated feedforward and feedback neurons support differential odor processing in the lateral entorhinal cortex. Nat. Neurosci. *19*, 935–944.

Luna, V.M., Anacker, C., Burghardt, N.S., Khandaker, H., Andreu, V., Millette, A., Leary, P., Ravenelle, R., Jimenez, J.C., Mastrodonato, A., et al. (2019). Adult-born hippocampal neurons bidirectionally modulate entorhinal inputs into the dentate gyrus. Science *364*, 578–583.

Overstreet-Wadiche, L.S., and Westbrook, G.L. (2006). Functional maturation of adult-generated granule cells. Hippocampus *16*, 208–215.

Pashkovski, S.L., Iurilli, G., Brann, D., Chicharro, D., Drummey, K., Franks, K., Panzeri, S., and Datta, S.R. (2020). Structure and flexibility in cortical representations of odour space. Nature.

van Praag, H., Schinder, A.F., Christie, B.R., Toni, N., Palmer, T.D., and Gage, F.H. (2002). Functional neurogenesis in the adult hippocampus. Nature *415*, 1030–1034.

Schmidt-Hieber, C., Jonas, P., and Bischofberger, J. (2004). Enhanced synaptic

plasticity in newly generated granule cells of the adult hippocampus. Nature *429*, 184–187.

Small, S.A., Schobel, S.A., Buxton, R.B., Witter, M.P., and Barnes, C.A. (2011). A pathophysiological framework of hippocampal dysfunction in ageing and disease. Nat. Rev. Neurosci. *12*, 585–601.

Sosulski, D.L., Bloom, M.L., Cutforth, T., Axel, R., and Datta, S.R. (2011). Distinct representations of olfactory information in different cortical centres. Nature *472*, 213–216.

Stettler, D.D., and Axel, R. (2009). Representations of odor in the piriform cortex. Neuron *63*, 854–864.

Suthana, N., Haneef, Z., Stern, J., Mukamel, R., Behnke, E., Knowlton, B., and Fried, I. (2012). Memory enhancement and deep-brain stimulation of the entorhinal area. N. Engl. J. Med. *366*, 502–510.

Vanderwolf, C.H. (1992). Hippocampal activity, olfaction, and sniffing: an olfactory input to the dentate gyrus. Brain Res. *593*, 197–208.

Vassar, R., Chao, S.K., Sitcheran, R., Nuñez, J.M., Vosshall, L.B., and Axel, R. (1994). Topographic organization of sensory projections to the olfactory bulb. Cell *79*, 981–991.

Vassilaki, M., Christianson, T.J., Mielke, M.M., Geda, Y.E., Kremers, W.K., Machulda,

M.M., Knopman, D.S., Petersen, R.C., Lowe, V.J., Jack, C.R., Jr, et al. (2017). Neuroimaging biomarkers and impaired olfaction in cognitively normal individuals. Ann. Neurol. *81*, 871–882.

Vivar, C., Potter, M.C., Choi, J., Lee, J.-Y., Stringer, T.P., Callaway, E.M., Gage, F.H., Suh, H., and van Praag, H. (2012). Monosynaptic inputs to new neurons in the dentate gyrus. Nat. Commun. *3*, 1107.

Woods, N.I., Vaaga, C.E., Chatzi, C., Adelson, J.D., Collie, M.F., Perederiy, J.V., Tovar, K.R., and Westbrook, G.L. (2018). Preferential Targeting of Lateral Entorhinal Inputs onto Newly Integrated Granule Cells. J. Neurosci. *38*, 5843–5853.

Xia, F., Yiu, A., Stone, S.S.D., Oh, S., Lozano, A.M., Josselyn, S.A., and Frankland, P.W. (2017). Entorhinal Cortical Deep Brain Stimulation Rescues Memory Deficits in Both Young and Old Mice Genetically Engineered to Model Alzheimer's Disease. Neuropsychopharmacology *42*, 2493–2503.

Zhang, S.-J., Ye, J., Couey, J.J., Witter, M., Moser, E.I., and Moser, M.-B. (2014). Functional connectivity of the entorhinal-hippocampal space circuit. Philos. Trans. R. Soc. Lond. B Biol. Sci. *369*, 20120516.

Chapter 4: Appendix on calcium analysis pipeline

Rationale for calcium imaging data management:

The collection of calcium imaging data presents a series of hurdles in terms of proper analysis. For one, calcium imaging is a relatively recent technique, so existing analysis pipelines are not currently well established, widely adopted, or flexible to different datasets. Significant strides have been made in the initial stage of signal extraction, with the adoption of partially automated methods to segment, deconvolve, and extract calcium traces from raw videos of 2-photon imaging (Pnevmatikakis et al., 2016; Zhou et al., 2018). But after this point, with the extracted calcium traces or inferred neural events in hand, what is next? How do you align the neural events with the behavior of the animal in the experiment, and what measures provide meaning in analyzing single cell or population responses? Each lab or individual often inherits the analysis techniques that are available and established by previous lab members, which can make for a piecemeal and oftentimes incomplete array of analysis options. Secondly, the inherently complicated nature of calcium imaging makes it a difficult type of data to analyze. It is commonplace to record hundreds of neurons from a single field of view within an animal, and these cells can fire many complex calcium transients over the timespan of recording. How can we make sense of the single cell firing characteristics or the whole population of neurons at once? We set out to establish an adaptable and general analysis pipeline for taking raw calcium transients and converting them into meaningful metrics of neural activity aligned to defined behavioral events, useful for

both single cell and population level analysis. Although much of the details of our analysis became highly specific and tailored to a particular experimental setup over time, it began as an attempt to make generic code that can be applied to a wide variety of datasets. This user guide is intended for subsequent scientists to understand, interface and adapt the code we will describe, with the goal of quickly making meaningful insights into trends of calcium imaging data and behavior.

Structuring the analysis pipeline:

1. Where to find list of notebooks and data for Woods, Stefanini et al. *Neuron* 2020:

Ubuntu computer jupyter notebook page:

https://169.230.191.169:1919/tree/home/nwoods/data/woods_etal18/

Make sure to hit “advanced” and “proceed anyways” if prompted.

“Woods_etal18” is the overarching folder that refers to all experiments conducted for paper, and some other experiments not in the paper.

2. How the data and notebooks are structured once in “woods_etal18” folder:

Below is shown a hierarchy organization for how folders are organized. One can imagine it as a russian doll type of arrangement, with the experiment being the outside layer, followed by animal, then individual imaging sessions for that animal. Each part of the hierarchy has the necessary folders/data/notebooks to run as a modular unit. Data structure explained more below.

Experiment structure

<experiment>

|_ results/

| |_ <mouse>

| | |_ <session>

| | | |_ notebooks/

| | | | (notebooks for that session, examples below)

| | | | |_ preprocessing.ipynb

| | | | | (basic preprocessing -- necessary)

| | | | |_ [other notebooks].ipynb

| | | | |_ selectivity.ipynb

| | | | | (computes cell tuning to combinations of trial type and behavior)

| | | | |_ psth.ipynb

| | | | (displays average cell behavior around trial event, e.g., CS+ onset)

| | | |_ data/

| | | | |_ behavior.txt

| | | | | (output of edit_arduino)

| | | | |_ C_df.txt

| | | | | (dff)

| | | | |_ Cnn.txt

| | | | | (for footprints)

| | | | |_ Coor.mat

```
|  |  |  |  | (for footprints)
|  |  |  |  |_ C_raw.txt
|  |  |  |  | (raw-signal - background)
|  |  |  |  |_ C.txt
|  |  |  |  | (denoised)
|  |  |  |  |_ S.txt
|  |  |  |  | (events)
|  |  |  |  |_ tseries.xml
|  |  |  |     (for time_ax)
|  |  |  |_ notebooks/
|  |  |     (notebooks comparing sessions)
|  |  |      |_ rates_early_vs_late.ipynb
|  |  |         (compare delta rates pre vs post learning)
|  |  |_ data/
|  |     (e.g., cell registration)
|  |      |_ sessions.txt
|  |         (information about sessions, e.g., pre and post)
|  |_ notebooks/
|     (notebooks comparing animals)
|      |_ rates.ipynb
|         (compare delta rates early vs late)
|_ code/
```

```
   |_ utils.py
   |  (the main code is here)
   |_ plots.py
   |  (generate nice plots)
   |_ template.ipynb
   |  (a notebook template for convenience)
   |_ doit.sh
```

Summary of notebook (nb) organization:

Basically, the data is organized in “woods_etal18” as a hierarchy of folders for all animals and experiments. First, each animal has its own folder. Within the animal folder, each experiment receives a specific folder, and within that experimental folder is a subset of folders containing: notebooks, data, and img (for images, i.e., pdfs generated and used for figures). We used one of the first DG mice, “Calvin” as the master animal where all new notebooks were created and amended, and we utilized a system whereby if a new animal is recorded, a copy is made of all the relevant notebooks from Calvin, then moved into a new folder for that new animal. That way, any coding errors or manipulations can be traced back to the original master code in “Calvin” where the code is not altered from its initial state. Since some, but not all, experiments were run in “Calvin” some other animals were also used as template/master animals where appropriate. Not all nb’s were run for each animal or experiment, as it will become evident that only a few nbs are used heavily for almost

every animal, whereas some nbs were utilized for specific experiments and their intended analyses. If looking for a nb that does not appear within “Calvin,” then check “Richard” for associative learning experiment analysis.

Running notebooks

The notebooks are supposed to be automatically run for each animal from the command line, but they can also be run manually if the user desires this approach. Notebooks automatically store data internally and load data from other notebooks. Dependencies across notebooks are not automatically sorted, therefore the user must know whether a notebook run is necessary to run a further notebook. Example: one must run the “preprocessing” notebook prior to running the “decoding_odors” notebook. To create new notebooks, one must use the templates. In particular, the first few cells of the template are important. After the necessary imports, the NOTEBOOK_NAME variable must be set to the actual notebook name. Then, the following code must be used:

```
//
from pickleshare import PickleShareDB
autorestore_folder = os.path.join(os.getcwd(), 'autorestore', NOTEBOOK_NAME)
db = PickleShareDB(autorestore_folder)
import sys
from workspace import *
import IPython
```

ip = IPython.get_ipython()

//

this will restore all the saved variables. ignore the errors listed. load_workspace(ip, db)

use `save_worspace(db)` to save variables at the end

One can comment out the load_workspace(ip, db) to avoid loading existing variables but it's useful for restoring a session saved with save_workspace(db).

3. What data do the notebooks need to run?

The data structure is organized as follows. The main folder results stores data and analysis results. These folders are not supposed to store raw data (e.g., TIFF videos) rather just the data necessary to run the analysis. This typically means a behavior file (aka, the "arduino file"), the XML file describing the time stamps of the imaging, and the results of the CNMF-E Matlab scripts.

The subfolders tree structure under the results folder (aka, the root folder) is organized in order of animal-session. In each session folder there's supposed to be a data folder containing the necessary data for that folder, an img folder with images of results from the analysis, a notebooks folder with the notebooks. Session names typically reflect the type of experiment and a reference time, e.g., sepodor_pre is a sepodor experiment (codename for three odors experiments in Woods et al. 2020) and pre refers to a pre-learning session.

In each experiment folder there's also a data folder, typically containing information useful to combine different sessions together, e.g., cell registration data. Consequently, there's also a notebooks folder with notebooks analysing multiple sessions of the same animal and an img folder with output images. The root folder results contains animal folders, a notebooks folder with notebooks typically summarizing the analysis results, and the usual img folder. The notebooks in this root folder are typically unique and are therefore usually not run automatically but instead manually run. Notebooks in the animal, experiment or session folders are meant to be created and run from the command line. All that is needed is an original notebook which serves as the master copy. This notebook is then copied into the appropriate folders as instructed from the command line and run. The results are automatically stored.

Within the folder for a session, there will always be a data folder that contains the raw data files necessary to run the intended notebooks. See "calvin/sepodor_pre" for example. Typically, an "events.txt", "c.txt", "tseries.xml", and "behavior_codes.txt" series of files is required. It is critical that these files are saved with specific names elsewhere and properly copied into the appropriate folder before applying the generic title of "events.txt" etc., so as not to lose track of the animal/experiment ID of that data file. Below is a list of corresponding animal files to locate the template. Make a copy of the folder for a new animals' analysis.

Experimental templates to use:

• animal1: data from calvin.

• animal1/three_odors: data from sepodor_pre and sepodor_post

• animal2: data from richard.

• animal2/associative: data from associative_d01, -02 and -03. • animal2/assfour: data from assofour_d01, -02 and -03.

Software for notebooks

For data analysis, we used a collection of Jupyter notebooks written in Python using publicly available standard numeric libraries.

The software is available upon request.

Software versions of the main libraries:

- Python: 2.7.12
- numpy: 1.13.1
- scipy: 0.19.1
- scikit-learn: 0.18.2

The behavior data consists of a list of (time, event string) elements. These are read from arduino .asc files converted with the edit_arduino.ipynb notebook into behavior codes, more manageable by Python.

Source code

• utils.py: all the useful functions to load data

• plots.py: all the plotting functions

A note on overall architecture:

Each nb essentially carries out one set of functions, whether it be decoding, similarity metrics, single cell selectivity, etc. In order to plot these variables, the functions called in nbs refer to variables defined in the utils.py folder. Here, you can find the arguments and returns for each function. This code is heavily annotated so that any user can understand how the calculations used in nbs are determined. Therefore, users should frequently refer to the utils.py folder for help in ascertaining details of operations.

4. Explanations of selected individual animal notebooks

(For a complete list of notebook descriptions, see google doc "notebook_explanations" and on server/ubuntu, reference "doc" and "current state" documents under woodsetal18/results/paper for a complete step-by-step process of adapting nbs for future data analysis).

preprocessing

This notebook takes the "behavior_codes.txt" file (which is the arduino behavior file) and aligns it to the "tseries.xml" file (which is the raw time series output from the 2P

prarieview program). It reads time from the tseries file as ground truth. For all other subsequent nb's to run properly, "preprocessing" needs to be run first. Also loads other relevant raw files, such as "C.txt" (the inferred calcium traces CNMFe output), and "events.txt" (the inferred spike events from CNMFe), and "A.txt" (the spatial footprints of each ROI from CNMFe) and "[].tif" if video is available. Will warn you if the tseries and behavior files are different lengths, which should prompt you manually checking that the arduino file was saved properly, for example.

Single session notebooks (within a single animal and within a single imaging session):

example notebooks: woods_etal18/results/calvin/sepodor_pre/notebooks

selectivity

Calculates the percent of cells that responded significantly to each odor tested. Both raw and adjusted stats. Adjusted stats are plotted in a simple bar graph. Similar nb's for 3-odor and 6-odor datasets. We defined cells as tuned to one odor by comparing the calcium events identified within all presentations of that odor (4s window) with the events identified 4 seconds periods preceding odor onset. We used a two-sided Mann-Whitney-U test to assess if the difference in activity levels was statistically significant. The positive or negative sign of the result of the test was then used to define positively and negatively tuned cells respectively.

psth

Plots the peri-stimulus time histogram for each cell in relation to all odor trials across every odor. Generates a pdf of all cells stored in the local /img folder. Needs variables from preprocessing and selectivity nbs. Figure 1 and 2 show psth from example cells.

decoding_odors

We used a linear decoder to decode the odor identities based on the recorded population activities. For each odor presentation, we defined the patterns of calcium activity by computing the mean event rates during the 4 seconds of odor presentation. We then evaluated the ability of a linear decoder (support-vector machine with linear-kernel, cite Bishop, python/scikit/linearSVC) to predict the odor identity based on the calcium activity on 10-fold cross-validated data. The decoding performance was then compared to a distribution of chance decoding performances evaluated by training our decoder on data in which odor identities where randomly shuffled with respect to the population activity patterns (n=100 data points, two-sided Mann-Whitney-U test, ***p<0.001, **p<0.01, *p<0.05). We further evaluate differences in the ability of our decoder to discriminate between single odor pairs, we trained it on the subset of data where we presented either of the odors in the pair and computed chance performance as above.

decoding_around_onset

We evaluated the ability of a linear decoder, a support-vector machine (SVM) with a linear kernel (cite Bishop, python/scikit/linearSVC), to predict the identity of the presented odor based on the population activity recorded in 1 second time bins during odor presentation. For each odor, we computed the mean values of the calcium events detected within 1 second long time bins starting 3 seconds before odor onset and ending 6 seconds after odor offset. We trained a separate decoder for each time bin separately and assessed its performance on 5-fold cross-validated data. For each time bin, we then report the mean decoding performance and the s.e.m.

decoding_odors_tuned_vs_untuned

Cells that don't pass a statistical test for tuning (untuned cells) to a certain stimulus, can still be used in a population to increase the ability to decode the stimulus identity via the correlated activity with the other cells in the population. Although this is true in general, it may not be necessarily the case in our data. To verify this possibility, we trained a linear decoder using the activity of the subset of tuned and untuned cells separately. To further allow for a fair comparison between the selected groups of cells, we randomly subsampled the more numerous group in an equal number to the other group. This nb requires “selectivity” to be run first in order to work properly.

decoding_odors_vs_ncells

Used to plot when combining animals, to look at the relationship between decoding accuracy and number of ROIs in FOV. Individual animal nb generates a number of cells and decoding accuracy (for 3 or 6 odors, for example). Supp fig x.x

decoding_timebins

Used for the decoding_timebins_animation_combo" (see below) and computes a second by second timebin decoding score (3-odor) with a leave one out linear SVC.

decoding_timebins_animation_combo

Generates an animation within a selected timeframe that will show denoised z-scored calcium imaging video, true odor identity, and decoded odor identity. Works for 3-odor.

repetition_suppression

We thought that if the same odor was presented twice in a row (by chance), that the activity rates during odor presentation might be affected. This nb calculates the change in activity rates for those occurrences.

similarity

To compute pattern similarities, we considered the mean event rates during each odor presentation in a session as well as the patterns during 4 seconds prior to odor onset

as baseline. We then computed the mean cosine similarities between every two pairs of patterns. This formula (see methods in Chapter 2) is also known as the Pearson similarity or Pearson correlation since the above formula is equivalent to the Pearson correlation coefficient for a sample. To further verify whether the pattern similarities were changing across time within the same session, we splitted the session into three blocks of 10 minutes (i.e., 30 trials each) and considered the similarity values within these blocks and among them. Needs preprocessing to run properly.

sparsity

Calculates the lifetime sparsity and population sparsity for each odor.

decoding_prepost

We assessed the stability of the population code by computing the generalization performance of a linear decoder to decode the recording session based on the population activity patterns during odor presentations. To decode the session, we first registered cells across recording sessions using CellReg (Sheintuch et al., 2017). We then identified activity patterns as in `decoding odors` and labeled them as belonging to one or the other session. Finally, we trained our decoder to discriminate between patterns of the same odor from the two different sessions and tested it on a different odor.

decoding_timebins_animation_combo

Makes a visualization of the FOV and Ca2+ signal heatmaps within a defined time window for animals. Need the raw .tif video file for the imaging session (motion corrected), decoding scores, and heatmap notebooks to be run. This is essentially the only time where we use the traces file from CNMF, rather than the events file.

rate_prepost

For registered, selective cells, calculate the difference in ca activity rate between pre and post, with either increase, decrease, or no change in activity rate. Calculated for odor presentation period.

overlaps

For each cell, we counted the number of odors that cell resulted tuned to from the panel of three odors used for the odor fear conditioning experiment. For each animal, we used the p-values obtained from the Mann-Whitney-U statistics (not corrected). We combined all cells identified across 10 imaged mice.

References for Chapter 4:

Pnevmatikakis, E.A., Soudry, D., Gao, Y., Machado, T.A., Merel, J., Pfau, D., Reardon, T., Mu, Y., Lacefield, C., Yang, W., et al. (2016). Simultaneous Denoising, Deconvolution, and Demixing of Calcium Imaging Data. Neuron *89*, 285–299.

Sheintuch, L., Rubin, A., Brande-Eilat, N., Geva, N., Sadeh, N., Pinchasof, O., and Ziv, Y. (2017). Tracking the Same Neurons across Multiple Days in Ca2+ Imaging Data. Cell Rep. *21*, 1102–1115.

Zhou, P., Resendez, S.L., Rodriguez-Romaguera, J., Jimenez, J.C., Neufeld, S.Q., Giovannucci, A., Friedrich, J., Pnevmatikakis, E.A., Stuber, G.D., Hen, R., et al. (2018). Efficient and accurate extraction of in vivo calcium signals from microendoscopic video data. Elife *7*, e28728.

Publishing Agreement

It is the policy of the University to encourage open access and broad distribution of all theses, dissertations, and manuscripts. The Graduate Division will facilitate the distribution of UCSF theses, dissertations, and manuscripts to the UCSF Library for open access and distribution. UCSF will make such theses, dissertations, and manuscripts accessible to the public and will take reasonable steps to preserve these works in perpetuity.

I hereby grant the non-exclusive, perpetual right to The Regents of the University of California to reproduce, publicly display, distribute, preserve, and publish copies of my thesis, dissertation, or manuscript in any form or media, now existing or later derived, including access online for teaching, research, and public service purposes.

DocuSigned by:
Nicholas Woods
F7411A582146475...
Author Signature

12/7/2020
Date